UNIVERSITÀ DI PISA

Università degli Studi di Pisa
Dipartimento di Fisica "E.Fermi"

Tesi di Dottorato
Dottorato di Ricerca in: Fisica – Ciclo XXIII (2008)
SSD – FIS/03

Development of a stabilized Ti:Sa frequency comb for frequency comparisons at high stability in the optical region

Candidato:
Denis Sutyrin

Supervisore:
Professore Nicolò Beverini

Coordinatore:
Professore Guglielmo M. Tino

Dicembre 2011

Dedication

In memory of my Mom.
In life she was my best friend, and in death she is always motivating me to live and to work

Acknowledgments

There are so many people that have helped me in so many ways. I could never name all those that contributed to my thesis and my life in ways both large and small. However I will take this small space and do what I can to acknowledge at least a few.

I could not have produced this thesis without the help of a very long list of people both inside Florence University-LENS, Pisa University and out, where they helped me along my professional and personal journeys. The list is, of course, too long to remember to thank everyone, but here is where I shall try. I am extremely grateful to each of them.

First of all, I would like to thank a lot my supervisor Prof. Nicolò Beverini. Despite on that I did my PhD about 80 km far from his office, I always feel his scientific and mental support to work on the thesis. I thank to Prof. Guglielmo Tino, who gave me the opportunity to work in his perfect laboratory with so many intelligent and friendly people.

The special thanks goes to Dr. Nicola Poli. We worked side-by-side for most of the construction and subsequent experiments, and I have come to admire his patience and generosity. I am a much better scientist because of his tutelage, and for that he has my gratitude.

My thanks to Dr. Sergei Chepurov, from whom I learn a lot about nature and femtosecond comb development. His ideas and recommendations were extremely helpful during all my work. I really happy to meet during the Prof. Marco Prevedelli, who is expressive example of accuracy and precision in work for me.

The work presented in Appendix A was performed in the optical clock laboratory at the Institute of Laser Physics in Novosibirsk. I am immensely grateful to people in the Novosibirsk, especially Prof. Vladimir Denisov, for making my visit possible to do science. I was privileged to work closely with Sergei Kuznetsov,

who is the big expert in fs Ti:Sa lasers. I appreciate also the advices of Alexey Lugovoi, Boris Nyushkov, Nicolai Chunosov.

One of the main trouble for me in Italy was bureaucracy. For this reason I would like to thanks all people, who helps me to solve them, especially secretaries in Florence University, Elisa Tonelli, and in Pisa University, Ilaria Fierro.

I would like to thank all people who help me in work and also did my life in Italy more entertaining: Marco Tarallo and Marco Schioopo (for too many thing to remember), Yu-Hung Lien (you organized many of grate events), Gabriele Rossi (you always gave me something useful from you lab), Giancarlo Ferrera (too many helps plus you was inspirer of soccer matches), Andrea De Michele (we start to build it together).

Abstract

This dissertation describes the development of a self-referenced optical frequency comb (OFC) based on a Ti:Sa femtosecond (fs) laser, to be employed in frequency comparisons between a strontium optical lattice clock and other frequency references, both in the radio-frequency (RF) and in the optical domain.

The Ti:Sa mode-locked laser, which employs external fiber broadening (EB) for the generation of octave-spanning spectrum, has been stabilized by locking an OFC tooth to a clock laser with high spectral purity, operating at 698 nm and resonant with the clock transition $^1S_0$-$^3P_0$ in neutral strontium atoms.

The frequency stability of this EB OFC has been tested both in the RF domain by comparison with a high-quality quartz oscillator slaved to the global positioning system (GPS) signal, and in the optical domain with a second stabilized diode laser at 689 nm slaved at long term to the intercombination transition $^1S_0$-$^3P_1$ in atomic strontium.

We perform a frequency noise and intensity-related dynamics characterization of the free-running fs Ti:Sa EB OFC and implement these results for optimizing the phase–lock of the OFC to a Hz-wide 698 nm semiconductor laser. Based on the frequency noise of the beatnote between the clock laser and corresponding EB OFC tooth f_{b698} we expect that the short term frequency stability of the 698 nm clock laser is then transferred to each tooth of the octave-spanning EB OFC.

Moreover, the noise transfer processes between the pump laser and the Ti:Sa laser have been studied in detail, both comparing the resulting frequency noise of the EB OFC output spectrum with a single-mode Coherent Verdi V5 and a multi-mode Spectra Physics Millennia Xs 532 nm pump lasers. In particular, in the latter case we demonstrate that the implementation of an additional control loop for the stabilization of carrier-envelope offset (CEO) frequency f_{CEO} allowed us to stabilize this signal at mHz level, that is compatible with f_{CEO} stabilization

results with the single-mode pump laser case.

Moreover, we show that, with our optical standard operated at a wavelength 698 nm the impact of f_{CEO} frequency noise on the frequency noise of any EB OFC tooth is negligible when compared with the frequency noise of the f_{b698}.

Despite the OFCs are used typically for precision frequency measurements, we demonstrate an approach to perform an absolute frequency measurement of unstable frequency by the EB OFC.

Most of this thesis is devoted to the EB OFC. However, I also present characteristics and our first stabilization results of the OFC working at quasi octave-spanning (QOS) regime.

Contents

1 Introduction **1**

1.1 The development of optical frequency measuring systems 1

1.2 Basic principle of the optical frequency measurements using an OFC 5

1.3 History of OFC development 7

1.3.1 Bulk crystal based: Ti:Sa OFC 9

1.3.2 Free-running OFC 10

1.4 Outline thesis 13

2 Theoretical aspects of OFCs and of frequency measurements **15**

2.1 Properties of ultrashort light pulses 15

2.1.1 Introduction 15

2.1.2 Dispersion 22

2.1.3 Managing of the Temporal Shape via the Frequency Domain 26

2.1.4 Waveguide Dispersion 30

2.1.5 Measurement of Chromatic Dispersion 31

2.2 Laser Mode-Locking 31

2.2.1 Mode-locking: Time- and frequency-domains of mode-locked laser 32

2.2.2 Kerr lens mode-locking 33

2.3 Principle of measurement of optical frequency 35

2.4 Supercontinuum Generation 37

2.4.1 The Physics of Supercontinuum Generation 38

2.4.2 Coherence Properties 40

2.5 Octave-spanning OFC 40

2.6 OFC dynamics 42

2.6.1 $\Delta\phi_{CEO}$ and f_{CEO} in the time domain . . . 42
2.6.2 The elastic tape model or fixed point formalism . . . 43
2.6.3 Intensity-related spectral shift . . . 44
2.6.4 Intensity-dependent f_{CEO} in octave-spanning Ti:Sa laser . . 46
2.6.5 Intensity-dependent f_{CEO} in Ti:Sa laser with spectrum broadening in PCF . . . 50
2.6.6 Response of f_{CEO} to a pump-power change . . . 51
2.6.7 Response of the repetition frequency to a pump-power change 51
2.6.8 Measurement of the f_{CEO} . . . 53
2.6.9 Amplitude-to-phase conversion effects . . . 54
2.6.10 Phase-locked OFC . . . 56

3 Apparatus **59**
3.1 Self-referenced home-build fs Ti:Sa laser . . . 59
3.1.1 Clean room environment . . . 60
3.1.2 Active medium: Titanium sapphire . . . 60
3.1.3 Pump lasers . . . 62
3.1.4 Femtosecond cavity design . . . 64
3.1.5 Elements for OFC stabilization . . . 71
3.1.6 Final design . . . 74
3.1.7 Photonic crystal fiber . . . 75
3.1.8 f-2f interferometer . . . 77
3.2 Quasi-octave spanning OFC . . . 80
3.2.1 Main characteristics of QOS OFC . . . 80
3.2.2 Passive stability of QOS OFC . . . 82
3.3 Clock laser . . . 83

4 Analysis of OFC frequency noise **89**
4.1 Free-running OFC behaviour . . . 89
4.1.1 Fixed point formalism . . . 89
4.1.2 Characterization of the frequency noise terms . . . 90
4.1.3 Turning point . . . 91
4.1.4 Intracavity and extracavity noise sources . . . 91
4.1.5 Cavity length perturbations . . . 92

4.1.6 Amplitude noise from pump lasers . . . 93
4.1.7 ASE-induced noise terms . . . 93
4.1.8 Shot Noise and Supercontinuum Generation . . . 94
4.1.9 OFC tooth linewidth estimation for free-running operation . 95
4.2 Stabilization of the OFC . . . 96
4.2.1 f_{CEO} stabilization . . . 97
4.2.2 f_{rep} stabilization: lock to the clock laser . . . 99
4.3 OFC stabilization results discussion . . . 101
4.3.1 Calculated frequency noise of different teeth of the stabilized OFC . . . 101
4.4 Stabilization of QOS OFC . . . 105
4.4.1 Fixed points for QOS OFC . . . 105
4.4.2 QOS OFC stabilization results . . . 105

5 OFC applications 111
5.1 Frequency measurements of the clock laser locked to an ULE cavity 112
5.1.1 Absolute frequency measurement of the clock laser locked to an ULE cavity . . . 112
5.1.2 Calibration of the clock laser frequency by the OFC . . . 115
5.2 OFC frequency stability in the the radio-frequency and in the optical region . . . 117
5.3 Absolute frequency measurement of unstable lasers with the OFC . 118
5.3.1 Introduction . . . 118
5.3.2 Experimental Setup . . . 119
5.3.3 Experimental results . . . 119

6 Conclusions 123

Bibliography 125

A The absolute frequency measurement of molecular iodine 149
A.1 Introduction . . . 149
A.2 Apparatus . . . 150
A.2.1 Ti:Sa OFC . . . 150

A.2.2 An apparatus for obtaining and investigations of emissive transitions optical resonances . . . 150
A.3 Modification of the setup . . . 151
A.3.1 New PZT mount . . . 151
A.3.2 Carrier-envelope phase-shift management . . . 153
A.4 Measurement . . . 153
A.5 Discussion . . . 155
A.6 Conclusion . . . 155

B Ti:Sa physical properties **157**

C Cooling and trapping strontium atoms **159**
C.1 689 nm laser . . . 160

D Apparatus for precision measurement of gravity **163**

E HeNe-laser based wavemeter **165**
E.1 Principle of Operation . . . 165
E.2 Practical use: alignment of the input laser beam . . . 166

F Frequency Stabilization of Lasers **169**
F.1 Oscillator phase noise . . . 169
F.1.1 Representing phase noise . . . 169
F.1.2 Power spectral density of the Phase Noise . . . 171
F.1.3 Power law model . . . 172
F.1.4 Allan variance . . . 173
F.1.5 Link between phase noise and Allan variance . . . 173
F.2 Passive stability of the laser frequency . . . 175
F.2.1 Long-term drift . . . 176
F.2.2 Short-term drift . . . 177
F.3 Active stabilization of the frequency . . . 177
F.4 Feedback Loops . . . 179
F.5 Feedback Loop: Loop Filter and Actuator . . . 181
F.5.1 The PID controller . . . 182

G Knife-edge method **183**
G.1 Knife-edge method 183
G.2 The Gaussian Distribution and the Error Function 184

List of Figures

1.1 Harmonic optical frequency chain 4
1.2 Using atomic resonances for optical mixing 5

2.1 (a) Refractive index of fused silica. (b) GDD of fused silica 26
2.2 Schematic diagram of a Gires-Tournois interferometer (GTI) 29
2.3 The basic time- and frequency-domain representations of the output of a mode-locked femtosecond laser 34
2.4 Kerr lens mode-locking 35
2.5 Two equivalent schemes for the measurement of f_{CEO} using an octave-spanning OFC 37
2.6 Fixed point model description for different types of fluctuations in the laser 45
2.7 (a) Definition of frequency terms: ω_0 is the gain peak, ω_c is the pulse spectral peak, ω_{rms} is the pulse spectral width, and $\omega_\Delta = \omega_c - \omega_0$. (b) Schematic showing the spectral shift effects 46
2.8 Linear relationship between df_{CEO}/dP and df_{rep}/dP with a slope of $\beta_0/(2\pi)$ 52
2.9 The measured df_{rep}/dP versus pump power 53

3.1 The energy levels diagram for Ti:Sa 62
3.2 (a) Index of refraction for Ti:Sa plotted for Sellmeir's equation. (b) GDD of Sapphire 63
3.3 (a) The RIN of all pump lasers used to pump the OFC. b) Free-running f_{CEO} of the OFC pumped by Verdi G7 65
3.4 Commonly used cavity for Ti:Sa laser 65
3.5 Schematics of our X folded Ti:Sa cavity 66

3.6 Regions for distance L_2 between mirror M_2 and Ti:Sa crystal when the cavity is stable . . . 69
3.7 Emission optical spectrum of Ti:Sa laser in fs regime with total cavity dispersion $\sim -400\text{fs}^2$ (left) and $\sim -150\text{fs}^2$ . . . 70
3.8 The passive stability of our OFC . . . 72
3.9 (a) - Configuration for using an AOM as a noise eater. (b) - Pump beam horizontal shifting . . . 74
3.10 Experimental setup of Ti:Sa OFC . . . 75
3.11 (a) - Typical measured dispersion of the fiber in the FEMTOWHITE 800. (b) - Principle behind the beam expansion in the device. . . . 76
3.12 Supercontinuum optical spectrum after the PCF . . . 78
3.13 Scheme for beam focusing in the BBO crystal . . . 80
3.14 (a) Scheme for beam focusing in the BBO crystal. (b) Typical observed f_{CEO} signal . . . 80
3.15 QOS OFC cavity scheme . . . 81
3.16 (a) QOS OFC output optical spectrum at different levels of the pump power. (b) QOS OFC broadest observed output optical spectrum . . . 82
3.17 (a) QOS OFC output power as a function of the pump power. (b) f_{CEO} as a function of the pump power (case of the mml pump) . . . 82
3.18 (a) f_{rep} of the free-running QOS FOC. (b) f_{CEO} of the free-running QOS FOC . . . 83
3.19 Experimental setup for the 698 nm clock laser frequency stabilization and characterization . . . 84
3.20 (a) Frequency noise of the stable 698 nm laser source locked to its ultra-high-finesse cavity. (b) Stability curves for the clock laser system 86

4.1 Measured intensity-related spectral shift . . . 92
4.2 Measured amplitude noise of sml and mml . . . 94
4.3 The calculated OFC tooth linewidth across the free-running OFC spectrum . . . 96
4.4 Electronics for the OFC stabilization . . . 97
4.5 Allan deviation of our local oscillator . . . 98

4.6 The noise spectral densities and the relative estimated Allan deviations of the phase-locked f_{CEO} . . . 100
4.7 The noise spectral densities and the relative estimated Allan deviations of the phase-locked f_{b698} . . . 102
4.8 Relative contributions of the frequency noise of f_{CEO} and the beat-note frequency between the OFC and the clock laser to a certain OFC tooth . . . 104
4.9 (a) Frequency noise of the stabilized f_{CEO} and f_{b698} signals. (b) Frequency noise of different teeth of our EB OFC phase-locked to the clock laser. . . . 104
4.10 Frequency counting of f_{b698} (Left) and f_{rep} (Right) signals of phase-locked QOS OFC to the clock laser . . . 106
4.11 f_{CEO} (Left) and f_{b698} (Right) phase noise of phase-locked QOS OFC 106
4.12 (a) Allan deviation of the f_{CEO} of the QOS OFC pumped by Verdi G7. (b) Locked f_{CEO} signal . . . 109

5.1 Schematic view of the experimental apparatus . . . 113
5.2 The frequency measurement of the f_{rep} and f_{CEO} . . . 114
5.3 The frequency measurement of the f_{rep} and f_{CEO} . . . 115
5.4 (a) Beat-notes between the OFC and 689 nm laser. (b) Allan deviation of the optical ratio . . . 117
5.5 Beat-notes between Verdi and the OFC . . . 120
5.6 Verdi absolute frequency measurement . . . 122

A.1 The setup for PZT resonances measurement . . . 152
A.2 PZT frequency resonance . . . 152
A.3 PZT phase resonance . . . 153

C.1 689 nm laser experimental scheme . . . 160

D.1 Experimental setup for Verdi frequency calibration and 1D ^{88}Sr optical lattice . . . 164

E.1 Optical setup of the wavemeter . . . 167

F.1 Oscillator Spectrum . . . 170

F.2 Phase noise, fractional-frequency noise and Allan variance 175
F.3 Simplified schematic of laser feedback loop 181

List of Tables

4.1 Values used in calculations 107
4.2 Fixed Point, Frequency Dependence, and Magnitude of the Various Contributions to the Frequency Noise on the Comb Lines 108

5.1 Rules for choosing sign of f_{CEO} and f_{rep} frequencies 114

A.1 Measured frequencies of molecular iodine 154

B.1 Physical properties of Ti:Sa 157

F.1 Phase noise 174

Chapter 1

Introduction

The creation and application of OFCs for precision measurements are the results of investigations and developments in the field of optical frequency measurement systems. Therefore, I would like to start describing in Sect. 1.1 the idea of the development of such systems. Sect. 1.2 describes investigations about detailed study of OFCs itself. While in Sect. 1.3 I focus on the historical results to create OFC and implement for frequency measurements.

1.1 The development of optical frequency measuring systems

The invention of the laser [1] made a revolution in many fields of science: spectroscopy, material processing, photochemistry, microscopy etc. and also in military, medicine and industry. Our interest is the laser impact on Metrology.

Heterodyne beatnotes experiments between independent lasers showed that lasers could have an excellent spectral and spatial coherence with relatively narrow linewidths, $\delta\nu$, and correspondingly low fractional uncertainty, $\delta\nu/\nu_0$, where ν_0 is the atomic transition frequency. The stability of frequency standard in the optical region potentially can be better than in microwave due to the fact that Allan deviation is determined as

$$\sigma_y(\tau) = \frac{\delta\nu(\tau)_{rms}}{\nu_0} = \frac{1}{\pi Q}\sqrt{\frac{T_c}{2N_0\tau}} \tag{1.1}$$

where $\delta\nu(\tau)_{rms}$ is the measured frequency fluctuation, T_c is the cycle time (i.e., the time required to make a determination of the line center), N_0 is the number of participating particles (atoms), τ is the total averaging time, $Q = \Delta\nu/\nu_0$ is the resonance quality factor of an optical clock transition.

Due to its high frequency, the practical implementation of optical standard has a significant technical challenge. This is because an absolute frequency measurement must be compared with the primary standard, which since 1967, is the hyperfine transition of a cesium atom with frequency of about 9 GHz. Optical standards have frequencies ∼50 000 times higher. There were no devices that could link directly microwave and optical regions.

At the beginning, for solving this task, the natural method was to start with the highest possible frequency from the oscillator, that can be coherently controlled and linked to the primary standard and then step by step multiply its frequency up to the optical region by using different types of nonlinear devices.

For this approach were developed new techniques of frequency multiplication that can work from microwave to IR region. Practically, from 1960 up to 1990, this approach was realized by using klystrons or backward wave oscillators for high frequency generation (up to 300 GHz). These devices could be phase–locked to microwave standard through low-frequency microwave mixing techniques and quartz crystals. The frequency multiplication step from hundreds of GHz to IR region demanded new methods and devices. To avoid the use of too many stable oscillators to span the electromagnetic spectrum, new devices should have had the highest possible frequency multiplication factor. Moreover, they had to be able to work in the microwave and IR regions. The search of such devices give us three interesting devices: whisker-contacted Schottky diodes, point-contact Metal-Insulator-Metal (MIM) diodes and superconducting Josephson mixers [2–5].

With new nonlinear mixers was possible to reach the 2-5 THz range. Above this region it was necessary to use FIR lasers with which was possible to reach ∼30 THz. To coherently generate a visible laser frequency near 500 THz starting from a 1 THz source and relying only on successive stages of second-harmonic generation would require $2^N = 500$, or $N \approx 9$, stages. With judicious choices of FIR lasers and mixers it was possible to achieve higher-order mixing (e.g. ×10 or ×12) in the THz range. This meant that is was possible to jump in a single step from a FIR laser at ∼1 THz to another FIR laser at ∼10 THz. With two

additional mixing orders, the 10 THz signal can be multiplied up to the 30 THz frequency of the convenient, powerful and stable CO_2 lasers [6].

At frequencies above 30 THz, MIM diode mixers are suitable for some mixing and harmonic generating applications (e.g. 3×30 THz $= 90$ THz), but nonlinear optical crystals can be very effective alternatives because they can be phase-matched for efficient mixing of specific desired frequencies/wavelengths.

Unfortunately, at higher frequencies no convenient nonlinear mixing elements were found that could generate continuous wave (CW) high harmonics. Lacking that, the mixing orders were necessarily low, and optical frequency chains required several stable laser sources spanning the frequency range and all locked together with phase-locked-loops - hence the analogy of a chain with interlocking loops. Several big labs worked on harmonic optical frequency chains that used these approaches to reach important optical frequency references directly from microwave frequency sources. They continued to develop and refine optical frequency measurement methods and synthesis chains that were used to measure and evaluate optical frequency standards [4, 7–19].

Because of their complexity and specialized applications, only a small number of optical frequency chains were ever constructed. One of such setup is presented in Fig. 1.1. This was the frequency chain developed by *Chebotayev's* group at Novosibirsk and configured to operate as an optical time scale, i.e. an 'optical clock'. The frequency chain was controlled from a CH_4 frequency standard at 88 THz (3.39 μm) at the top and delivered an output at a RF/microwave frequency [20].

A novel way around the problem of the lack of any efficient nonlinear mixers for low-power CW lasers was the concept from *Klement'ev* et al. [21] who proposed using resonant interactions in atoms to efficiently sum three optical frequencies to generate a fourth. Specifically, they proposed using Ne atomic resonances to sum the well-known He-Ne laser lines at 3.39 μm, 1.15 μm and 1.5 μm in order to generate the 633 nm laser line as shown in Fig. 1.2. The advantage is that resonant atomic nonlinear mixing can be 8 to 10 orders of magnitude stronger than that found in bulk nonlinear optical materials. The obvious disadvantage is that the optical mixing is not broadband, and so only very specific frequencies can be generated. The four-photon optical mixing approach of Fig. 1.2 was demonstrated in Russia [21] and was also used at NIST for the measurement of the 633 nm He-Ne frequency [3].

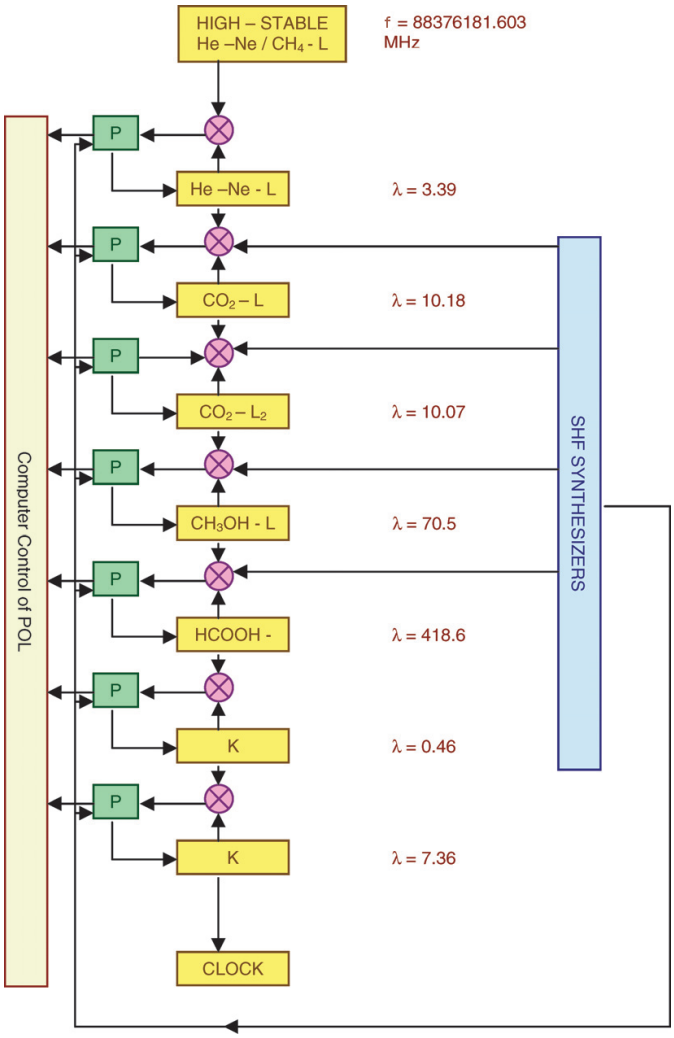

Figure 1.1: Harmonic optical frequency chain. It was developed by *Chebotayev's* group at Novosibirsk and configured to operate as an optical time scale, i.e. an "optical clock". The yellow boxes are sources, the green boxes are phase-locked loops, the red circles are harmonic mixers.

Demonstration of optical molecular clocks were done in Novosibirsk [23] and at PTB [7]. Both used He-Ne/CH_4 optical frequency standard. Optical clock on I_2 was demonstrated in [24], and on cold atoms/ions in [25–28].

Great improvements of optical clock frequency uncertainty were at the beginning of 2000. These were the results of optical standards referred to laser cooled

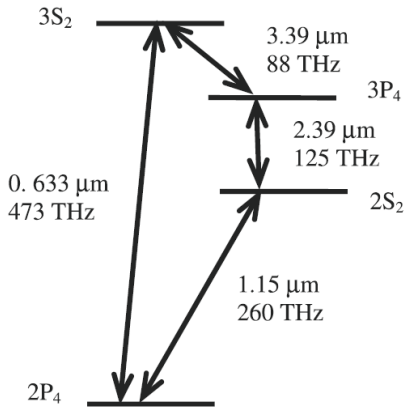

Figure 1.2: Using atomic resonances for optical mixing. It was proposed by *Klement'ev* et al. [21] and first demonstrated in USSR using the Ne transitions shown here. This scheme was also implemented by a team at NBS using 8 m long He-Ne gain tubes in a measurement of the frequency of the 473 THz (633 nm) laser [3,22].

and trapped atoms/ions and of the developments of fs OFCs. Cold atoms/ions were developed in many laboratories around the world and fs OFC technology provides practical optical synthesizers and frequency dividers.

1.2 Basic principle of the optical frequency measurements using an OFC

In 1998, *Hänsch* and co-workers introduced a revolutionary approach vastly simplifying optical frequency measurements. By using the modes of optical frequencies emitted by a mode-locked fs laser as a ruler, they were able to measure differences of several tens of THz between laser frequencies [29–31]. Next several experiments [32–36] definitely pointed out that, by establishing a phase-coherent link between optical frequencies and the radio frequency domain, the modes of a mode-locked fs laser could be used as an extremely precise and absolute ruler in frequency space.

The emission of a mode-locked fs laser is formed by an ideal regular train of optical pulses and its optical spectrum presents a series of repeating, equally

spaced spectral lines.

The spacing of the spectral lines of such OFC is given by the repetition rate f_{rep} at which pulses are emitted from the mode-locked laser, while the phase shift $\Delta\phi_{CEO}$ between the pulse carrier and the pulse envelope each round trip determines the overall offset of the comb elements $f_{CEO} = f_{rep}(\Delta\phi_{CEO}/2\pi)$. The relationship between these two parameters and the nth element of the OFC is given by the simple expression

$$\nu_n = nf_{rep} \pm f_{CEO} \tag{1.2}$$

where $n \approx 10^6$. Here and later in the thesis, the symbol ν refers to optical frequencies, while f - to RF frequencies. The unknown absolute optical frequency of a cw laser, whose frequency lies close to OFC tooth n, can be determined by the equation

$$\nu_{cw} = \nu_n \pm f_b = nf_{rep} \pm f_{CEO} \pm f_b \tag{1.3}$$

where f_b is the beatnote between cw laser and corresponded OFC tooth n.

For a high-precision determination of f_{CEO}, it must be directly measured, and typically it is performed by using nonlinear frequency generation to compare different regions of the frequency comb [37]. For example, if the laser spectrum covers more than one octave, then the OFC teeth at the low-frequency end of the spectrum can be doubled in a nonlinear crystal and subsequently heterodyned against the high-frequency teeth of the OFC to yield f_{CEO}. An important advance in this respect is the generation of octave-spanning spectra with low-power Ti:Sa lasers in microstructured fibers [38,39], or by direct generation from the laser itself [40–42]. Once measured, f_{CEO} can then be locked at a fixed frequency with the use of servo-control techniques.

Phase-lock of one tooth n of the OFC can be done to the low-noise cw laser, that has itself been steered to an atomic resonance, or directly to a known microwave standard.

OFC becomes a final tool in the long history of the development of optical frequency measuring systems. The dramatic simplification of a complex optical frequency chain to a single mode-locked laser has facilitated optical frequency measurements. An important aspect of this new technology is its high degree of

reliability and precision together with a lack of systematic errors. For example, it has been shown that the f_{rep} of a mode-locked laser equals the mode spacing to within the measurement uncertainty of 10^{-16} [29]. The uniformity of the comb's mode spacing has also been verified to a level below 10^{-17} [29], even after spectral broadening in fibers.

OFCs are used nowadays in many applications including optical frequency metrology [36, 43, 44] optical clocks [45, 46] comb-calibrated tunable lasers [47–49], OFC spectroscopy [50–52], frequency/time transfer [53, 54], low-phase-noise microwave generation [55–57], calibration of astronomical spectra [58] and search for variations of fundamental constants [59, 60].

1.3 History of OFC development

Mode-locking was first demonstrated in the mid-1960s using a He-Ne laser [61], a ruby laser [62], and a Nd:glass laser [63]. Unfortunately, from the early 1960s until about 1990, the pulsed and cw lasers communities continued to diverge. The cw lasers community worked on the stability of their lasers. While pulsed lasers researches were focused on escalation of pulsed power.

The key technique for mode-locking was Q-switching based on the implementation of saturable absorbers. It was generally preferred to obtain high pulse energy rather than stability.

In the period from 1970s up to 1980s interest of researchers was focused on ultrafast dye lasers. For this type of laser Q-switching instabilities are not a problem, and also dye lasers soon allowed the generation of much shorter pulses. In 1974 the first sub-picosecond passively mode-locked dye laser [64–66] and, in 1981, the first sub-100-fs colliding pulse mode-locked (CPM) dye laser [67] were demonstrated.

In the 1980s begins a time when diode lasers achieve an average power high enough for pumping solid state lasers. This provides dramatic improvements in efficiency, lifetime, size, and other important laser characteristics. For example, actively mode-locked diode-pumped Nd:YAG [68] and Nd:YLF [69–72] lasers generated 7-12 ps pulse durations for the first time. In comparison, flashlamp-pumped Nd:YAG and Nd:YLF lasers typically produced pulse durations of ≈100 ps and ≈30 ps, respectively [73, 74]. Before 1992, however, all attempts to passively mod-

elock diode-pumped solid-state lasers resulted in Q-switching instabilities.

The first significant step in ultrafast solid-state lasers was performed in the end of 1980s, when was demonstrated the Ti:Sa laser [75]. The strong interest in an all-solid-state ultrafast laser technology was the driving force, and formed the basis for many new inventions and discoveries.

The next significant step in ultra-short pulse production was made in 1990. Two important papers were presented: *Ishida* et al. presented passively mode-locked Ti:Sa laser with an intracavity saturable absorber dye that produced stable 190 fs pulses [76]. Second, *Sibbett's* group presented 60 fs pulses from a Ti:Sa laser that appeared not to have a saturable absorber [77]. This second result - in the absence of a visible saturable absorber - had an immediate impact on the research community, but the ultrafast laser experts realized that the first result was also very surprising, even though a saturable absorber was present. It was clear that the dye saturable absorber, with a recovery time in the nanosecond range, could not support ultrashort pulses with a Ti:Sa laser as it could with dye lasers. *Sibbett's* modelocking approach was initially termed 'magic modelocking', and it triggered a major research effort into understanding passive modelocking of solid-state lasers. This form of modelocking was soon explained [78–80] and is now referred to as Kerr lens modelocking (KLM). *Ishida's* result was also explained by KLM: the slow dye saturable absorber only provided a reliable starting mechanism for KLM.

The short pulses from these systems provide a very broad optical spectrum. However, it is also important also that spectrum also is *stable comb-shaped*, where the spacing of the individual longitudinal modes exactly equals the pulse repetition rate. Phase-locking the optical frequencies of the OFC to a laser serving as the oscillator of the clock results in the phase-locking of the OFC spacing (i.e., the laser repetition frequency) to the clock's oscillator as well. Therefore, the OFC provides the phase-coherent division from an optical frequency to a microwave frequency, and the clock output is the repetition frequency of the mode-locked laser producing the comb.

The OFC produces a "ruler" in the frequency domain with which an unknown optical frequency can be measured. However, many years passed before this "simple idea" [81] to use OFC was realized.

1.3.1 Bulk crystal based: Ti:Sa OFC

OFC can be produced by several types of lasers. Nowadays, three groups of OFCs can be outlined: bulk crystal based, fiber-based and microresonator-based OFCs. Among them, the bulk crystal based group is our interest.

The main active medium in bulk laser is Ti:Sa. The working principle of it is a Kerr-lens. The primary reason for using Ti:Sa is its enormous gain bandwidth (700-1000 nm), which is necessary for supporting ultrashort pulses as ruled by the Fourier formula. Moreover, a Ti:Sa crystal also serves as the nonlinear material for mode-locking through the optical Kerr effect which manifests itself as an increase of the nonlinear index at increasing optical intensity. Since the transverse intensity profile of the intracavity beam is Gaussian, a Gaussian index profile is created in the Ti:Sa crystal, which makes the latter equivalent to a lens. As a consequence, the beam tends to focus, the focusing increasing with the optical intensity. Together with a correctly positioned effective aperture, the nonlinear (Kerr) lens can act as a saturable absorber, i.e. high intensities are focused and hence are fully transmitted through the aperture, while low intensities experience losses.

Since short pulses produce higher peak powers, they experience lower losses, making mode-locked operation favorable. This mode-locking mechanism has the advantage of being essentially instantaneous, but has the disadvantages of not being self-starting and of requiring a critical misalignment from optimum cw operation. Since most of the pulse broadening in ultrashort pulses is caused by group delay dispersion (GDD) of the gain medium, to obtain the shortest possible pulses from the laser cavity the overall GDD has to be near zero. To counteract the Ti:Sa normal dispersion, a prism sequence is used, in which the first prism spatially disperses the pulse, causing the long wavelength components to travel through more glass in the second prism than the shorter wavelength components. The net effect is to generate an effective anomalous dispersion that counteracts the normal one in the Ti:Sa crystal. The spatial dispersion is canceled by placing the prism pair at one end of the cavity so that the pulse retraces its path through the prisms. With an optimum material choice, it is possible to minimize both second-order and third-order dispersion, yielding only a fourth-order dispersion limitation [82].

It is also possible to generate anomalous dispersion by the so-called chirped mirrors [83]. These have the advantage of allowing shorter cavity lengths, but the

disadvantage of less adjustability, if used alone. Chirped mirrors also allow additional control over higher order dispersion and have been used in combination with prisms to produce pulses even shorter than those achieved using prisms alone [84].

1.3.2 Free-running OFC

When considering the shape of the OFC lines of a mode-locked laser, there is a fundamental distinction between the case of a free-running laser and the case of a laser locked to an external reference. In the former case, when the noise source is spontaneous emission (SE) noise or any other white noise source, the central time and the phase of the mode-locked pulse undergo a random walk, and the OFC lines have a stationary shape. In the latter case, again assuming white noise, the central pulse time and the phase are bounded, and there is no stationary line shape; the measured line width is inversely proportional to the measurement time. However, the phase noise spectrum of each OFC line is stationary, and that spectrum - not the frequency spectrum - is physically meaningful.

Any clock or frequency measurement system consists of an oscillator and a counter [85]. The clock performance depends on the frequency noise of the oscillator and the phase noise of the counter. Virtually all theoretical calculations to date of the noise properties of passively mode-locked lasers have focused on the frequency spectrum of a free-running laser, but in modern time and frequency metrology applications, these lasers are part of the counting system [86], so it is their phase noise spectrum after they are locked to an oscillator that is important.

The properties of stabilized OFC strongly depend on properties of free-running OFC because they become parts of the transfer function of the servo loop. The frequency noise of both degrees of freedom of OFC should be studied and optimized before a OFC stabilization.

Frequency noise of free-running OFC

When light passes through any gain medium, it will acquire noise through SE [87]. The SE noise sets a fundamental limit on the linewidth of a laser. For a cw laser, this Schawlow-Townes limit is due to phase jitter [88]. The situation with mode-locked lasers is more complicated. A mode-locked laser produces a train of pulses, regularly spaced in time, and the frequency spectrum is a series of narrow

OFC lines. The width of each OFC line depends on the timing and phase jitter of the pulse train. The laser dynamics are characterized by four pulse parameters: the pulse energy, the carrier frequency, the central pulse time, the phase, and in addition a fifth parameter: the round-trip gain. In all mode-locked lasers, strong nonlinearities couple amplitude and frequency fluctuations into timing and phase jitter. The quantum-limited noise properties of mode-locked lasers were first treated by *Haus* and *Mecozzi* based on soliton perturbation theory in [89], hereafter referred to as HM. Until recently, subsequent work focused mainly on quantum-limited timing jitter. With the development of fs OFCs [86], the more general problem of timing and phase jitter has received more attention [90–96]. While HM calculated the timing and phase jitter rather than the OFC linewidths, that paper contains almost all of the information needed to calculate the linewidths. More recent works extend HM model [90, 91], including technical noise contributions [92, 96]. The effects of gain dynamics [94] and spontaneous emission limited noise properties were studied in the work of *Wahlstrand* et al. [97]. A major unknown in all theoretical efforts to date was the strength of couplings between pulse parameters. Theoretical predictions carry large uncertainties and depend on the details of the laser design, including dispersion management. The quantitative measurement of the linear response of the pulse energy, the central frequency, the round-trip gain were done by *Menyul* et al. [98]. The timing and the phase measurement of a mode-locked Ti:Sa laser by *Wahlstrand* et al. [99].

Previous evaluations have proven the OFC's suitability for precision optical metrology. The fractional frequency uncertainty of Ti:Sa-based OFCs has been evaluated at the 10^{-19} level at 1000 s [100, 101]. Experiments testing the phase coherence of Ti:Sa OFCs have been able to place upper limits on the relative linewidth of different spectral regions for both locked and free-running OFCs at 20 mHz [102] and 9 mHz [103], respectively, and were ultimately limited by by differential-path technical noise caused by air currents and mirror vibrations. In [104] the OFC was compared to a 10 W average power Yb fiber OFC locked to a common optical reference, with a resulting 1 mHz resolution bandwidth-limited relative linewidth. This indicates that the Ti:Sa OFC should be capable of supporting narrower relative linewidths.

Intensity related dynamics of OFC

The f_{CEO} was first measured for soliton like pulses in a laser cavity operating in the net negative dispersion regime [105]. A decrease of the f_{CEO} for increasing pulse energies was explained by a power-dependent wavelength shift, which, together with the negative GDD, dominated over the accumulated soliton phase [105]. A detailed analysis of the f_{CEO} [106] based on the perturbed nonlinear Schrödinger equation for the fundamental soliton revealed that the pulse energy modulates the group delay due to self-steepening. The resulting timing shift contributes twice as much to the f_{CEO} and is of opposite sign as the nonlinear phase due to self-phase modulation. Later measurements of the f_{CEO} using continuum generation in microstructure fiber confirmed that the self-steepening mechanism prevailed [107–109]. For dispersion-managed solitons [110], which best describe the pulse dynamics in few-cycle Ti:Sa lasers, the Kerr-induced phase shift was derived to be reduced compared to classical solitons [106]. Under strong dispersion management, an analytical and numerical evaluation of the phase slip for dispersion-managed solitons presented that contributions from the shock-term and the phase slip can nearly cancel each other [111]. Analytical and experimental studies showed that the intensity-related spectral shift could be reduced by minimizing the carrier frequency shift [112]. For a broader spectrum, which was obtained for smaller magnitudes of net group delay dispersion, the coupling between the negative GDD (values as high as -400 fs^2) and intensity fluctuations decreased [112]. In addition, the Raman effect was identified as a possible mechanism contributing to spectral shifts [112]. For octave-spanning Ti:Sa lasers, measurements of the pump power-dependent carrier envelope offset frequency agreed sufficiently well with previous results based on soliton perturbation theory so that it was suggested that spectral shifts could be neglected for broadband intracavity spectra [94]. All these results indicate that the f_{CEO} dynamics depend strongly on the laser configuration.

Fixed point formalism

At the same time the the fixed point formalism was introduced by *Telle, Havercamp* and coworkers in [113, 114]. The formalism was used in several works to estimate the frequency noise of the optical spectrum of fs fiber lasers [92, 96, 115]. Moreover, it has been shown that for each type of noise source there is an optimum pivot

point for the control of the optical spectrum [93].

1.4 Outline thesis

This thesis presents the design and implementation of a Ti:Sa OFC phase-locked to a semiconductor clock laser resonant with ^{88}Sr $^{1}S_0$-$^{3}P_0$ clock transition.

The first step was to build up a Ti:Sa laser, reach the fs regime and broaden the optical spectrum in a photonic crystal fiber (PCF) for stabilizing f_{CEO} in a self-referencing scheme via interferometric detection of the f-$2f$ beat note. The optimization of the OFC passive stability also was done during this stage of work.

The second step was the stabilization of EB OFC degrees of freedom. The importance of intensity dynamics was observed and studied. This helped us to found a working region of f_{CEO} as a function of the multimode pump power, where amplitude noise is highly suppressed. We have demonstrated that with a multi-mode pump, by choosing the optimum pump power, and by implementing a PZT on one pump mirror, the f_{CEO} can reach the same stability level obtained with a single-mode pump.

To test the EB OFC stability and its feasibility for frequency measurements we measured the frequency ratio of the 698 nm clock laser and the 689 nm laser stabilized to the ^{88}Sr atomic resonance. The result has demonstrated better short term stability than the absolute frequency measurement of optical frequencies against a RF reference. We implement our EB OFC for the absolute frequency measurement of the Verdi V5 with sub-MHz resolution and observed the fast and the slow behavior of its frequency by the use of a EB OFC. The frequency measurements have been used in an accurate determination of gravity by the use of ^{88}Sr atoms trapped in vertical lattices. This work demonstrates the great flexibility of OFCs for precision measurements of optical frequencies of unstable lasers. This study in turn may also be important for the study of stabilization techniques of CW solid-state diode pumped lasers and moreover could be important for the study of Ti:Sa fs lasers dynamics.

The optimization of stability was done by the study of the frequency noise of the free-running OFC. The noise analysis of a free-running EB OFC shows that different perturbations of a EB OFC have different fixed points that are lying in different parts of spectrum. For this reason, it is useless to stabilize frequency in

certain region by using perturbations which have fixed points near to it. For us this formalism gives a prove that new stabilization technique, the pump beam shifting, is suitable for f_{CEO} stabilization. Due to the absence of the experimental ways to prove that stability of our clock laser transferred across EB OFC, we estimate a stability from the related phase noise measurements. Allan deviation is given by

$$\sigma_y^2(\tau) = \int_0^\infty S_y(f) \frac{\sin^4(\pi\tau f)}{(\pi\tau f)^2} df \tag{1.4}$$

where $S_y = S_{\nu n}/\nu_0$. Then the stability is changed less than one order of magnitude across the OFC.

The format of this thesis is as follows. In Chapter 2 the theoretical concepts and principles of frequency measurement are discussed including a method for frequency noise description of a free-running OFC. Chapter 3 describes the construction of the experimental apparatus used for our experiments and a detailed characterization of the Ti:Sa OFC. Chapter 4 is focused on the frequency noise properties and dynamics of our free-running Ti:Sa EB OFC and on the implementation of this knowledge for an optimization of OFC stabilization loops. Chapter 5 describes the applications of the EB OFC for measurements of the ratio of optical frequencies and the absolute frequency of an unstable laser.

Chapter 2

Theoretical aspects of OFCs and of frequency measurements

I start to describe the theoretical aspects from the properties of ultrashort light pulses in Sect. 2.1 where I introduce the dispersion definition (SbSect. 2.1.2). The optical spectrum of OFC in the frequency domain is introduced in Sect. 2.2. The optical frequency measurement principle is explained in Sect. 2.3. In Sect. 2.4 is discussed the physics of supercontinuum generation, while the working principles of octave-spanning OFCs are presented in Sect. 2.5. In Sect. 2.6 several specific important topics are described: definition of CEO phase and frequency (SbSect. 2.6.1), the fixed point formalism (SbSect. 2.6.2), intensity-related spectral shift (SbSect, 2.6.3), the intensity-related dynamics of f_{CEO} in octave-spanning Ti:Sa OFCs (SbSect. 2.6.4) and in EB Ti:Sa OFCs (SbSect. 2.6.5), the response of f_{CEO} and f_{rep} to a pump-power change in a fs fiber laser, which have similar behavior comparing with Ti:Sa fs laser case in SbSect. 2.6.6 and SbSect. 2.6.7, amplitude-to-phase conversion effects (SbSect. 2.6.9), the principle to phase-lock OFCs (SbSect 2.6.10).

2.1 Properties of ultrashort light pulses

2.1.1 Introduction

For the mathematical description we followed the approaches of [116–118].

In linear optics the superposition principle holds and the real-valued electric field $E(t)$ of an ultrashort optical pulse at a fixed point in space has the Fourier decomposition into monochromatic waves [116, 117, 119]

$$E(t) = \frac{1}{2\pi} \int_{-\infty}^{\infty} \tilde{E}(\omega) e^{i\omega t} d\omega \tag{2.1}$$

where $|\tilde{E}(\omega)|^2$ is the spectrum. $\tilde{E}(\omega)$ is obtained by the Fourier inversion theorem

$$\tilde{E}(\omega) = \int_{-\infty}^{\infty} E(t) e^{-i\omega t} dt \tag{2.2}$$

Since $E(t)$ is real-valued $\tilde{E}(\omega)$ is Hermitian, i. e., obeys the condition

$$\tilde{E}(\omega) = \tilde{E}^*(-\omega) \tag{2.3}$$

where * denotes complex conjugation. Hence knowledge of the spectrum for positive frequencies is sufficient for a full characterization of a light field without dc component we can define the positive part of $\tilde{E}(\omega)$ as

$$\begin{aligned} \tilde{E}^+(\omega) = & \tilde{E}(\omega) \qquad \text{for } \omega \geq 0 \qquad \text{and} \\ & 0 \qquad \text{for } \omega < 0 \end{aligned} \tag{2.4}$$

The negative part of $\tilde{E}(\omega)$ is defined as

$$\begin{aligned} \tilde{E}^-(\omega) = & \tilde{E}(\omega) \qquad \text{for } \omega < 0 \qquad \text{and} \\ & 0 \qquad \text{for } \omega \geq 0 \end{aligned} \tag{2.5}$$

Just as the replacement of real-valued sines and cosines by complex exponentials often simplifies Fourier analysis, so too does the use of complex-valued functions in place of the real electric field $E(t)$. For this purpose we separate the Fourier transform integral of $E(t)$ into two parts. The complex-valued temporal function $E^+(t)$ contains only the positive frequency segment of the spectrum. In communication theory and optics $E^+(t)$ is termed the analytic signal (its complex conjugate is $E^-(t)$ and contains the negative frequency part). By definition $E^+(t)$

and $\tilde{E}^+(\omega)$ as well as $E^-(t)$ and $\tilde{E}^-(\omega)$ are Fourier pairs where only the relations for the positive-frequency part are given as

$$E^+(t) = \frac{1}{2\pi}\int_{-\infty}^{\infty}\tilde{E}^+(\omega)e^{i\omega t}d\omega \tag{2.6}$$

$$\tilde{E}^+(\omega) = \int_{-\infty}^{\infty}E^+(t)e^{-i\omega t}dt \tag{2.7}$$

These quantities relate to the real electric field

$$E(t) = E^+(t) + E^-(t) = 2\mathrm{Re}[E^+(t)] = 2\mathrm{Re}[E^-(t)] \tag{2.8}$$

and its complex Fourier transform

$$\tilde{E}(\omega) = \tilde{E}^+(\omega) + \tilde{E}^-(\omega) \tag{2.9}$$

$E^+(t)$ is complex-valued and can therefore be expressed uniquely in terms of its amplitude and phase

$$\begin{aligned} E^+(t) &= |E^+(t)|e^{i\Phi(t)} = |E^+(t)|e^{i\Phi_0}e^{i\omega_c t}e^{i\Phi_a(t)} \\ &= \sqrt{\frac{I(t)}{2\epsilon_0 cn}}e^{i\Phi_0}e^{i\omega_c t}e^{i\Phi_a(t)} \\ &= \frac{1}{2}A(t)e^{i\Phi_0}e^{i\omega_c t}e^{i\Phi_a(t)} \\ &= E_c(t)e^{i\Phi_0}e^{i\omega_c t} \end{aligned} \tag{2.10}$$

where $E_c(t)$ is the complex-valued envelope function without the absolute phase and without the rapidly oscillating carrier-frequency phase factor, a quantity often used in ultrafast optics. The envelope function $A(t)$ is given by

$$A(t) = 2|E^+(t)| = 2|E^-(t)| = 2\sqrt{E^+(t)E^-(t)} \tag{2.11}$$

and coincides with the less general expression in Eq. (2.1). The complex positive-frequency part $\tilde{E}^+(\omega)$ can be analogously decomposed into amplitude and phase

$$\tilde{E}^+(\omega) = |\tilde{E}^+(\omega)|e^{-i\phi(\omega)} = \sqrt{\frac{\pi}{\epsilon_0 cn}I(\omega)}e^{-i\phi(\omega)} \tag{2.12}$$

where $|\tilde{E}^+(\omega)|$ is the spectral amplitude, $\phi(\omega)$ is the spectral phase and $I(\omega)$ is the spectral intensity proportional to the power spectrum density (PSD) - the familiar quantity measured with a spectrometer. From Eq. (2.3) the relation $-\phi(\omega) = \phi(-\omega)$ is obtained. It is precisely the manipulation of this spectral phase $\phi(\omega)$ in the experiment which - by virtue of the Fourier transformation Eq. (2.6) - creates changes in the real electric field strength $E(t)$ of Eq. (**??**) without changing $I(\omega)$. If the spectral intensity $I(\omega)$ is manipulated as well, additional degrees of freedom are accessible for generating temporal pulse shapes at the expense of lower energy. Note that the distinction between positive- and negative-frequency parts is made for mathematical correctness. In practice only real electric fields and positive frequencies are displayed. Moreover, as usually only the shape and not the absolute magnitude of the envelope functions in addition to the phase function are the quantities of interest, all the prefactors are commonly omitted.

Let us construct the electric field of an optical pulse at a fixed position in space, corresponding to the physical situation of a fixed detector. Assuming linear polarization, we may write the real electric field strength $E(t)$ as a scalar quantity whereas a sinusoidal wave is multiplied with a temporal amplitude or envelope function $A(t)$

$$E(t) = A(t)\cos\left(\Phi_0 + \omega_c t\right) \tag{2.13}$$

with ω_c being the carrier angular frequency, Φ_0 is the absolute phase or carrier-envelope phase. The light frequency is given by $\nu_0 = \omega_c/2\pi$.

The average radiation intensity is given by

$$I(t) = \frac{1}{2}\epsilon_0 cnA(t)^2, \tag{2.14}$$

with ϵ_0 being the vacuum permittivity, c the speed of light and n the refractive index. The factor $1/2$ arises from averaging the oscillations.

In general, we may add an additional time dependent phase function $\Phi_a(t)$ to the temporal phase term in Eq. (2.13)

$$\Phi(t) = \Phi_0 + \omega_c t + \Phi_a(t) \tag{2.15}$$

and define the instantaneous light frequency $\omega(t)$ as

$$\omega(t) = \frac{d\Phi(t)}{dt} = \omega_c + \frac{d\Phi_a(t)}{dt} \tag{2.16}$$

This additional phase function describes variations of the frequency in time, called a "chirp".

The temporal phase $\Phi(t)$ of Eq. (2.15) contains frequency-versus-time information, leading to the definition of the instantaneous frequency $\omega(t)$ Eq. (2.16). In a similar fashion, the spectral phase $\phi(\omega)$ contains time-versus-frequency information and we can define the group delay $T_g(\omega)$, which describes the relative temporal delay of a given spectral component

$$T_g(\omega) = \frac{d\phi}{d\omega} \tag{2.17}$$

Usually the spectral amplitude is distributed around a center frequency (or carrier frequency) ω_c. Therefore - for well-behaved pulses - it is often helpful to expand the spectral phase into a Taylor series

$$\phi(\omega) = \sum_{j=0}^{\infty} \frac{\phi^{(j)}(\omega_c)}{j!}(\omega - \omega_c)^j \tag{2.18}$$

$$\phi(\omega) = \phi(\omega_c) + \phi'(\omega_c)(\omega - \omega_c) + \frac{1}{2}\phi''(\omega_c)(\omega - \omega_c)^2 + \frac{1}{6}\phi'''(\omega_c)(\omega - \omega_c)^3 + ... \tag{2.19}$$

with

$$\phi'(\omega_c) = \left.\frac{\partial\phi(\omega)}{\partial\omega}\right|_{\omega_c} \tag{2.20}$$

The spectral phase coefficient of zeroth order describes in the time domain the absolute phase ($\Phi_0 = -\phi(\omega_c)$). The first-order term leads to a temporal translation of the envelope of the laser pulse in the time domain (the Fourier shift theorem) but not to a translation of the carrier. A positive $\phi'(\omega_c)$ corresponds to a shift towards later times. An experimental distinction between the temporal translation of the envelope via linear spectral phases in comparison to the temporal translation of the whole pulse is, for example, discussed in [120, 121]. The coefficients of higher order are responsible for changes in the temporal structure of the electric field. A positive $\phi''(\omega_c)$ corresponds to a linearly up-chirped laser pulse.

There is a variety of analytical pulse shapes where this formalism can be applied to get analytical expressions in both domains. For general pulse shapes a numerical implementation is helpful. As an example, we will focus on a Gaussian laser pulse $E_{in}^{+}(t)$ (not normalized to pulse energy) with a corresponding spectrum $\tilde{E}_{in}^{+}(\omega)$. Phase modulation in the frequency domain leads to a spectrum $\tilde{E}_{out}^{+}(\omega)$ with a corresponding electric field $E_{out}^{+}(t)$ of

$$E_{in}^{+}(t) = \frac{E_0}{2} e^{-2\ln 2 \frac{t^2}{\Delta t^2}} e^{i\omega_c t} \tag{2.21}$$

Here Δt denotes the FWHM of the corresponding intensity $I(t)$. The absolute phase is set to zero, the carrier frequency is set to ω_c, additional phase terms are set to zero as well. The pulse is termed an unchirped pulse in the time domain. For $\tilde{E}_{in}^{+}(\omega)$ we obtain the spectrum

$$\tilde{E}_{in}^{+}(\omega) = \frac{E_0 \Delta t}{2} \sqrt{\frac{\pi}{2\ln 2}} e^{-\frac{\Delta t^2}{8\ln 2}(\omega-\omega_c)^2} \tag{2.22}$$

The FWHM of the temporal intensity profile $I(t)$ and the spectral intensity profile $I(\omega)$ are related by $\Delta t \Delta\omega = 4\ln 2$, where $\Delta\omega$ is the FWHM of the spectral intensity profile $I(\omega)$. Usually this equation, known as the time-bandwidth product, is given in terms of frequencies ν rather than circular frequencies ω and we obtain

$$\Delta t \Delta\nu = \frac{2\ln 2}{\pi} \simeq 0.441 \tag{2.23}$$

Several important consequences arise from this example and are summarized before we proceed:

1. The shorter the pulse duration, the larger the spectral width. A Gaussian pulse with $\Delta t = 10$ fs centered at 800 nm has a ratio of $\frac{\Delta\nu}{\nu} \approx 10\%$, corresponding to a wavelength interval $\Delta\lambda$ of about 100 nm. Taking into account the wings of the spectrum, a bandwidth comparable to the visible spectrum must be used to create the 10 fs pulse.

2. For a Gaussian pulse the equality in Eq. (2.23) is only reached when the instantaneous frequency (Eq. (2.16)) is time-independent, that is the temporal phase variation is linear. Such pulses are termed Fourier-transform-limited pulses or bandwidth limited pulses.

3. Adding nonlinear phase terms leads to the inequality $\Delta t \Delta \nu \geq 0.441$.

4. For other pulse shapes a similar time-bandwidth inequality can be derived

$$\Delta t \Delta \nu \geq K \tag{2.24}$$

Values of K for different pulse shapes are: Gaussian is 0.441, hyperbolic secant is 0.315, square is 0.886, single side exponential is 0.110, symmetric exponential is 0.142 [116].

One feature of Gaussian laser pulses is that adding the quadratic term $\frac{1}{2}\phi''(\omega_c)\times(\omega-\omega_c)^2$ to the spectral phase function also leads to a quadratic term in the temporal phase function and therefore to linearly chirped pulses. This situation arises for example when passing an optical pulse through a transparent medium as will be shown in next subsection. The complex fields for such laser pulses are given by [122, 123]

$$\tilde{E}^+_{out}(\omega) = \frac{E_0 \Delta t}{2}\sqrt{\frac{\pi}{2\ln 2}} e^{\frac{-\Delta t^2}{8\ln 2}(\omega-\omega_c)^2} e^{-i\frac{1}{2}\phi''(\omega_c)(\omega-\omega_c)^2} \tag{2.25}$$

$$E^+_{out}(t) = \frac{E_0}{2\gamma^{\frac{1}{4}}} e^{\frac{-t^2}{4\zeta\gamma}} e^{i\omega_c t} e^{i(at^2-\epsilon)} \tag{2.26}$$

with $\zeta = \Delta t_{in}^2/8\ln 2$, $\gamma = 1+\phi''^2/4\zeta^2$, $a = \phi''/8\zeta^2\gamma$ and $\epsilon = [\arctan(\phi''/2\zeta)]/2 = -\Phi_0$.

For the pulse duration Δt_{out} (FWHM) of the linearly chirped pulse (quadratic temporal phase function at^2) we obtain the convenient formula

$$\Delta t_{out} = \sqrt{\Delta t^2 + \left(4\ln 2 \frac{\phi''}{\Delta t}\right)^2} \tag{2.27}$$

It is not always advantageous to expand the phase function $\phi(\omega)$ into a Taylor series. Periodic phase functions, for example, are generally not well approximated by polynomial functions. For sinusoidal phase functions of the form $\phi(\omega) = A\sin(\omega\Gamma+\phi_0)$ analytic solutions for the temporal electric field can be found for any arbitrary unmodulated spectrum $\tilde{E}^+_{in}(\omega)$.

2.1.2 Dispersion

Dispersion is the dependence of the phase velocity in a medium on the optical frequency or the propagation mode. There are various different types of dispersion: in *Chromatic dispersion* the phase velocity depends on the optical frequency or wavelength. This can result from a frequency-dependent refractive index, but also from waveguide dispersion. *Intermodal dispersion* results from different propagation characteristics of higher-order transverse modes in waveguides, such as multimode fibers. *Polarization mode dispersion* results from polarization-dependent propagation characteristics. As a result of chromatic dispersion, refraction angles at optical surfaces can be frequency-dependent, leading to *angular dispersion*. This effect can subsequently lead to frequency-dependent path lengths, which can again act like chromatic dispersion.

A main topic in the design of ultrafast laser systems is the minimization of these higher dispersion terms with the help of suitably designed optical systems to keep the pulse duration inside a laser cavity or at the place of an experiment as short as possible. In the following we will discuss the elements that are commonly used for the dispersion management.

Chromatic Dispersion and its Mathematical Description

For the following discussion it is useful to think of an ultrashort pulse as being composed of groups of quasimonochromatic waves, that is of a set of much longer wave packets of narrow spectrum all added together coherently. In vacuum the phase velocity

$$v_p = \omega/k \tag{2.28}$$

and the group velocity

$$v_g = d\omega/dk \tag{2.29}$$

are both constant and equal to the speed of light c, where k denotes the wave number. Therefore an ultrashort pulse will maintain its shape upon propagation in vacuum (no matter how complicated its temporal electric field is). In the following we will always consider a bandwidth-limited pulse entering an optical system such

as, for example, air, lenses, mirrors, prisms, gratings and combinations of these optical elements. Usually these optical systems will introduce dispersion, that is a different group velocity for each group of quasi-monochromatic waves, and consequently the initial short pulse will broaden in time. In this context the group delay $T_g(\omega)$ defined in Eq. (2.17) is the transit time for such a group of monochromatic waves through the system. As long as the intensities are kept low, no new frequencies are generated. This is the area of linear optics and the corresponding pulse propagation has been termed linear pulse propagation. It is convenient to describe the passage of an ultrashort pulse through a linear optical system by a complex optical transfer function [124]

$$\tilde{M}(\omega) = \tilde{R}(\omega)e^{-i\phi_d} \tag{2.30}$$

that relates the incident electric field $\tilde{E}^+_{in}(\omega)$ to the output field

$$\tilde{E}^+_{out}(\omega) = \tilde{M}(\omega)\tilde{E}^+_{in}(\omega) = \tilde{R}(\omega)e^{-i\phi_d}\tilde{E}^+_{in}(\omega) \tag{2.31}$$

where $\tilde{R}(\omega)$ is the real-valued spectral amplitude response describing for example the variable diffraction efficiency of a grating, linear gain or loss or direct amplitude manipulation. The phase $\phi_d(\omega)$ is termed the spectral phase transfer function. This is the phase accumulated by the spectral component of the pulse at frequency ω upon propagation between the input and output planes that define the optical system. It is this spectral phase transfer function that plays a crucial role in the design of ultrafast optical systems.

In the following discussion we will concentrate mainly on pure phase modulation and therefore set $\tilde{R}(\omega)$ constant for all frequencies and omit it initially. To model the system the most accurate approach is to include the whole spectral phase transfer function. Often however only the first orders of a Taylor expansion around the central frequency ω_c are needed.

$$\phi_d(\omega) = \phi_d(\omega_c) + \phi'_d(\omega_c)(\omega-\omega_c) + \frac{1}{2}\phi''_d(\omega_c)(\omega-\omega_c)^2 + \frac{1}{6}\phi'''_d(\omega_c)(\omega-\omega_c)^3 + \ldots \tag{2.32}$$

If we describe the incident bandwidth-limited pulse by $\tilde{E}^+_{in}(\omega) = |\tilde{E}^+(\omega)| \times e^{-i\phi(\omega_c)} \times e^{-i\phi'(\omega_c)(\omega-\omega_c)}$ then the overall overall phase ϕ_{op} of $\tilde{E}^+_{out}(\omega)$ is given by

$$\begin{aligned}\phi_{op}(\omega) = \phi(\omega_c) + \phi'(\omega_c)(\omega-\omega_c) + \phi_d(\omega_c) + \phi'_d(\omega_c)(\omega-\omega_c) \\ + \frac{1}{2}\phi''_d(\omega_c)(\omega-\omega_c)^2 + \frac{1}{6}\phi'''_d(\omega_c)(\omega-\omega_c)^3 + ...\end{aligned} \tag{2.33}$$

As discussed in the context of [119] the constant and linear terms do not lead to a change of the temporal envelope of the pulse. Therefore we will omit in the following these terms and concentrate mainly on the second-order dispersion ϕ'', also termed the group velocity dispersion (GVD) or group delay dispersion (GDD), and the third-order dispersion ϕ''' (TOD) whereas we have omitted the subscript d. Strictly they have units of [fs^2/rad] and [fs^3/rad^2], respectively, but usually the units are simplified to [fs^2] and [fs^3].

Note that in fiber optics a slightly different terminology is commonly used. The propagation constant of a mode in a fiber, often denoted with the symbol β determines how the phase and amplitude of that light with a given frequency varies along the propagation direction z: $A(z) = A(0)\exp(i\beta z)$. It is related to the n-order dispersion by

$$\beta_n = \frac{\frac{d^n\phi_m}{d\omega^n}\Big|_{\omega_c}}{L} \qquad [\mathrm{ps}^n/\mathrm{km}] \tag{2.34}$$

where L denotes the length of the fiber. The dispersion parameter D is a measure for the GDD per unit bandwidth and is given by

$$D = \frac{\omega_c^2}{2\pi c}|\beta_2| \qquad [\mathrm{ps/nm\ km}] \tag{2.35}$$

The dispersion of various orders for a medium can most conveniently be calculated if the refractive index is specified with a kind of Sellmeier formula (see Sect. 2.1.2). Tabulated index data are less suitable, since the numerical differentiation is sensitive to noise.

One distinguishes normal dispersion (for $\phi'' > 0$) and anomalous dispersion (for $\phi'' < 0$). Normal dispersion, where the group velocity decreases with increasing optical frequency, occurs for most transparent media in the visible spectral region. Anomalous dispersion sometimes occurs at longer wavelengths, e.g. in silica (the basis of most optical fibers) for wavelengths longer than the zero-dispersion wavelength of ~ 1.3 μm.

Between wavelength regions with normal and anomalous dispersion, there is a zero dispersion wavelength. The region around this wavelength can be special in some respects, not only concerning weak dispersive pulse broadening.

Dispersion of third and higher order is called higher-order dispersion. When dealing with very broad optical spectra, one sometimes has to consider dispersion up to the fourth or even fifth and sixth order. Ultimately, the concept of Taylor expansion loses its value in this regime, where many dispersion orders have to be considered. It is therefore often more convenient e.g. in numerical modeling to work directly with a table of frequency-dependent phase changes.

Sellmeier Formula

For the specification of a wavelength-dependent refractive index of a transparent optical material, it is common to use a so-called Sellmeier formula [125] (also called Sellmeier equation or Sellmeier dispersion formula, after *W. Sellmeier*). This is typically of the form

$$n(\lambda) = \sqrt{1 + \sum_j \frac{A_j \lambda^2}{\lambda^2 - B_j}} \tag{2.36}$$

with the coefficients A_j and B_j. For example, the refractive index of fused silica can be calculated as [126]

$$n_{fs}(\lambda) = \sqrt{1 + \frac{0.6961663\lambda^2}{\lambda^2 - 0.0684043^2} + \frac{0.4079426\lambda^2}{\lambda^2 - 0.1162414^2} + \frac{0.8974794\lambda^2}{\lambda^2 - 9.89661^2}} \tag{2.37}$$

where the wavelength in micrometers has to be inserted (see Fig. 2.1a).

Such equations are very useful, as they make it possible to describe fairly accurately the refractive index in a wide wavelength range with only a few so-called Sellmeier coefficients, which are usually obtained from measured data with some least-square fitting algorithm. Sellmeier coefficients for many optical materials are available in databases. Some caution is advisable when applying Sellmeier equations in extreme wavelength regions; unfortunately, the validity range of available data is often not indicated.

Sellmeier data are also very useful for evaluating the chromatic dispersion of a material. This involves frequency derivatives, which can be performed analytically

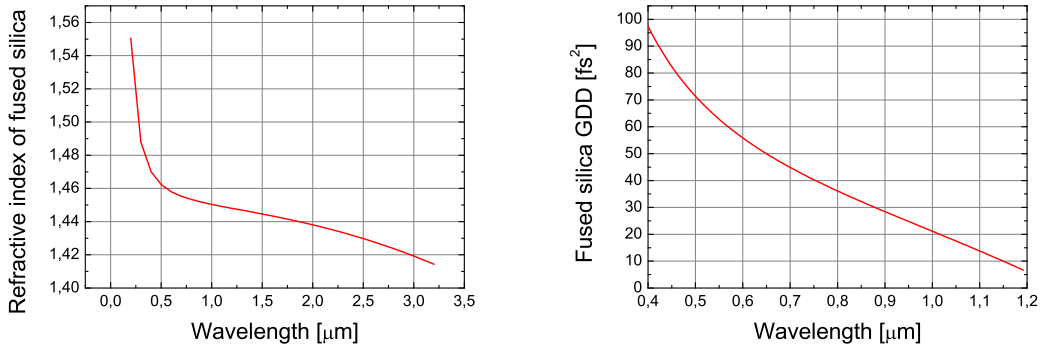

(a) (b)

Figure 2.1: (a) Refractive index of fused silica. (b) GDD of a fused silica for the beam path in a glass L=1 mm.

with Sellmeier data even for high orders of dispersion, whereas numerical differentiation on the basis of tabulated index data is sensitive to noise. As the example, the calculated GDD of fused silica is presented in Fig. 2.1b.

The literature contains a great variety of modified equations which are also often called Sellmeier formula. Extensions to the simple form give above can enlarge the wavelength range of validity, or make it possible to include the temperature dependence of refractive indices. This can be important, for example, for calculating phase-matching configurations for nonlinear frequency conversion.

2.1.3 Managing of the Temporal Shape via the Frequency Domain

Dispersion due to Transparent Media

A pulse traveling a distance L through a medium with index of refraction $n(\omega)$ accumulates the spectral phase

$$\phi_m(\omega) = k(\omega)L = \frac{\omega}{c} n(\omega)L \tag{2.38}$$

which is the spectral transfer function due to propagation in the medium as defined above. The first derivative

$$\frac{d\phi_m}{d\omega} = \phi'_m = \frac{d(kL)}{d\omega} = L\left(\frac{d\omega}{dk}\right)^{-1} = \frac{L}{v_g} = T_g \tag{2.39}$$

yields the group delay T_g and describes the delay of the peak of the envelope of the incident pulse. Usually the index of refraction $n(\omega)$ is given as a function of wavelength λ, i.e., $n(\lambda)$. Eq. (2.39) then reads

$$T_g = \frac{d\phi_m}{d\omega} = \frac{L}{c}\left(n + \omega\frac{dn}{d\omega}\right) = \frac{L}{c}\left(n - \lambda\frac{dn}{d\lambda}\right) \tag{2.40}$$

As different groups of the quasi-monochromatic waves move with different group velocities the pulse will be broadened. For second-order dispersion in a transparent media we obtain the)

$$\mathrm{GDD_{tm}} = \phi''_m = \frac{d^2\phi_m}{d\omega^2} = \frac{L}{c}\left(2\frac{dn}{d\omega} + \omega\frac{d^2n}{d\omega^2}\right) = \frac{\lambda^3 L}{2\pi c^2}\frac{d^2n}{d\lambda^2} \tag{2.41}$$

For ordinary optical glasses in the visible range we encounter normal dispersion, i. e., red parts of the laser pulse will travel faster through the medium than blue parts. So the symmetric temporal broadening of the pulse due to ϕ'' will lead to a linearly up-chirped laser pulse. In these cases the curvature of $n(\lambda)$ is positive (upward concavity) emphasizing the terminology that positive GDD leads to up-chirped pulses.

For the TOD in a transparent media we obtain

$$\mathrm{TOD_{tm}} = \phi'''_m = \frac{d^3\phi_m}{d\omega^3} = \frac{L}{c}\left(3\frac{d^2n}{d\omega^2} + \omega\frac{d^3n}{d\omega^3}\right) = \frac{-\lambda^4 L}{2\pi^2 c^3}\left(3\frac{d^2n}{d\lambda^2} + \lambda\frac{d^3n}{d\lambda^3}\right) \tag{2.42}$$

Empirical formulas for $n(\lambda)$ such as Sellmeiers equations are usually tabulated for common optical materials so that all dispersion quantities in Eq. (2.40), (2.41), (2.42) can be calculated.

Angular Dispersion

Transparent media in the optical domain possess positive group delay dispersion leading to up-chirped femtosecond pulses. To compress these pulses, optical systems are needed that deliver negative group delay dispersion, that is systems where

the blue spectral components travel faster than the red spectral components. Convenient devices for that purpose are based on angular dispersion delivered by prisms and gratings.We start our discussion again with the spectral transfer function [124]

$$\phi(\omega) = \frac{\omega}{c} P_{op}(\omega) \tag{2.43}$$

where P_{op} denotes the optical path length. Eq. (2.43) is the generalization of Eq. (2.38). The GDD is given by

$$\mathrm{GDD}_{\mathrm{ang}} = \frac{1}{c}\left(2\frac{dP_{op}}{d\omega} + \omega\frac{d^2P_{op}}{d\omega^2}\right) = \frac{\lambda^3}{2\pi c^2}\frac{d^2P_{op}}{d\lambda^2} \tag{2.44}$$

and is similar to Eq. (2.41). In a dispersive system the optical path from an input reference plane to an output reference plane can be written

$$P_{op} = l\cos\alpha \tag{2.45}$$

where $l = l(\omega_c)$ is the distance from the input plane to the output plane for the center frequency ω_c and α is the angle of rays with frequency ω with respect to the ray corresponding to ω_c. In general, it can be shown [124] that the angular dispersion produces negative GDD

$$\mathrm{GDD}_{\mathrm{ang}} \approx -\frac{l\omega_c}{c}\left(\left.\frac{d\alpha}{d\omega}\right|_{\omega_c}\right)^2 \tag{2.46}$$

For pairs of elements (prisms or gratings) the first element provides the angular dispersion and the second element recollimates the spectral components. Using two pairs of elements permits the lateral displacement of the spectral components (spatial chirp) to be canceled out and recovers the original beam profile.

Dispersion due to Interference: Gires-Tournois Interferometers and Chirped Mirrors

A Gires-Tournois interferometer (GTI) [127] is a special case of a Fabry-Pérot interferometer in which one mirror (M1) is a 100% reflector and the top mirror (M2) is a low reflector, typically with a reflectivity of a few percent (Fig. 2.2). The group delay dispersion of such a device is given by (see for example [128] or [129])

$$\mathrm{GDD}_{\mathrm{GTI}} = \frac{-2t_0^2(1-R)\sqrt{R}\sin\omega t_0}{(1+R-2\sqrt{R}\cos\omega t_0)^2} \tag{2.47}$$

where $t_0 = (2nd\cos\theta)/c$ is the round-trip time of the Fabry-Pérot [130], n is the refractive index of the material between the two layers, d is the thickness of the interferometer and θ is the internal angle of the beam between the layers. In this formula material dispersion is neglected and R is the intensity reflectivity of the top reflector. The group delay dispersion can be conveniently tuned either by tilting the device or by changing the interferometer spacing. Increasing t_0 increases the dispersion, but at the same time reduces the frequency range over which the group delay dispersion is constant. These devices are typically used in applications employing pulses larger than 100 fs. For picosecond pulses the mirror spacing is on the order of several mm, for femtosecond lasers the spacing has to be on the order of a few μm. In order to overcome the limitations for femtosecond applications, GTIs were constructed on the basis of dielectric multilayer systems [131]. The corresponding spectral transfer functions can be found in [117].

Compared to prism compressors GTI mirrors reduce the intra-cavity losses resulting in higher output power of the laser.

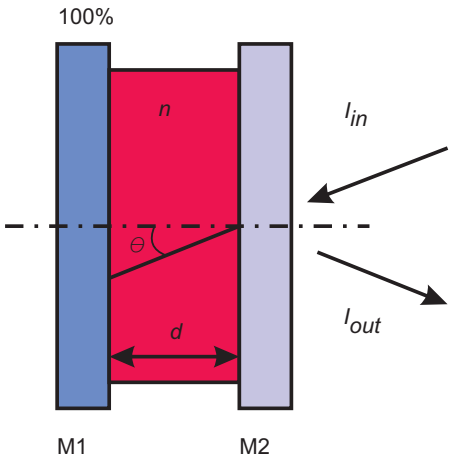

Figure 2.2: Schematic diagram of a Gires-Tournois interferometer (GTI)

The alternative to GTI are specially designed dielectric multilayer mirrors. Usually a dielectric mirror consists of alternating transparent pairs of high-index

and low-index layers where the optical thickness of all layers is chosen to be equal to 1/4 of the Bragg wavelength λ_B. Interference of the reflections at the index discontinuities add up constructively for the Bragg wavelength. If the optical thickness of the layers along the mirror structure is varied, then the Bragg wavelength depends on the penetration depth.

The Bragg wavelength does not have to be varied linearly with the penetration depth. In principle chirp laws $\lambda_B(z)$ can be found for compensation of higher-order dispersion in addition. It was realized, that the desired dispersion characteristics of the chirped mirrors can be spoiled by spurious effects originating from multiple reflections within the coating stack and at the interface to the ambient medium, leading to dispersion oscillations (see the discussion on GTI). An exact coupled-mode analysis [132] was used to develop a so-called double-chirp technique in combination with a broadband antireflection coating, in order to avoid the oscillations in the group delay dispersion. Using accurate analytical expressions double chirped mirrors could be designed and fabricated with a smooth and custom-tailored group delay dispersion [133] suitable for generating pulses in the two optical cycles regime directly from a Ti:Sa laser [84]. Double chirping has the following meaning: in conventional chirped mirrors, equal optical lengths of high-index (hi) and low-index (lo) material within one period are employed, i. e., $P_{lo} = P_{hi} = \lambda_B/4$. Double chirping keeps the duty cycle η as an additional degree of freedom under the constraint: $P_{lo} + P_{hi} = (1-\eta)\lambda_B/2 + \eta\lambda_B/2 = \lambda_B/2$.

2.1.4 Waveguide Dispersion

The discussion above is based on the assumption of plane waves. In practice, significant deviations from this situation can occur, in particular in the context of waveguides. Here, the quantity of interest is usually not the magnitude of the k vector (which anyway is no longer well defined), but rather the propagation constant β, which specifies the phase change per unit length in the propagation direction (see Eq. (2.34)). As the propagation constant is influenced by the waveguide (particularly for mode diameters of only a few wavelengths or even less), the dispersion is also affected. This is important e.g. in optical fibers, and particularly in photonic crystal fibers with very small effective mode areas. In some cases, waveguide dispersion makes the overall dispersion anomalous even in the visible

wavelength region, where the material dispersion of silica alone is clearly in the normal dispersion regime. For telecom applications, fiber designs are often made for tailored dispersion properties, resulting in, e.g., dispersion-shifted fibers.

2.1.5 Measurement of Chromatic Dispersion

There are several techniques for measuring chromatic dispersion:

1. The pulse delay technique [134] (for fibers) is based on measuring the difference in propagation time (group delay) for pulses with different center wavelengths. This is typically done using hundreds of meters (or even some kilometers) of a fiber. The dispersion is obtained by differentiation of these data.

2. The phase shift technique or"difference method" [135] (also for fibers): a light beam with a sinusoidally modulated intensity is sent through a fiber, and the phases of the oscillations of input and output power are compared. The group delay can be calculated from that phase, and the dispersion can be measured by performing the measurement at different wavelengths.

3. Dispersion in the resonator of a wavelength-tunable passively mode-locked laser can be measured by monitoring changes in the pulse repetition frequency when the laser wavelength is changed, as this reveals the wavelength-dependent group delay.

4. Different types of interferometry [136] (e.g. white-light interferometry [137] or spectral phase interferometry [138]) can be used to measure the phase delay caused by a dispersive component. The dispersion properties can be obtained from this phase by numerical differentiation. The method is normally used for dispersion measurements on dispersive laser mirrors and sometimes for fibers.

2.2 Laser Mode-Locking

Mode-locking is a laser operation regime in which many longitudinal modes of the cavity are simultaneously forced to oscillate with a precise phase relation so that

the output laser beam shows a repetitive train of ultrashort optical pulses [74,139]. To achieve mode-locking operation, a suitable device, which is usually referred to as the mode locker, must be placed inside the cavity. For a given laser medium, the lower limit to the achievable pulse duration $\Delta\tau_p$ is set by the gain line width ($\Delta\tau_p \geq 1/\Delta\nu_0$), whereas the pulse repetition rate $1/\tau_p$ is usually equal to the difference frequency between two consecutive longitudinal modes $\Delta\nu$ (or an integer multiple of $\Delta\nu$, as for harmonic mode-locking). Therefore, pulse duration, depending upon the gain line width, usually ranges from about 1 ns, in gas lasers, down to 10 fs in broad-bandwidth solid-state lasers. Pulse repetition rate depends, of course, upon the cavity length and usually ranges from about 100 MHz to a few GHz.

2.2.1 Mode-locking: Time- and frequency-domains of mode-locked laser

Consider an ideal pulse circulating in the laser cavity

$$E(t) = \mathrm{Re}[A(t)\exp(-i\omega_c t)] \tag{2.48}$$

where, $A(t)$ - pulse envelope, ω_c - carrier frequency. The laser radiation is a sequence of pulses, which are copies of the same pulse (Fig. 2.3). Time between pulses $T_0 = 2L/v_g$, where v_g - pulse propagation velocity in the cavity (group velocity). However, the pulses are not quite identical, because their envelope propagates with the velocity v_g (see Eq. (2.29)), and a carrier wave with ω_c with the phase velocity. As a result, after each resonator round-trip a carrier wave acquires a phase shift $\Delta\phi$ with respect to the envelope of $A(t)$, i.e., electric field is not a periodic function. We assume, however, that the envelope of the pulse is a periodic function:

$$A(t) = A(t - T_0) \tag{2.49}$$

In this case, the field of laser radiation can be written as

$$E(t) = \mathrm{Re}\Big\{\sum_m A_m \exp\left[-i(\omega_c + m\omega_r)t\right]\Big\} \tag{2.50}$$

where A_m are the Fourier components of $A(t)$; $\omega_{rep} = 2\pi/T_0$ - angular frequency of pulse repetition. Represent ω_c like $\omega_c = \omega_{CEO} + p\omega_{rep}$, where p - integer, and

$\omega_{CEO} < \omega_{rep}$. Changing a numeration of mode ($n = p + m, n = 0, 1, 2, ...$), we get

$$E(t) = \mathrm{Re}\Big[\sum_n A_n \exp(-i\omega_n t)\Big] \tag{2.51}$$

where

$$\omega_n = n\omega_{rep} + \omega_{CEO}; \tag{2.52}$$

ω_{CEO} and ω_{rep} - microwave frequencies; $n \simeq 10^5 - 10^6$. Thus, spectrum of fs laser radiation can be represented by a set of equidistant frequencies with interval ω_{rep} (see Fig. 2.3). In this case, the OFC emitted frequencies (solid line) has an initial detuning ω_{CEO} relative to the provisions of the frequencies obtained by multiplying ω_{rep} an integer (dashed line). The appearance of ω_{rep} associated with the difference of the phase and group velocities of propagation of the laser pulse in the cavity. During traversal of the cavity phase shift $\Delta\phi = \omega_c T = 2\pi\omega_c/\omega_{rep}$. The frequency of n-th mode (in Hertz) is defined by Eq. (1.2) where $f_{CEO} = \omega_c/2\pi$; $f_{rep} = \omega_{rep}/2\pi$.

It turned out that considered idealized case is realized in fs laser with a high degree of accuracy. Checking of frequencies equidistant was done in [29].

2.2.2 Kerr lens mode-locking

This technique is based on the use of a nonlinear loss element simply consisting of a nonlinear Kerr medium placed in front of an aperture (Fig. 2.4). The nonlinear medium shows, via the optical Kerr effect, an intensity-dependent refractive index $n = n_0 + n_2 I$, where n_0 is the linear refractive index of the medium, I is the local light intensity and n_2 is a positive coefficient (for a self-focusing medium) which depends on the strength of the nonlinearity (e.g., $n_2 \simeq 4.5 \times 10^{-16}$ cm^2/W for fused quartz and $n^2 \simeq 3.45 \times 10^{-16}$ cm^2/W for sapphire). A light beam with, e.g., a transverse Gaussian intensity distribution $I(r) = I_p \exp[-2(r/w)^2]$ that crosses a thin slice of the Kerr medium of length l thus experiences a transversely varying phase shift

$$\delta\phi \approx 2\pi l n_2 I(r)/\lambda) = (2\pi l n_2/\lambda) I_p \exp[-2(r/w)^2] \tag{2.53}$$

Close to the beam center $r = 0$, one can write

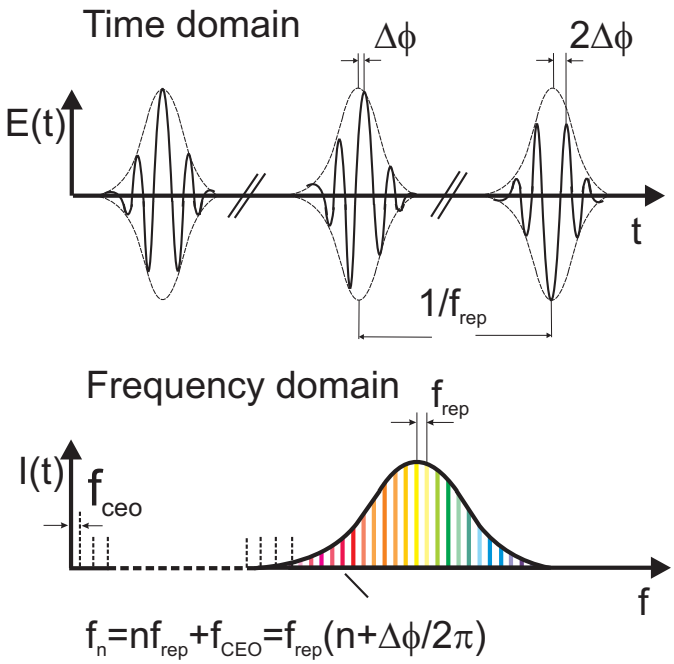

Figure 2.3: The basic time-and frequency-domain representations of the output of a mode-locked fs laser. Pulses are emitted at the rate f_{rep}, but because of dispersion in the laser cavity, the carrier advances with respect to the envelope by $\Delta\phi$ from one pulse to the next. In the frequency domain, the result of this phase slip is an offset common to all modes of $f_{CEO} = f_{rep}\Delta\phi/(2\pi)$ (see Eq. (2.61)).

$$\delta\phi \approx (2\pi l n_2 I_p/\lambda)[1 - 2(r/w)^2], \tag{2.54}$$

i. e., the thin medium introduces a quadratic phase change of the field and thus acts, for $n_2 > 0$, as a positive lens (called a Kerr lens) of dioptric power

$$1/f = 4n_2 l I_p/(n_0 w^2), \tag{2.55}$$

which increases as the beam intensity I_p increases. If an aperture is placed at some suitable distance from the Kerr medium, a beam with higher intensity will be focused tighter and a higher fraction of the beam will be transmitted through the aperture. Therefore, the Kerr medium with the aperture, like a fast saturable absorber, introduces losses that decrease when the instantaneous pulse intensity is

increased, thus leading to mode-locking. Note that, by appropriately controlling the cavity dispersion, the shortest mode-locked pulses ($\approx$ 6 fs) have been achieved by this technique for Ti^{3+}:Al_2O_3 lasers.

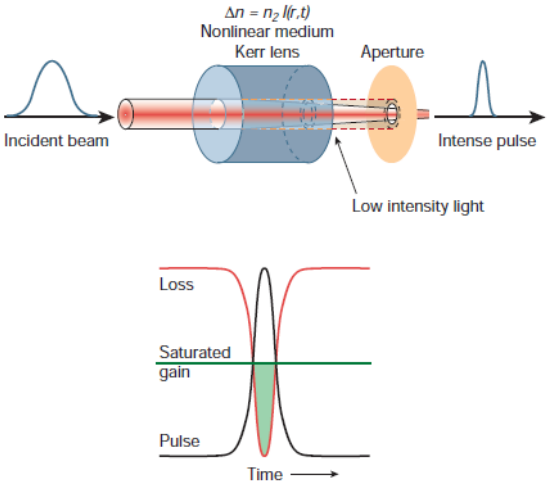

Figure 2.4: Kerr lens mode-locking is obtained through a Kerr lens at an intracavity focus in the gain medium or in another material. In combination with a hard aperture inside the cavity, the cavity design is made such that the Kerr lens reduces the laser mode area for high intensities at the aperture and therefore forms an effective fast saturable absorber. After [140].

2.3 Principle of measurement of optical frequency

After discussing the frequency spectrum of a mode-locked laser, we now turn to the measurement of the absolute frequencies of OFC lines. For a frequency measurement to be absolute, it must be referenced to the hyperfine transition of ^{133}Cs that defines the second. From the relations listed above, we see that determining the absolute optical frequencies of the femtosecond OFC requires two RF measurements, that of f_{rep} and f_{CEO}. Measurement of f_{rep} is straightforward: we simply detect the pulse train's repetition rate (from tens of megahertz to several gigahertz) with a fast photodiode. On the other hand, measurement of f_{CEO} is

more involved as the pulse-to-pulse-carrier-envelope phase shift requires an interferometric measurement, either in the time domain or in the frequency domain. When the optical spectrum spans an octave in frequency, i.e., the highest frequencies are a factor of two larger than the lowest frequencies, measurement of f_{CEO} is greatly simplified. If we use a second harmonic crystal to frequency double a OFC line, with index n, from the low-frequency portion of the spectrum, it will have approximately the same frequency as the OFC line on the high-frequency side of the spectrum with index $2n$. Measuring the heterodyne beat between these two families of OFC lines yields a difference,

$$2\nu_n - \nu_{2n} = 2(nf_{rep} + f_{CEO}) - (2nf_{rep} + f_{CEO}) = f_{CEO}, \tag{2.56}$$

which is just the offset frequency. Thus an octave-spanning spectrum enables a direct measurement of f_{CEO}. However, an octave-spanning spectrum is not required; it just represents the simplest approach. This scheme is designated as "self-referencing" since it uses only the output of the mode-locked laser as shown in (Fig. 2.5(a)).

Self-referencing is not the only scheme for determining the absolute optical frequencies given by an octave-spanning spectrum. For example, the absolute optical frequency of a cw laser can be determined if its frequency lies close to OFC line n in the low-frequency portion of the fs OFC spectrum. Then the second harmonic of the cw laser will be positioned close to the OFC line $2n$. Measurement of the heterodyne beat between the cw laser frequency, ν_{ref}, and the OFC line n gives $f_b = \nu_{ref} - (nf_{rep} + f_{CEO})$ and between the second harmonic of the cw laser and OFC line $2n$ gives $f_{b2} = 2\nu_{ref} - (2nf_{rep} + f_{CEO})$. Mixing the beats with appropriate weighting factors gives $f_{b2} - 2f_{b1} = 2\nu_{ref} - (2nf_{rep} + f_{CEO}) - (2\nu_{ref} - 2(nf_{rep} + f_{CEO})) = f_{CEO}$, which represents the second detection scheme shown in Fig. 2.5(b). Another interesting fact is that by mixing the two beat signals, one establishes a direct link between the optical and RF frequencies (ν_{ref} and f_{rep}) as in $f_{b2} - f_{b1} = 2\nu_{ref} - (2nf_{rep} + f_{CEO}) - \nu_{ref} + (nf_{rep} + f_{CEO}) = \nu_{ref} - nf_{rep}$.

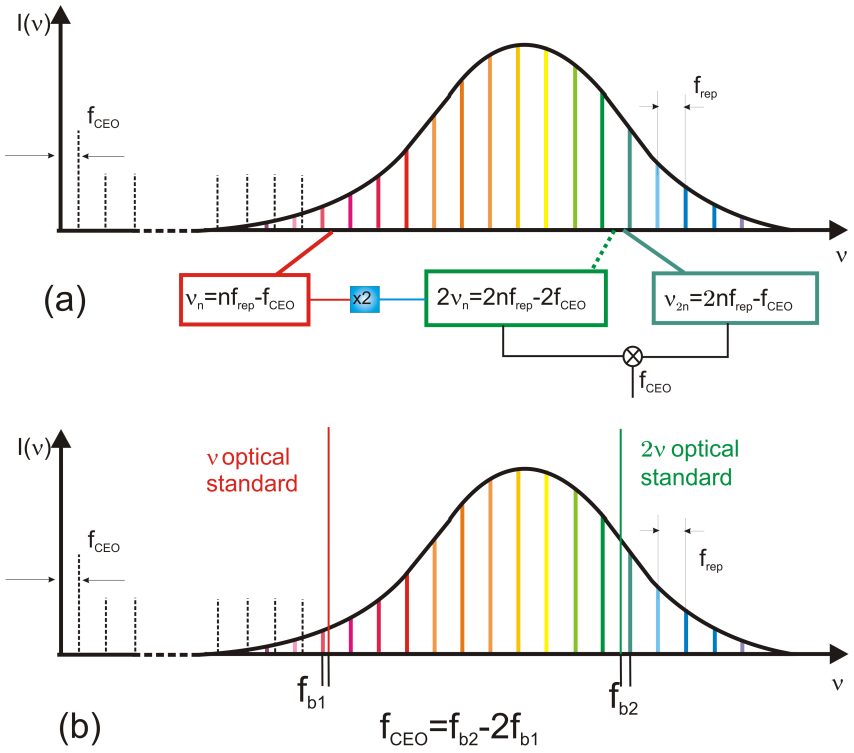

Figure 2.5: Two equivalent schemes for the measurement of f_{CEO} using an octave-spanning OFC. In the self-referencing approach, shown in (a), frequency doubling and comparison are accomplished with the OFC itself. In the second approach shown in (b), the fundamental frequency (ν-standard) and its second harmonic of a cw optical standard are used to determine f_{CEO}. These two basic schemes are employed for absolute optical frequency measurement and implementation of optical atomic clocks.

2.4 Supercontinuum Generation

Supercontinuum generation is a process where laser light is converted to light with a very broad spectral bandwidth (i.e., low temporal coherence), whereas the spatial coherence usually remains high. The spectral broadening is usually accomplished by propagating optical pulses through a strongly nonlinear device, such as an optical fiber. Of special interest are photonic crystal fibers, mainly due to their unusual chromatic dispersion characteristics, which can allow a strong nonlinear

interaction over a significant length of fiber. Even with fairly moderate input powers, very broad spectra are achieved; this leads to a kind of "laser rainbow". In some cases, tapered fibers can also be used.

2.4.1 The Physics of Supercontinuum Generation

The physical processes behind supercontinuum generation in fibers can be very different, depending particularly on the chromatic dispersion and length of the fiber (or other nonlinear medium), the pulse duration, the initial peak power and the pump wavelength. When femtosecond pulses are used, the spectral broadening can be dominantly caused by self-phase modulation. In the anomalous dispersion regime, the combination of self-phase modulation and dispersion can lead to complicated soliton dynamics, including the split-up of higher-order solitons into multiple fundamental solitons (soliton fission). For pumping with picosecond or nanosecond pulses, Raman scattering and four-wave mixing can be important. Supercontinuum generation is even possible with continuous-wave beams, when using multi-watt laser beams in long fibers; Raman scattering and four-wave mixing are very important in that regime.

The noise properties of the generated continua can also be very different in different parameter regions. In some cases, e.g. with self-phase modulation being the dominant mechanism and the dispersion being normal, the process is very deterministic, and the phase coherence of the generated supercontinuum pulses can be very high, even under conditions of strong spectral broadening. In other cases (e.g. involving higher-order soliton effects), the process can be extremely sensitive to the slightest fluctuations (including quantum noise) e.g. in the input pulses, so that the properties of the spectrally broadened pulses vary substantially from pulse to pulse.

The strongly nonlinear nature of supercontinuum generation makes it difficult to understand intuitively all the details of the interaction, or to predict relations with analytical tools. Therefore, much of the underlying physics describing supercontinuum generation can be described within the framework of the one-dimensional nonlinear envelope equation (NEE) [141] with the inclusion of the effects of stimulated Raman scattering.

Nonlinear envelope equation

In this model, the pulse is assumed to propagate along the z-axis with a wave vector amplitude $k_0 = n_0\omega_c/c$ where n_0 is the linear refractive index of the material at the central frequency ω_c of the pulse [142]. For an input pulse with a peak amplitude A_0 and a pulse duration τ_p, the equation for the normalized amplitude $u(z,t) = A(z,t)/A_0$ can be expressed as [143]

$$\frac{\delta u}{\delta \xi} = -i\mathrm{sgn}(\beta_2)\sum_{n=2}\frac{L_{ds}}{L_{ds}^{(n)}} + i\left(1 + \frac{i}{\omega_c\tau_p}\frac{\partial}{\partial\tau}\right)p_{nl} \tag{2.57}$$

where $L_{ds} = \tau_p^2/|\beta_2|$ is the dispersion length, $\xi = z/L_{ds}$ is the normalized propagation distance, β_2 is the GDD, $L_{ds}^{(n)} = \tau_p^n/\beta_n$ is the nth-order dispersion length, $\tau = (t - z/v_g)/\tau_p$ is the normalized retarded time for the pulse traveling at the group velocity v_g, and p_{nl} is the normalized nonlinear polarization. Inclusion of both instantaneous (i.e., electronic) and noninstantaneous (i.e., nuclear) nonlinear refractive index changes in the nonlinear polarization yields [143]

$$p_{nl} = \frac{L_{ds}}{L_{nl}}\left[(1-f)|u|^2 + f\int_{-\infty}^{\tau} d\tau' g(\tau-\tau')|u|^2\right]u, \tag{2.58}$$

where $L_{nl} = (c/\omega_c n_2 I_0)$ is the nonlinear length, $I_0 = n_0 c|A_0|^2/2\pi$ is the peak input intensity, f is the fractional contribution of Raman scattering to the nonlinear refractive index, and $g(\tau)$ is the Raman-response function [144, 145].

The presence of the operator $1 + i\partial/\omega_c\tau_p\partial\tau$ in the nonlinear polarization term accounts for self-steepening effects and allows for the modeling of the propagation of pulses with spectral widths comparable to the ω_c.

Spectral superbroadening

For a fs pulse propagating in a fiber, the central wavelength of the pulse relative to the zero-GDD point strongly determines the nature of the spectral broadening and supercontinuum generation. For the case in which the bandwidth of the pulse overlaps the zero-GDD point, the qualitative characteristics of the supercontinuum generation can be attributed to the combined action of self-phase modulation and third-order dispersion [142, 146].

The temporal profile of femtosecond pulse in microstructure fiber is highly complicated. However, after its propagation on a certain distances some substruc-

ture is visible and can be understood as arising from the formation of well-defined pulses, known as soliton fission [142], that is accompanied by nonsolitonic radiation at the short-wavelength side. Although stimulated Raman scattering and self-steepening result in quantitative changes in the spectrum, in the limit where the GDD is small, the basic shape of the supercontinuum spectrum depends primarily on the amount of third-order dispersion and, to a lesser extent, the amount of fourth-order dispersion.

2.4.2 Coherence Properties

It is worth spending some thoughts on the coherence properties of supercontinuum. The spatial coherence (considering the cross-spectral density) is usually very high, particularly when the source involves a single-mode fiber. On the other hand, the high spectral bandwidth suggests a very low temporal coherence. However, supercontinuum generated from periodic pulse trains can still have a high temporal coherence in the sense that there can be a strong correlations between the electric fields corresponding to different pulses, if the spectral broadening mechanism is highly reproducible. This kind of coherence is in fact very important for the generation of OFCs in photonic crystal fibers, and it may or may not be achieved depending on parameters such as the seed pulse duration and energy, fiber length, and fiber dispersion.

The initially surprising discrepancy between high bandwidth and high temporal coherence can be resolved by realizing the shape of the field correlation function: it has a very narrow peak around zero time delay (with a width of e.g. a few femtoseconds), but there are also additional peaks with comparable height at time delays corresponding to integer multiples of the pulse period. Hence there is low temporal coherence in the sense of vanishing correlations for most time delays, but high temporal coherence in the sense of strong correlations for some large time delays.

2.5 Octave-spanning OFC

In recent years a new type of extremely broadband fs laser, that is able to generate an octave-spanning spectrum without external broadening in PFC, has been

realized. The definition of "octave spanning" has to be explained. The span of a spectrum is often taken as the width at some power below the peak (often full-width at half-maximum or perhaps even at the 10 dB points). However, for fs OFC applications, there is a good operational definition of octave-spanning, namely that it is possible to obtain f-$2f$ beats. A slightly stronger version of this is that the beats are sufficiently strong to be used to stabilize the offset frequency of the laser. This criterion can be met even when the intensity at the octave points is as much as 40 dB below the peak.

To get an idea of how this laser functions, it is helpful to review the two practical routes towards shorter pulses and broader spectra in a fs laser.

One approach is to engineer the dispersion inside the resonator in a way that short pulses with extremely broad spectra do not spread in time during a cavity round trip. This involves careful design of mirrors to have negative GDD over the desired large bandwidth and compensate for the positive-gain crystal dispersion with a low net-higher-order dispersion. This approach has been taken with great success by *Ell* et al. [147]. Their carefully engineered intracavity dispersion is capable of generating spectra exceeding one octave with 5 fs pulses at a repetition rate of 64 MHz.

However, in the presence of the narrow bandwidth of the chirped mirrors, both with respect to their dispersive and reflective properties, this limit is inapplicable. Alternatively, one can allow higher-order dispersion in the resonator but, at the same time, ensure that the leading and trailing edges of the temporally spreading spectrum are sufficiently suppressed, such that only a short pulse remains stable in the cavity. This effect can be attained by employing an effective fast saturable absorber. In the case of Ti:Sa lasers, this effective saturable absorber is provided by a soft aperture KLM. While this effect is actually a self-gain modulation, it can theoretically be treated as an equivalent fast saturable absorber. These effects are more generally referred to as self-amplitude modulation (SAM).

There are indications that the broadband laser operates in the limit of an increased SAM. The strongest support for this idea is the experimental observation that the mode-locked output power and the continuous output power of the laser differ by more than an order of magnitude. This difference indicates that the Kerr-lens-induced effective saturable absorber has a saturable absorption of approximately 30%. Theoretical calculations of the change in beam waist diameter

inside the gain medium (i.e., the soft-aperture Kerr-lens effect) show that replacing flat mirror with a slightly convex mirror can increase the SAM of pulses circulating in the ring cavity.

2.6 OFC dynamics

As was mentioned before, a OFC has two degrees of freedom: f_{CEO} and f_{rep}. While the spacing of the frequencies is simply determined by the repetition rate of the laser and can be relatively easily controlled, the f_{CEO} is governed by phase differences between the carrier and the envelope of the pulses during one round trip through the laser cavity. This CEO phase $\Delta\phi_{CEO}$ is measured via heterodyning different harmonics of the mode-locked laser spectrum. In an unstabilized laser, this $\Delta\phi_{CEO}$ exhibits very strong noise and can fluctuate several thousand radians in only one second.

2.6.1 $\Delta\phi_{CEO}$ and f_{CEO} in the time domain

The envelope travels at v_g and repeats itself after the cavity round-trip time T_R. The underlying carrier propagates at phase velocity v_p. Generally, $v_p \neq v_g$ in any dispersive medium. This means that the electric field structure of the pulse will undergo a permanent change. The drift of the relative phase between carrier and envelope can be tracked down to the $dn/d\omega$ term in the definition of the group velocity.

When propagating through a dispersive material with an index of refraction $n(z)$ along the axis z, the pulse will accumulate a phase offset between the carrier and envelope of [148]

$$\Delta\phi_{CEO} = \left[\frac{2\pi}{\lambda}\int_0^L n_g(z) - n(z)dz\right] \mathrm{mod} 2\pi = \left[\frac{\omega^2}{c}\int_0^L \frac{dn(z)}{d\omega}dz\right] \mathrm{mod} 2\pi \quad (2.59)$$

Here L is the length of the dispersive material, $n_g = n + (\omega db/d\omega)$. For the case of a linear cavity, L takes the role of twice the cavity length, and the $\Delta\phi_{CEO}$ is the change of the phase ϕ_{CEO} per round trip:

$$\Delta\phi_{CEO}(t) = \Phi_{CEO}(t) - \Phi_{CEO}(t - T_R) \quad (2.60)$$

The CEO phase $\Delta\phi_{CEO}$ must not be confused with the phase Φ_{CEO} , which is typically defined such that a pulse with $\Phi_{CEO} = 0$ has the largest possible value of the electric field [37]. It is useful to introduce the f_{CEO} [149],

$$f_{CEO} = \frac{\Delta\phi_{CEO}}{2\pi} f_{rep} \tag{2.61}$$

where f_{rep} equals the inverse round-trip time $1/T_R$ of the cavity and f_{CEO} is time dependent unless the intracavity dispersion and the cavity length are absolutely constant with time. Changes of f_{CEO} or $\Delta\phi_{CEO}$ tend to be unnoticeably small on a pulse-to-pulse time scale but can reach significant magnitudes on millisecond time scales, rendering stabilization of these parameters a nontrivial task.

2.6.2 The elastic tape model or fixed point formalism

As the pulses follow each other at a constant delay T_R, their spectrum consists of a OFC of equidistantly spaced frequencies with a separation $f_{rep} = 1/T_R$. This OFC must not be confused with the modes of a linear cavity, which are only equidistant in the absence of intracavity dispersion. In contrast, if the spacing between the teeth in the mode-locked OFC were not constant, different Fourier components of the pulse in Fig. 2.3 would travel at different repetition rates inside the cavity, and the pulse would slowly drift apart. The fact that the separation of the frequencies is constant over the entire OFC has been experimentally checked to better than 10^{-15} [29].

Differing phase and group velocity cause a translation of the entire OFC by the f_{CEO}. The frequencies of the nth OFC component can therefore be written in the form of the Eq. (1.2), that leaves only two degrees of freedom for the dynamics of the OFC, translation via f_{CEO} and breathing via f_{rep} as illustrated in Fig. 2.6. Any kind of perturbation of the cavity, e.g., by a thermal change of the refractive index of the laser crystal, will typically affect both the f_{rep} and the f_{CEO}.

However, as was shown by *Havercamp* et al., there are always fixed frequencies f^X_{fix} that remains unaffected by any distortion X [114, 150].

$$f^X_{fix} = f_{CEO} + f_{rep} \frac{\delta f_{CEO}}{\delta X} \left(\frac{\delta f_{rep}}{\delta X} \right)^{-1} \tag{2.62}$$

where X could be any physical parameter of the cavity, e.g., its length or the

temperature of the laser crystal. The fixed point formalism is illustrated in Fig. 2.6, where two types of fluctuations are shown. It can be used as a base whose linear combinations describe general frequency fluctuations of the laser. A fluctuation of type a (Fig. 2.6, top) results from a fluctuation of the mean of the group and phase delay of the laser cavity, while their ratio is kept constant. For this type of fluctuation, the repetition rate and the carrier frequency fluctuate. The fixed point frequency coincides with the frequency origin. A type b fluctuation (Fig. 2.6, bottom) is induced by a fluctuating difference between the group and phase delay in the laser cavity, while the phase delay is kept constant. As result of this, the repetition frequency fluctuates, but the carrier frequency remains unaltered, which is, therefore, the fixed point frequency for fluctuations of type b [148].

Most environmental contributions to OFC dynamics, such as thermal or nonlinear changes of the intracavity refractive indices, have an f_{fix}^{env} located between zero frequency and the carrier frequency [150]. This means that they neither add a pure contribution to the group delay nor do they only affect the phase delay of the group. Cavity length fluctuations only affect the repetition rate f_{rep} of the laser but leave the per-round-trip phase shift $\Delta\phi_{CEO}$ between envelope and carrier unchanged (in first approximation).

Measuring the fixed frequency f_{fix} can help to pinpoint the source of dominant OFC dynamics.

2.6.3 Intensity-related spectral shift

The importance of pump-induced spectral shifts was recognized in very early work [105] and its importance has been noted for both Ti:Sa [151] and fiber-laser based OFCs [114]. The basic effect is quite simple: a shift in the spectrum causes a shift in the round trip time, $\omega_\Delta\beta_2$, due to the net cavity dispersion as in Eq. (2.79). In so much as ω_Δ and β_2 can be measured experimentally, the strength of this effect is easily calculated as in Eq. (2.80). However, given the apparent importance of this effect, it is worth considering what actually causes the pump-induced spectral shift.

The two effects of frequency-dependent loss and nonlinear frequency shifts can lead to a pump-induced frequency shift. In each case, a frequency-pulling effect is counteracted by the filtering effects of the gain profile. Fig. 2.7 shows schematically

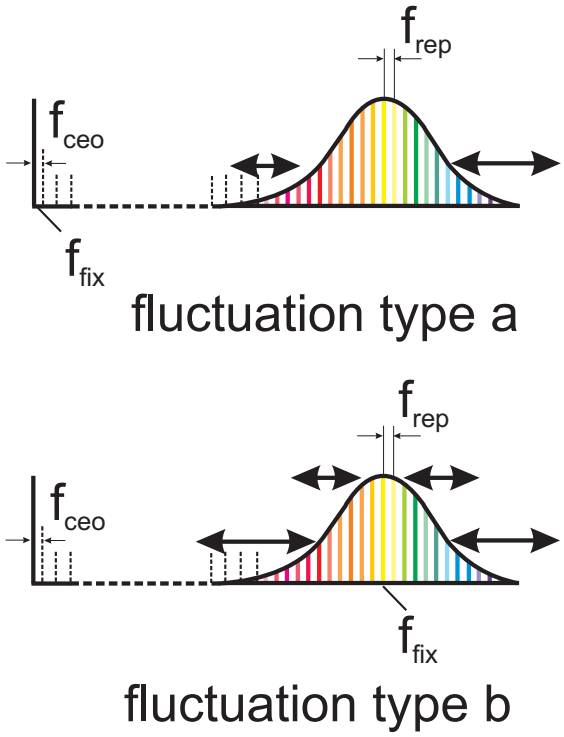

Figure 2.6: Fixed point model description for different types of fluctuations in the laser. Fluctuation type a (top) is caused by a fluctuating mean of the group and the phase delay with the ratio of the two held constant. Type b (bottom) is caused by a change of the difference between the group and the phase delay, while the phase delay is kept constant [114].

the competing effects. The nonlinear component to the frequency shift, $\omega_{\Delta,NL}$, arises primarily from the well-known Raman self-frequency shift, although self-steepening can also contribute for a chirped pulse. The linear component, $\omega_{\Delta,L}$ arises from a slope to the cavity loss, $l_\omega = dl/d\omega$. Mathematically, [92, 115]

$$\omega_{\Delta,NL} = \frac{-2A^2\delta}{5D_g(1+C^2)}(\tau_g + \mu\omega_0^{-1}C) \qquad \text{and} \qquad \omega_{\Delta,L} = -\frac{l_\omega}{2D_g} \tag{2.63}$$

where A is the pulse peak intensity, δ is the lumped nonlinearity for the laser, D_g is is the second derivative of the power-broadened gain, i.e. the curvature of the gain as a function of frequency, C is the pulse chirp, ω_0 is the pulse central

peak, μ is a minor numerical correction related to the modal shape.

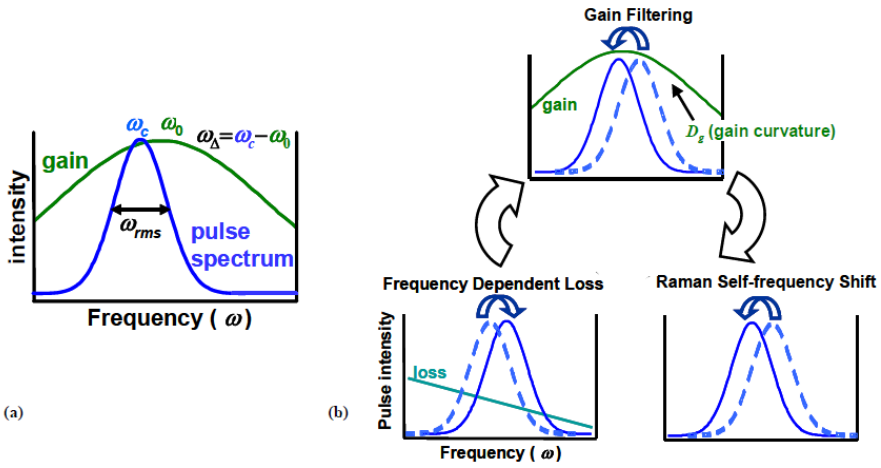

Figure 2.7: (a) Definition of frequency terms: ω_0 is the gain peak, ω_c is the pulse spectral peak, ω_{rms} is the pulse spectral width, and $\omega_\Delta = \omega_c - \omega_0$. (b) Schematic showing the spectral shift effects. The pulse can shift higher or lower in frequency if there is a frequency dependent loss. It will shift lower in frequency due to the Raman self-frequency shift. In the erbium-doped fiber, it will shift back toward the gain peak at ω_0 due to gain filtering [115].

2.6.4 Intensity-dependent f_{CEO} in octave-spanning Ti:Sa laser

Assume that the laser operates at carrier frequency ν_c, then the complex carrier wave of the pulse is given by [94]

$$e^{i2\pi\nu_c(t-z/v_p)}, \tag{2.64}$$

In the absence of nonlinearities v_p is simply the ratio between frequency and wavenumber due to the linear refractive index of the media in the cavity, i.e., $v_p = v_p(\nu_c) = 2\pi\nu_c/k(\nu_c)$. The envelope of a pulse that builds up in the cavity due to the mode-locking process will travel at the group velocity due to the presence of the linear media given by $v_g = v_g(\nu_c) = 2\pi[dk(\nu_c)/d\nu_c]^{-1}$. Therefore, after one round trip of the pulse over a distance $2L_{cav}$, which takes the time $T_R = 2L_{cav}/v_g$,

we obtain from Eq. (2.64) that the linear contribution to the $\Delta\phi_{CEO}$ caused by the difference between phase and group velocities is

$$\Delta\phi_{CEO} = 2\pi\nu_c \left(1 - \frac{v_g(\nu_c)}{v_p(\nu_c)}\right) T_R \tag{2.65}$$

and for the subsequent f_{CEO}

$$f_{CEO} = \nu_c \left(1 - \frac{v_g(\nu_c)}{v_p(\nu_c)}\right) \tag{2.66}$$

In a dispersive medium, v_g and v_p depends on the ν_c. Therefore, if the ν_c shifts as a function of the intracavity pulse energy, the linear f_{CEO} becomes energy and pump power dependent as found in [112].

In a mode-locked laser there are also nonlinear processes at work that may directly lead to an energy-depended f_{CEO}. There are many effects that may contribute to such a shift. Here we re-derive briefly the effects due to the intensity-dependent refractive index as discussed by *Haus* and *Ippen* [106] for the case of a laser with strong soliton-like pulse shaping which can be evaluated analytically using soliton perturbation theory. We then argue that the same analysis holds for the general case where steady-state pulse formation is different from conventional soliton pulse shaping.

Now we follow to the theoretical approach of *Matos* et al. [94]. We start from the description of a mode-locked laser by a master equation of the form

$$T_R \frac{\delta A}{\delta T} = D_{irrev} A + iD_2 \frac{\delta^2}{\delta t^2} A - i\sigma |A|^2 A \tag{2.67}$$

where we have already factored out the carrier wave [152]. Here, D_{irrev} is an operator that describes the irreversible dynamics occurring in a mode-locked laser such as gain, loss and saturable absorption. $A \equiv A(T,t)$ is the slowly varying field envelope whose shape is investigated on two time scales: first, the global time T which is coarse grained on the time scale of the round-trip time T_R, and second, the local time t which resolves the resulting pulse shape. $A(T,t)$ is normalized such that $|A(T,t)|^2$ is the instantaneous power and $\int dt |A(T,t)|^2$ the pulse energy at time T. $D_2 = (d^2k)/(d\nu_c^2) L_{cav}/8\pi^2$ is the GDD parameter for the cavity. The Kerr coefficient is $\sigma = (2\pi = \lambda_c) n_2 L = A_{eff}$, where l_c is the carrier wavelength, n_2 is the nonlinear index in cm/W, L is the path length per round trip through the

laser crystal, and A_{eff} is the effective mode cross-sectional area. Strictly speaking Eq. (2.67) only applies to a laser with small changes in pulse shape within one round trip. Obviously this is not the case for few-cycle laser pulses where the pulse formation is governed by dispersion-managed mode locking [110]. Nevertheless we want to understand this propagation equation as an effective equation of motion for the laser, where some of the parameters need to be determined self-consistently [152].

Let us assume that the laser operates in the negative GDD regime, where a conventional soliton-like pulse forms, and that it is stabilized by the effective saturable absorber action against the filtering effects. Then the steady-state pulse solution is close to a fundamental soliton, i.e., a symmetric sech-shaped pulse that acquires an energy-dependent nonlinear phase shift per round trip due to the nonlinear index [106]

$$A(T,t) = A_0 \mathrm{sech}(t/\tau) e^{-i\phi_s T/T_R} \tag{2.68}$$

The nonlinear phase shift per round trip is

$$\phi_s = \frac{1}{2}\sigma A_0^2 \tag{2.69}$$

A more careful treatment of the influence of the Kerr effect on the pulse propagation, especially for few-cycle pulses, needs to take the self-steepening of the pulse into account, i.e., the variation of the index during an optical cycle, by adding to the master equation the term [153].

$$L_{pert} = -\frac{\sigma}{\omega_c}\frac{\delta}{\delta t}(|A|^2 A) \tag{2.70}$$

We emphasize that this term is a consequence of the Kerr effect and is not related to soliton propagation. It can be viewed as a perturbation to the master Eq. (2.67). For pulses with τ much longer than an optical cycle, this self-steepening term is unimportant in pulse shaping, because it is on the order of $1 = \omega_c \tau \ll 1$. However, this term is always of importance when the phase shifts acquired by the pulse during propagation are considered. *Haus* and *Ippen* found, by using soliton perturbation theory based on the eigensolutions of the unperturbed linearized Schrödinger equation, analytic expressions for the changes in phase and group

velocity. Obviously, the nonlinear phase shift per round trip of the soliton adds an additional phase shift to the pulse in each round trip.

If the term in Eq. (2.70) is applied to a real and symmetric waveform, it generates an odd waveform.

An odd waveform added as a perturbation to the symmetric waveform of the steady-state pulse leads, to first order, to a temporal shift of the steady-state pulse. For a soliton-like steady-state solution this timing shift can be evaluated with soliton perturbation theory, i.e., using the basis functions of the linearized operator, and results in a timing shift [106, 154].

$$T_R \frac{\delta \Delta t(T)}{\delta T}\bigg|_{self-steep} = \Delta\left(\frac{1}{v_g}\right) = \frac{\sigma}{\omega_c} A_0^2 = \frac{2\phi_s}{\omega_c} \tag{2.71}$$

In total, the compound effect of self-phase modulation, self-steepening, and linear dispersion on the pulse results in a carrier-envelope frequency of

$$\begin{aligned} f_{CEO} &= \frac{f_{rep}}{2\pi}\Delta\phi_{CEO} \\ &= -f_{rep}\frac{\phi_s}{2\pi} + \nu_c \frac{\delta}{\delta T}\Delta t(T)_{self-steep} + \nu_c\left(1 - \frac{v_g(\nu_c)}{v_p(\nu_c)}\right) \\ &= -\frac{f_{rep}}{4\pi}\delta A_0^2 + 2\frac{f_{rep}}{4\pi}\delta A_0^2 + \nu_c\left(1 - \frac{v_g(\nu_c)}{v_p(\nu_c)}\right) \end{aligned} \tag{2.72}$$

As the above expression shows, the term arising from the group delay change due to self-steepening is twice as large and of opposite sign compared with the one due to self-phase modulation. In total we obtain

$$f_{CEO} = \frac{f_{rep}}{4\pi}\delta A_0^2 + \nu_c\left(1 - \frac{v_g(\nu_c)}{v_p(\nu_c)}\right) \tag{2.73}$$

Note that soliton perturbation theory was only used in this derivation for analytical evaluation of timing shifts. If the pulse shaping in the laser is not governed by conventional soliton formation but rather by dispersion-managed soliton dynamics [110] or a saturable absorber, the fundamental physics stays the same. If the steady-state solution has a real and symmetric component, the self-steepening term converts this component via the derivative into a real and odd term, which is to first order a timing shift in the autonomous dynamics of the free running mode-locked laser. Another mechanism that leads to a timing shift is, for example, the

action of a slow saturable absorber, which absorbs only the front of the pulse. So care needs to be taken to include all relevant effects when a given laser system is analyzed.

The intensity dependence of f_{CEO} in octave-spanning OFCs is a simple linear behavior which is universal, provided the correct pump power level is used to prevent the appearance of pulse instabilities such as cw breakthrough. The pulse energy in the octave-spanning regime is strongly clamped by the KLM action and the combination of SPM and bandwidth limitation, making the intensity-related carrier-envelope frequency shift much smaller than one would expect from the cw laser model.

2.6.5 Intensity-dependent f_{CEO} in Ti:Sa laser with spectrum broadening in PCF

Holman et al. shows that f_{CEO} and f_{rep} depend on the laser power and hence on pulse peak intensity I in Ti:Sa lasers with spectrum broadening in PCF, as [112]

$$\frac{df_{rep}}{dI} = \frac{1}{l_c}\frac{dv_g}{dI} \tag{2.74}$$

$$\frac{df_{CEO}}{dI} = \frac{1}{2\pi}\frac{\delta\omega_c}{\delta I}\left(1-\frac{v_g}{v_p}\right) + \frac{\omega_C}{2\pi}\frac{v_g}{v_p}\left(\frac{1}{v_p}\frac{dv_p}{dI} - \frac{1}{v_g}\frac{dv_g}{dI}\right) \tag{2.75}$$

where $\omega_c/\delta I$ is the intensity-related laser spectral shift (see Sect. 2.6.3). Denoting by $\bar{n}(\bar{n} = \bar{n}_0 + \bar{n}_2 I)$ the average refractive index in the laser cavity leads to $v_g = c/[\bar{n} + \omega_c(d\bar{n}/d\omega)_{\omega_c}]$ and $v_p = c/\bar{n}$, which lead to the following equations:

$$\frac{df_{rep}}{dI} = -\frac{1}{l_c}\frac{v_g^2}{c}\left[\bar{n}_2 + \omega_c\left(\frac{d\bar{n}_2}{d\omega}\right)_{\omega_c} + c\frac{\delta\omega_c}{\delta I}\frac{\delta}{\delta\omega_c}\left(\frac{1}{v_g}\right)\right] \tag{2.76}$$

$$\begin{aligned}\frac{df_{CEO}}{dI} = {} & \frac{\omega_c^2}{2\pi}\frac{v_g^2}{c^2}\left[\bar{n}_0\left(\frac{d\bar{n}_2}{d\omega}\right)_{\omega_c} - \bar{n}_2\left(\frac{d\bar{n}_0}{d\omega}\right)_{\omega_c}\right] \\ & + \frac{1}{2\pi}\frac{\delta\omega_c}{\delta I}\left[\left(1-\frac{v_g}{v_p}\right) + \frac{\omega_c v_g^2}{v_p}\frac{\delta}{\delta\omega_c}\left(\frac{1}{v_g}\right) - \frac{\omega_c v_g}{c}\frac{\delta\bar{n}}{\delta\omega_c}\right]\end{aligned} \tag{2.77}$$

All terms except $\delta\omega_c/\delta I$ and $\delta(1/v_g)/\delta\omega_c$ are constants. The last term in Eq. (2.76) and the second term in brackets in Eq. (2.77) reveal the dependence

of df_{rep}/dI and df_{CEO}/dI on the intensity-related spectral shift. Both equations are dominated by a term proportional to $\delta\omega_c/\delta I\delta(1/v_g)/\delta\omega_c$, explaining the near coincidence in the sign change of df_{rep}/dI and df_{CEO}/dI with that of $\delta\omega_c/\delta I$. By experimentally measuring df_{rep}/dI and df_{CEO}/dI it is possible to calculate the spectrally related shift of $1/v_g$ (i. e., $\delta(1/v_g)/\omega_c$.

2.6.6 Response of f_{CEO} to a pump-power change

The shift in f_{CEO} is complicated by the fact f_{CEO} is the product of ϕ_{CEO} and f_{rep}. In the work [115] for fiber laser was considered that a shift in envelope arrival time will shift both ϕ_{CEO} and directly shift f_{rep} by $\Delta f_{rep} = f_{rep} - 2\Delta T_{rep}$. A careful treatment yields the following expression for the change in the f_{CEO} offset versus pump power [115]

$$\frac{df_{CEO}}{dP} = \frac{\beta_0}{2\pi}\left(\frac{df_{rep}}{dP}\right) + \frac{f_{rep}}{2\pi}\left(\frac{d\phi_{spm}}{dP}\right) \tag{2.78}$$

where $\beta_0 = nL\omega_0/c$ is the lumped, average fiber propagation constant for the laser of length L and average index of refraction n. The first term accounts for shifts in the carrier envelope arrival time and the second accounts for shifts in the carrier phase from self-phase modulation. Eq. (2.78) predicts two important results (see Fig. 2.8). First, it predicts a linear relationship between df_{CEO}/dP and df_{rep}/dP with a slope of $\beta_0/(2\pi)$. Which is, in fact, the main term in Eq. (2.62) for the ν_{fix}^{pump}. Second, it predicts an intercept given by the pump-induced change to the SPM, or Kerr, phase shift.

2.6.7 Response of the repetition frequency to a pump-power change

In the SbSect. 2.6.6, we found that the pump-induced change in the offset frequency is typically dominated by the pump-induced change in the repetition frequency, df_{rep}/dP. The next question to address is what are the fundamental reasons for a pump-induced change in the repetition frequency?

There are a number of perturbations that affect the round-trip time around the cavity, T_{rep}, and therefore the repetition rate, f_{rep}. The perturbations considered here are: resonant gain contribution, spectral shifts, third-order dispersion, and

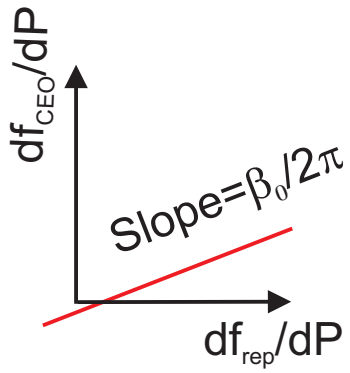

Figure 2.8: Linear relationship between df_{CEO}/dP and df_{rep}/dP with a slope of $\beta_0/(2\pi)$ [115].

self-steepening. If one includes these perturbations the total round trip time is given by [115]

$$T_r = \frac{1}{f_{rep}} = \beta_1 + \omega_\Delta \beta_2 + \frac{1}{2}\omega_{rms}^2 \beta_3 + \frac{g}{\Omega_g} + \frac{\mu A^2 \sigma}{\omega_0} \tag{2.79}$$

where $\beta_n = d^n\beta/d\omega^n|\omega_0$ are the frequency-derivatives of the lumped linear fiber propagation constant evaluated at the gain peak, ω_0. The first term is just the expected round-trip time for a group velocity of L/β_1. The second term is a correction due to spectral shifts c $\omega_\Delta = \omega_c - \omega_0$ of the carrier from ω_0. The third term is a correction due to third-order dispersion, where ω_{rms} is the root-mean-square pulse spectral width, and we assume $\omega_{rms} \gg \omega_\Delta$. The fourth term is the resonant contribution from the laser active medium gain assuming a Lorentzian gain shape with peak value g and bandwidth Ω_g. The final term is the nonlinear self-steepening contribution, where μ is a minor numerical correction related to the modal shape.

A calculation of df_{rep}/dP involves taking the derivative of each term on the right hand side of Eq. (2.79). The first term, β_1, vanishes since it is by definition the linear part of the propagation constant. The second term is proportional to the pump-induced spectral shift, $d\omega_\Delta/dP$, which can be measured experimentally. For the remaining terms, we relate the relevant derivatives (of ω_{rms}, g, and A_2) to the derivative of the pulse energy, dw/dP, and ultimately to the fractional change in the pump power in order to derive a more useful expression for df_{rep}/dP.

See [115]for details of this scaling, here we are interested in a final result:

$$\frac{df_{rep}}{dP} = -f_{rep}^2 \left\{ \overbrace{\beta_2 \frac{d\omega_\Delta}{dP}}^{SpectralShift} + \overbrace{\frac{\omega_{rms}^2 \beta_3}{2P}}^{TOD} + \overbrace{\frac{\nu^{LasMed}}{2P\nu\Omega_g}}^{Gain} + \overbrace{\frac{3\mu A^2 \sigma}{2P\omega_0}}^{SS} \right\} \tag{2.80}$$

The graphical representation with strengths of the various contributions for *fiber laser* are shown in Fig. 2.9. The sum of the effects yields the solid black line, to be compared to the experimental measurements (solid black squares) [115].

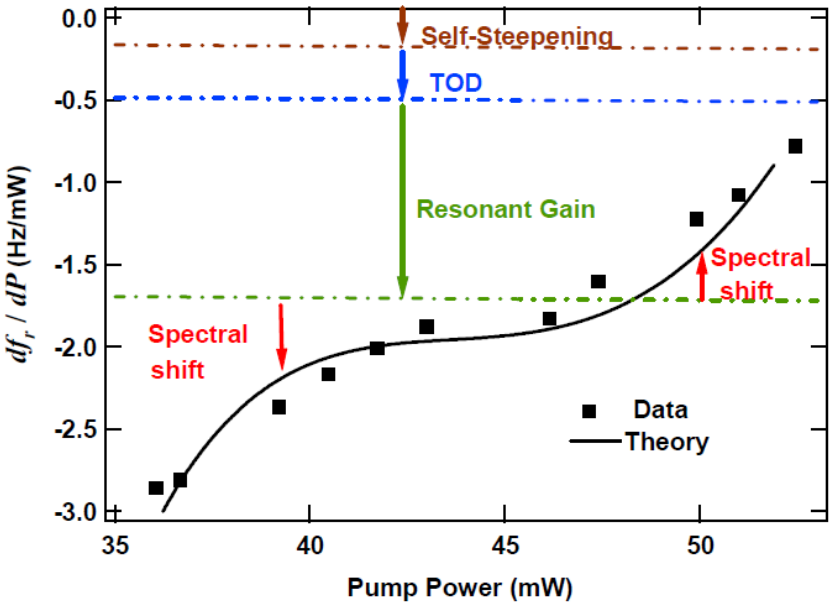

Figure 2.9: The measured df_{rep}/dP versus pump power measured by *Washburn* et al. [115]. The sum of the effects yields the solid black line, to be compared to the experimental measurements (solid black squares).

2.6.8 Measurement of the f_{CEO}

An early approach for measurement of f_{CEO} employed an interferometric method based on second-harmonic generation (SHG) cross-correlation between two subsequent laser pulses [105]. For vanishing $\Delta\phi_{CEO}$, the cross-correlation signal is

identical to the interferometric autocorrelation, with a symmetric fringe pattern. In all other cases, the fringe pattern appears shifted with the fringe maximum located at $\Delta\phi_{CEO}/\omega$ and the cross-correlation is asymmetric. Even though this measurement in the time domain works in principle [39], it is very susceptible to offset errors. Any offset between group and phase delay in the long arm of the cross-correlator will induce a measurement error in determining f_{CEO}. Therefore, phase-coherent methods are indispensable for precise control of the $\Delta\phi_{CEO}$ as was suggested in [37].

2.6.9 Amplitude-to-phase conversion effects

The key to understanding the mechanisms forming the f_{CEO} phase noise is Eq. (2.59). Any change of temperature, air pressure, or laser power may also affect $\Delta\phi_{CEO}$. For simplicity, assume that we have a laser cavity of length L filled with a material of index n. We can then rewrite the dependence of Eq. (2.59) on any laser or environmental parameter X as [105, 151, 155]:

$$\frac{\delta}{\delta X}\Delta\phi_{CEO} = 2\omega_c\frac{\delta\omega_c}{\delta X}\frac{\delta n}{\delta\omega}L + \omega_c^2\frac{\delta n}{\delta\omega}\frac{\delta L}{\delta X} + \omega_c^2\frac{\delta^2 n}{\delta\omega\delta X}L \tag{2.81}$$

Amplitude-to-phase conversion (APC) is a special case of Eq. (2.81). The case where X is the intensity deserves special attention, as the resulting fluctuations of $\Delta\phi_{CEO}$ can be arbitrarily fast when electronic nonlinearities such as the all-optical Kerr effect are mediating between amplitude fluctuations and CEO phase noise. APC effects are mainly taking place in the laser crystal, as this is the position of highest intracavity intensities.

Spectral shifting of the laser spectrum has been proposed as the first mechanism giving rise to APC effects [105]. The carrier frequency ω_c shifts with pump power or intracavity intensity, an effect that strongly depends on the operating conditions of the laser. Generally, both effects seem to be weaker when the laser bandwidth is wider. In a recent publication, spectral shifting was observed for a 750 MHz repetition-rate laser below 50 nm mode-locked bandwidth, whereas it did not appear to play a role in a 100 MHz repetition-rate laser with its stronger mode locking and higher pulse energy [112]. APC coefficients $\partial f/\partial I$ on the order of 10^{-7} HzW/m^2 were observed when spectral shifting dominates the APC, resulting in the prevalent contribution to $\Delta\phi_{CEO}$ noise. In contrast, the APC coefficient drops

to a few 10^{-9} HzW/m^2 in the absence of spectral shifting [108, 112, 155].

A second contribution to $\Delta\phi_{CEO}$ noise arises from geometrical changes of the laser cavity affecting the total cavity length L. This contribution is typically negligible in prismless cavities but can play a role in cavities that use intracavity prism sequences for dispersion compensation [40], [108]. One potential mechanism behind such laser dynamics is beam-pointing variations inside the laser cavity together with the directional sensitivity of the dispersion of a prism compressor [108, 156, 157]. If the beam direction inside the prism sequence changes, this will also affect the net first-order dispersion of the cavity via the second term in Eq. (2.81). Beam-pointing variations can be induced by changes of the refractive index of the laser crystal. If the index of refraction of the laser crystal changes, Snell's law demands a change of angles inside and outside the laser crystal [108]. Beam-pointing effects are held responsible for an approximately tenfold increase of $\Delta\phi_{CEO}$ noise of prism laser cavities as compared to prismless variants.

The third term in Eq. (2.81) contains contributions to $\Delta\phi_{CEO}$ noise via intensity-induced changes of the refractive index [106, 153, 158]. Nonlinear fraction is well known as the all-optical Kerr effect [153], but according to Eq. (2.81), only the dispersion of the Kerr effect affects changes of the $\Delta\phi_{CEO}$. The issue of dispersion of the Kerr effect has been addressed by [159, 160]. According to *Sheik-Bahae* et al. [159], the main contribution to the first-order dispersion of a dielectric medium well below half the band edge stems from a Kramers-Kronig term induced by two-photon absorption. As per their example, for sapphire at 800 nm, one calculates $\partial^2 n/\partial\omega\partial I \approx 10^{-36}$ s m^2/W rad. Inserting values for typical Ti:Sa laser cavities [84], one computes a theoretical estimate of $\partial f/\partial I_0 = 5 \times 10^{-9}$ HzW/m^2, which agrees well with the lowest experimentally observed values of $\partial f/\partial I_0$. Again, these low APC coefficients can only be reached in the absence of geometrical effects and spectral shifting.

From the experimental observations, some guidelines can be given on how to keep APC effects to a minimum. The first recommendation is to use a prismless cavity. In prismless cavities, beam pointing does not translate into CEO phase noise [108]. Spectral shifting is the other APC effect that can be avoided by suitable design of the laser. For a stable position of the laser spectrum, a broad mode-locked bandwidth of more than 50 nanometers and a high pulse energy appear to be favorable conditions [112]. If geometric effects and spectral shifting

can be avoided, the APC effects are restricted to nonlinear refractive mechanisms, both Kerr-type and an additional thermally induced mechanism at low Fourier frequencies. Values on the order of $\partial f/\partial I_0 = 10^{-8}$ HzW/m^2 or less are indicative of a dominance of nonlinear refraction in the APC dynamics.

2.6.10 Phase-locked OFC

One might expect that various noise processes would disrupt the pulse train of a mode-locked laser, effectively blurring out any OFC structure. Fortunately, it turns out that this noise simply causes the OFC to stretch or shift. This motion can be eliminated by phase-locking (or 'monitoring') the OFC with respect to an underlying frequency reference [44, 81, 100, 104, 161–163] to stabilize f_{rep}, which controls the tooth spacing, and f_{CEO}, which sets the overall frequency shift of the OFC. The teeth of the resulting OFC are phase-coherent with each other as well as with the underlying frequency reference.

f_{CEO} stabilization

To stabilize the offset frequency it is crucial to generate a full optical octave. However, the typical spectral output generated by Ti:Sa lasers spans only several tens of nm. Propagation through optical fibers is commonly used to broaden the spectrum of mode-locked lasers via the nonlinear process of self-phase modulation. Nevertheless, chromatic dispersion in the fiber rapidly stretches the pulse duration, thus lowering the peak power and limiting the width of generated spectrum. A real breakthrough has been represented by the advent of air-silica microstructure fibers having zero group dispersion at 780 nm [38,164]. By coupling the Ti:Sa laser output into such a fiber, the sustained high intensity (hundreds of GW cm^{-2}) generates a stable, single-mode, phase-coherent continuum that stretches from $\sim$ 520 to $\sim$ 1130 nm. Through four-wave mixing processes, the original spectral OFC in the mode-locked pulse is transferred to the generated continuum. Once a full octave is obtained, f_{CEO} can be detected by the self-referencing technique (see Sect. 2.3). f_{CEO} signal is fed into suitable servo electronics which acts on the cavity end mirror.

The only missing link to stabilization of the f_{CEO} is now a mechanism for external control of the f_{CEO}. Such a mechanism allows closing the servo loop,

forcing the f_{CEO} into a lock with a RF-reference oscillator. Ideally, a control mechanism should only act on the f_{CEO} and leave other cavity parameters unchanged (orthogonality). If we leave this concern aside, all mechanisms causing an amplitude-to-phase conversion (APC) are suited, in principle, for control of the f_{CEO}. A servo bandwidth of more than 10 kHz is needed, which rules out many slow mechanisms. Choice of the control mechanism is therefore a trade-off between orthogonality and bandwidth.

In lasers with intracavity prism sequences, an elegant way of controlling the f_{CEO} of a laser without affecting other laser parameters is offered. Tilting the end mirror after the prism sequence affects only the difference between the group and phase delay in the cavity but leaves other laser parameters widely unchanged [30, 165]. The tilt of the end mirror has to be restricted to small excursions compared to the angular aperture of the beam at the end mirror. Only then one can be sure that the intracavity power is not also affected by the mirror tilt. Mirror excursion in the microradian range is sufficient to control the f_{CEO} within one spectral range. This makes mirror tilting the method of choice for cavities with prisms. However, it is typically very difficult to reach a servo bandwidth of more than 1 kHz with mirror tilting because of mirror inertia. Reaching sufficient bandwidth requires an optimized setup of the tilt actuator. Bandwidths up to 25 kHz have been demonstrated using a mirror of low mass directly mounted on a split piezoelectric transducer (PZT) actuator [107].

Mirror tilting is not an option when a prismless setup is used. Then the method of choice is modulation of the pump power either with an acoustooptic modulator [155] or with an electro-optic device [166]. As the required pump-power modulation is on the order of 10^{-3}, it is typically very easy to reach bandwidths of several tens to hundreds of kHz. Pump-power modulation relies on the APC mechanisms discussed in the previous section and is currently the most widespread mechanism for f_{CEO} control.

Repetition rate frequency stabilization

Repetition rate control is easily obtained by adjusting the cavity length using a piezoelectric transducer (PZT) to translate one of the end mirrors. In practice, PZT stacks can twist as they expand or contract, thereby requiring a more complex

arrangement. Also, temperature stabilization of the laser base plate is usually accomplished; this reduces cavity length drifts, thus allowing an ordinary PZT to achieve a sufficient range. Also f_{rep} control by the pump-power modulation were recently suggested and tested [167, 168].

Chapter 3

Apparatus

In first Sect. 3.1 of this chapter the key questions of the fs Ti:Sa laser development are presented: the active medium characteristics in SbSect. 3.1.2, characteristics of three different types of the pump lasers (Millennia Xs, Verdi V5, Verdi G7) in SbSect. 3.1.3, the Ti:Sa cavity design in SbSect. 3.1.4, elements of stabilization of both OFC's degrees of freedom in SbSect. 3.1.5, PCF properties and input beam alignment in SbSect. 3.1.7, implementation of the f-2f interferometer in SbSec. 3.1.8.

Separately characteristics of the OFC operated in quasi octave-spanning regime are presented in in Sect. 3.2).

The absolute frequency characteristics of the locked OFC clearly depend on the reference. In our case, the reference is the clock laser ([169, 170]), which was involved in day-by-day operation with OFC and its main characteristics are presented in Sect. 3.3.

3.1 Self-referenced home-build fs Ti:Sa laser

Nowadays many OFCs with different characteristics are commercially available. For experiments that need to use an OFC as a black box, the choice of a proper commercial OFC is often the best solution. While these lasers can be perfectly realized, for metrological applications the main task remains the phase stabilization of OFC. For this a proper realization of a phase-lock loop (PLL) is demanded with good understanding of nature of the OFC frequency noise. For some experiments

in which the best stability is required, this translates in modifications needed in the laser optical cavity or stabilization PLL circuits. For simple cases, these modifications may concern PZT adding/modification for building proper repetition rate frequency f_{rep} control, dispersion managing for stabilizing f_{CEO} and improving noise characteristics. Modifications finally can change a lot an initial design of a laser. For this reason it also suitable to build up OFC in laboratory from scratch in order to study properties of the OFC. This will demand initially more time than to buy a commercial OFC. However, it can give a profit in time at the stage of OFC stabilization.

3.1.1 Clean room environment

The clock laser and fs Ti:Sa laser are placed in a class 1000 clean room. Also the temperature is stabilized at $21 \pm 1°C$ and remains in this region if the temperature outside of laboratory is not dramatically changing. These conditions play a role in increasing the passive stability of Ti:Sa laser fs regimes up to weeks without need of cleaning the optics of the Ti:Sa laser, which is, naturally, very sensitive to dust.

The optical systems are partially insulated from seismic, acoustic and sub-acoustic disturbances. The optical table is supported by four pneumatic insulating legs. This system decouples floor seismic motions from the laser system, providing a -40 dB/decade vibration damping up to 30 Hz. A wooden panel above the table and a heavy-rubber curtain surrounding it block the direct clean room laminar air-flow and attenuate the acoustic noise from the rest of the laboratory [169].

3.1.2 Active medium: Titanium sapphire

One of the first questions in the project of building a fs laser is the choice of the active medium. Depending on the task, the choice can be among laser based on bulk crystals, fiber lasers, dye lasers or semiconductor lasers. Recently, fiber lasers have been studied in details in many scientific groups. This is due to the fact that these lasers are compact and do not need frequent alignments and are cheap when compared to bulk crystal lasers. The cost of bulk lasers is typically higher compared with fiber lasers due to the high price for pump lasers. However bulk crystal Ti:Sa lasers still remain a good choice due to their very large gain bandwidth. This feature allows to achieve very short pulses and a better S/N

ratio for beat notes when compared to OFCs based on other active media. These convert into the better ability to measure precisely an optical frequency.

The active medium used in the laser is a Titanium-ion doped sapphire crystal (Ti^{3+}:Al_2O_3). This is a vibronic laser medium, as there is strong coupling between the vibrational energy levels and the electronic energy levels of the Ti^{3+} active ions. The vibronic nature of Ti^{3+}:Al_2O_3 leads to broad absorption and emission spectra.

To date, Ti^{3+}:Al_2O_3 is the most common and commercially available tunable solid-state laser. Nowadays, it can be pumped with frequency-doubled Nd lasers at wavelengths around 532 nm, thus efficient all-solid state laser operation is possible. Formerly, Ar^+-ion laser pumping was applied. In commercial systems, overall efficiencies as high as 30% are obtained.

Besides the broad tuning capability of the Ti:Sa laser, its ability for ultrashort-pulse generation and amplification is especially exploited. In mode-locked operation, pulses as short as 5 fs [147, 171–174] and octave-spanning spectra (e.g., 600 nm to 1200 nm [147]) have been obtained.

The electronic structure of the Ti^{3+} ion is a close shell plus a single 3d electron. The free-space, fivefold-degenerate (neglecting spin) d-electron levels are split by the crystal field of the host. The site for the Ti^{3+} ion has trigonal symmetry in the host Al_2O_3; the crystal field can be viewed as sum of cubic- and trigonal-symmetry components. The cubic field dominates and splits the Ti^{3+} energy level into a triply degenerate $^2T_2$ ground state and a doubly degenerate ^2E excited state.

The absorption band centered at 490 nm makes it suitable for variety of laser pump sources - argon ion, frequency doubled Nd:YAG and YLF, copper vapor lasers. Given the low absorption cross-section and (compared to dye laser materials) the relatively low gain, a long gain medium is required to ensure efficient pumping and overall gain. As a result, the crystal must be pumped collinearly to obtain the best overlap between pump and resonator mode. An anti-reflection coated lens is used for focusing the pump beam in the Ti:Sa crystal. The polarization of the pump beam is rotated by a phase plate by $\pi/2$. The polarization of the laser mode is parallel to the optical table and governed by the lossless propagation through the surfaces at the Brewster angle of the crystal and the prisms. Moreover, the Ti:Sa rod may act as a birefringent filter in the cavity and thus works as a mode selector. Only the modes that have the correct polarization ori-

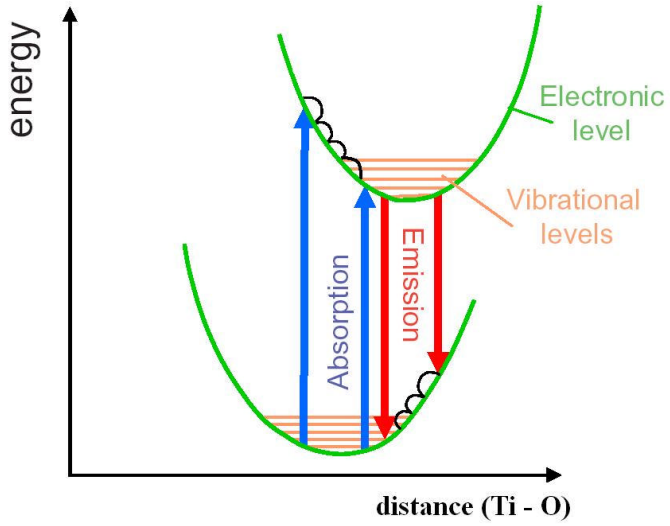

Figure 3.1: The energy levels diagram for Ti:Sa.

entation will propagate without any losses. Setting of the c-axis of the sapphire crystal parallel to the polarization direction of the circulating radiation, results in the lossless propagation over the whole accessible gain bandwidth. Therefore careful alignment of the crystal axis is crucial to sustain the broadband mode-locked operation of the laser.

The Sellmeir equation Eq. (2.36) for sapphire is

$$n^2_{Sa}(\lambda) = 1 + \frac{1,4313493 \times \lambda^2}{\lambda^2 - 0,0052799261} + \frac{0,65054713 \times \lambda^2}{\lambda^2 - 0,0142382647} + \frac{5,3414021 \times \lambda^2}{\lambda^2 - 325,017834} \quad (3.1)$$

where λ in μm. The corresponding graph is plotted in Fig. 3.2a. From it we can find $n(\lambda = 800\ \mu\text{m}) = 1.76$. By using the Eq. (3.1) and Eq. (2.41) the GDD of the sapphire rod is calculated and plotted in Fig. 3.2b.

3.1.3 Pump lasers

A Ti:Sa crystal typically is pumped by a green light from either an Ar^+-ion laser or a diode-pumped solid-state (DPSS) laser, which provides far superior performance in terms of laser stability and noise. Nowadays, two types of a DPSS lasers are widely used to pump fs Ti:Sa lasers for metrological applications: multi-mode

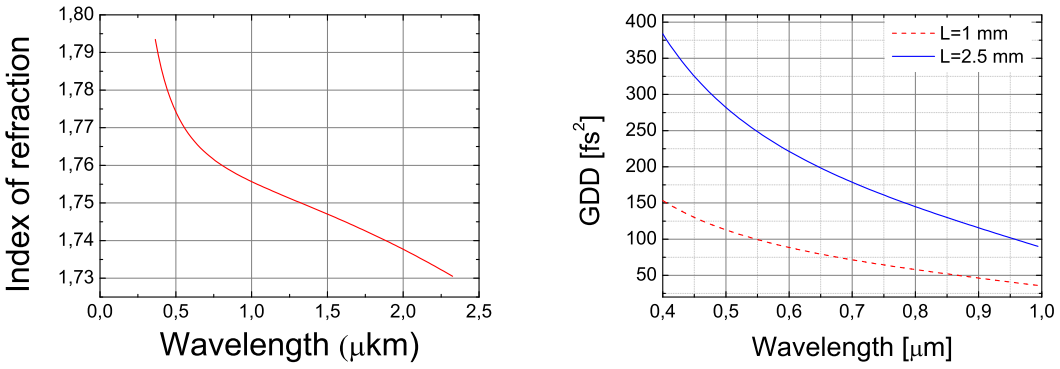

(a) (b)

Figure 3.2: (a) Index of refraction for Ti:Sa plotted for Sellmeir's equation. (b) GDD of a sapphire rod for the beam path in a crystal L=1 mm (red dashed line) and L=2.5 mm (blue solid line).

lasers (mml) and single-mode lasers (sml). The sml has an advantage versus mml due to his lower amplitude noise at higher frequencies. The properties of these pump lasers largely affects the properties of the Ti:Sa laser.

In our experiments we used both mlm (Millennia Xs Spectra-Physic and Verdi G7 Coherent) and slm (Verdi V5 Coherent) pump lasers.

Millennia Xs The Millennia Xs is an all solid-state, high power, visible cw laser that produces more than 10 W of green light at 532 nm. The Millennia Xs has a $1/e^2$ beam diameter of 2.3 mm $\pm 10\%$, beam pointing stability $< 5\mu$rad/ °C and relative amplitude noise $< 0.05\%$ rms.

Most of the results in this thesis have been obtained with this laser.

Verdi V5 The Verdi V5 from Coherent is a pump laser of the sml family. It can give more than 5 W output power, has a $1/e^2$ beam diameter of 2.25 mm $\pm 10\%$, beam pointing stability $< 2\mu$rad/ °C and relative amplitude noise $< 0.02\%$ rms.

We tested two versions of Verdi V5. When it is necessary to distinguish these two lasers, we will call the first one "Verdi V5 old".

Verdi G7 The Verdi G7 532 nm mml high power laser. It is based on optically pumped semiconductor laser technology where the rod-based gain medium

is replaced with a robust and versatile semiconductor chip. There are two advantages of this laser comparing with Verdi V series: no thermal lensing issues (TEM_{00} mode has better shape) and no "green" problem due to the very short (nanosecond) upper state lifetime. It can give more than 7 W output power, has a $1/e^2$ beam diameter of 2.25 mm $\pm 10\%$, beam pointing stability $< 2\mu$rad/ °C and relative amplitude noise $< 0.02\%$ rms.

We tested the OFC performance in QOS regime pumped by the Verdi G7 demo version.

Amplitude noise of pump lasers

First of all, we measured the amplitude noise of the all our pump lasers: the Verdi V5, Verdi G7 and Millennia Xs (Fig. 3.3). Verdi G7 has relative intensity noise (RIN) from low frequencies up to the $\sim$ 30 kHz comparable with Millennia Xs. At about 45 kHz Verdi G7 RIN has a bump at 40 kHz and at higher frequencies it goes down. So, in the important frequency region (for f_{CEO} phase stability) from 40-60 kHz (typical bandwidth of servo loop) up to the $\sim$ 300 kHz (most of the amplitude noise higher than 300 kHz will be effectively filtered out by the laser crystal itself due to the the 3.2 μs lifetime of Ti:Sa [109]) the Verdi G7 has lower RIN comparing with Millennia Xs RIN.

Comparing with Verdi V5 RIN, Verdi G7 RIN is one order higher from 100 Hz up to the $\sim$ 65 kHz. At $\sim$ 65 kHz and at 100 kHz Verdi V5 RIN has very high peaks, that can not be compensated by the servo-stabilization loop. The Verdi G7 amplitude noise at higher frequencies can be seen from phase noise of f_{CEO} signal (Fig. 3.3b. It is visible the bump at $\sim$ 45 kHz from Verdi G7 amplitude noise. In the frequency region 100-200 kHz the phase noise is going down, probably reaching the phase noise level of Verdi V5, and it has small peak at $\sim$ 265 kHz.

3.1.4 Femtosecond cavity design

General schemes

The second step of fs laser building is to chose of the region for a f_{rep}. Once it is chosen, it is necessary to choose between several possible designs for cavity. Basically, there are two commonly used linear cavities for Ti:Sa oscillator as de-

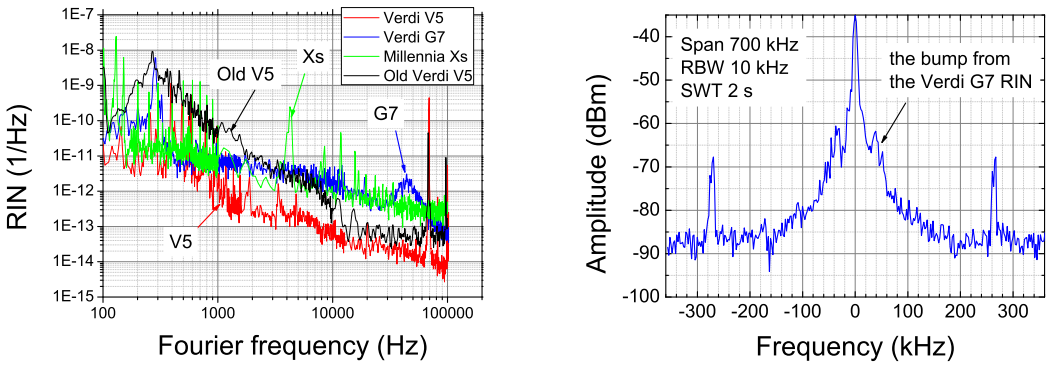

(a) (b)

Figure 3.3: (a) The RIN of all pump lasers used to pump the OFC. (b) Free-running f_{CEO} of the OFC pumped by Verdi G7.

picted in Fig. 3.4: an X or Z configuration. The folded cavity is suitable to obtain good mode matching with pump and to provide tight focusing in the mirror [175]. Beside it can control the astigmatism produce from laser cavity by adjusting the angle of the arm. Both types work equally well and usually selected based on considerations of available space in setting up the cavity [176].

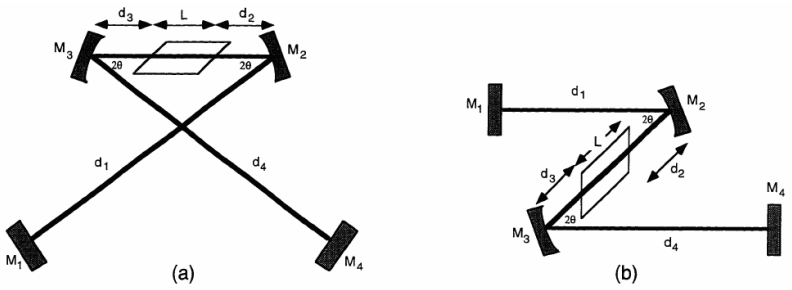

Figure 3.4: Commonly used cavity for Ti:Sa laser: X- and Z-configurations.

In Fig. 3.5 presented schematics of our X folded Ti:Sa cavity, where all possible plane mirrors between mirror M_1 and M_{4out} is neglected, because they don't have an impact on next calculations here we used ABCD-matrix's methods.

Several considerations must be taken into account when a fs cavity is designed. First is the cavity astigmatism.

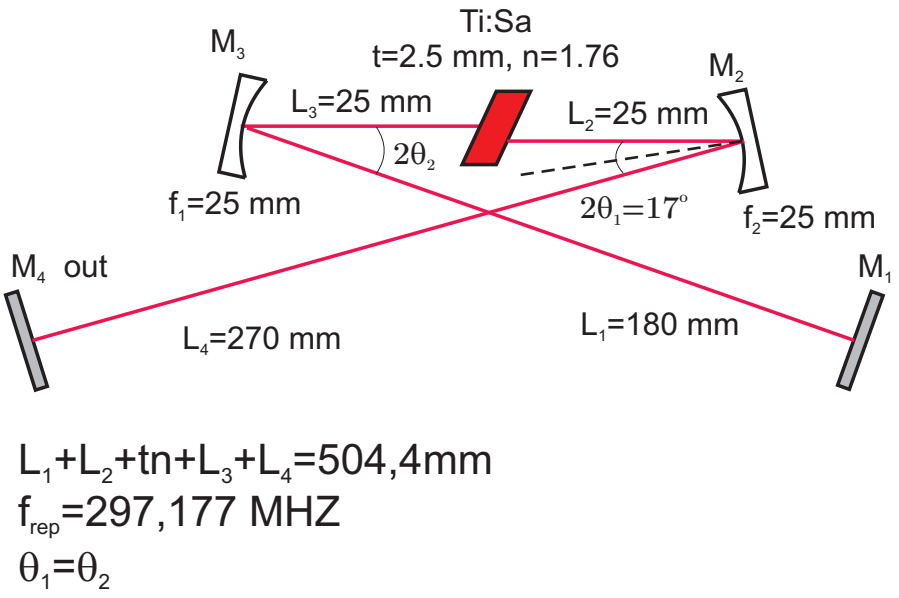

Figure 3.5: Schematics of our X folded Ti:Sa cavity.

Astigmatism compensation

The Ti:Sa crystal as an active medium, normally is cut at Brewster angle. The presence of the astigmatism in the cavity lead to a beam waist size which is different in the sagittal (perpendicular to the plane of incident) and tangential (parallel to the plane of incident) plane [177]. Astigmatism needs to be reduced because it can cause unstable mode-locking [178] and also reduced output power. For real X folded cavity, astigmatism cannot be completely compensated but minimized by titling opportunely the folding mirrors. For the curved mirrors, astigmatism comes from the asymmetry of the oblique incidence. The proper angle θ in Fig. 3.5 must be chosen to compensate the effects of each other.

In the sagittal and the tangential plane, according to [179], the Guassian beam is therefore reflected by two different effective focal lengths, related to the normal incidence focal length of the curved mirror $f = R/2$

$$f_x = \frac{f}{cos\theta} \tag{3.2}$$

$$f_y = f cos\theta \tag{3.3}$$

Another source of astigmatism is the Brewster angle cut Ti:Sa crystal. The effective length l_x and l_y the beams have to travel in the crystal [180]:

$$l_x = \frac{t\sqrt{n^2+1}}{n^2} \tag{3.4}$$

$$l_y = \frac{t\sqrt{n^2+1}}{n^4} \tag{3.5}$$

where t is the thickness of the Ti:Sa crystal, and n is the refractive index of it.

Knowing the two astigmatic elements, we compensate the astigmatism of the cavity and aim for maximum overlap of the stability region of x and y direction. To do this, consider the distance d_f between the curved mirror, for the x and y beam dimensions,

$$d_{f_x} = f_{1x} + f_{2x} + \delta_x = l_{air} + l_x \tag{3.6}$$

$$d_{f_y} = f_{1y} + f_{2y} + \delta_y = l_{air} + l_y \tag{3.7}$$

For the x and y direction, l_{air} is the same. Thus,

$$\delta_x - \delta_y = l_x - l_y - (f_{1x} - f_{1y}) - (f_{2x} - f_{2y}) = 0 \tag{3.8}$$

With this condition, the stability parameters in x and y direction are equal, and the The optimal fold angle for the cavity to reduce a crystal astigmatism can be calculated using the following equation

$$\frac{t(n^2-1)\sqrt{n^2+1}}{n^4} = f_1 \sin\theta_1 \tan\theta_1 + f_2 \sin\theta_2 \tan\theta_2 \tag{3.9}$$

for $f_1 = f_2 = f$, $\theta_1 = \theta_2 = \theta$, t is 2.5 mm, n is 1.76, $f = 50$ mm we calculate θ that is equal to $\sim 8.5°$.

Stability regions

The initial step to build a fs laser is to build a cw operating laser. For this a cavity should satisfy the stability rules.

With L_1, L_2, L_3, L_4 defined in Fig. 3.5 and labeling the distance between the curved mirrors: $d_f = f_1 + f_2 + t$, our cavity with the Ti:Sa crystal give us a transmission matrix as follow:

$$\begin{aligned} T =& M1 \times L1 \times M2 \times L2 \times \text{TiSa} \times L3 \times M3 \times L4 \times M4(\text{out}) \\ & \times L4 \times M3 \times L3 \times \text{TiSa} \times L2 \times M2 \times L1 \\ & = L1 \times M2 \times L2 \times \text{TiSa} \times L3 \times M3 \times L4 \\ & \times L4 \times M3 \times L3 \times \text{TiSa} \times L2 \times M2 \times L1 = \begin{pmatrix} A & B \\ C & D \end{pmatrix} \end{aligned} \tag{3.10}$$

where M_k is the matrix for mirror number k, L_k is the matrix for distance number k for elements in Fig. 3.5. Note here that matrices of Ti:Sa crystal for tangential and sagittal planes and the matrix of concave mirrors are not equal. This results in two different ABCD-matrix for tangential (T) and sagittal (S) planes.

Suppose that we want to analyze a region of the cavity stability when we are changing some distance in it, for example, distance L_2 between curved mirror M_2 and Ti:Sa crystal. For this we can use the stability condition for a cavity [74],

$$-1 \leq \frac{A+D}{2} \leq 1 \tag{3.11}$$

or in the form

$$0 < 1 - \left(\frac{A+D}{2}\right)^2 \leq 1 \tag{3.12}$$

The graph for the distance L_2 in the range where Eq. (3.12) is true and the cavity is stable (we put $f_1 = f_2 = f = 25$, $L_1 = 180$, $L_3 = 25$, $L_4 = 270$) is presented in Fig. 3.6. The green line is for tangential plane, red one is for sagittal. This distance will be changed when we will search a fs regime of our laser. Also useful to know the region for distance L_1 or L_4 in order to fix desired f_{rep}.

Dispersion compensation

For a fs laser the management of the cavity dispersion is of great importance. Without dispersion compensation, a longer wavelength component of the pulse

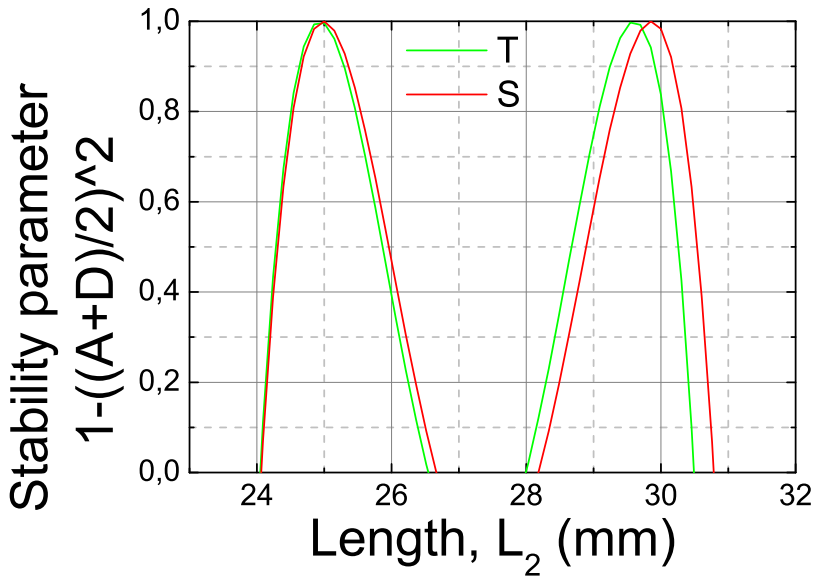

Figure 3.6: Regions for distance L_2 between mirror M_2 and Ti:Sa crystal when the cavity is stable.

propagate faster than shorter wavelength component, leading to pulse stretching. In a mode-locked laser for fs pulse generation, the uncompensated chromatic dispersion is not desirable, because to broaden and chirp the generated pulses, making the femtosecond pulse generation impossible.

A way to compensate the dispersion is to insert in the cavity a prism pairs [156]. Another solution is to use Gires-Tournois interferometer mirrors (GTI) [127] or chirped mirrors (see SbSect. 2.1.3).

Two different types of Ti:Sa cavities has been tested. In the first case we used Layertec GTI mirror with GDD -550±50 fs^2 in 790-815 nm optical region. The Ti:Sa crystal introduces a GDD of ≈ 145 fs^2 into our cavity (see Fig. fig:SapphireGDD). The air contribution is less than 10 fs^2 and there is some small contributions (less than 20 fs^2 for each mirror and specially for $\lambda = 800$ nm close to 0) from optics which laser beam passes in cavity. Thereby, total cavity GDD is about -400 fs^2 for $\lambda = 800$ nm in this case.

In second case we test a chirped pair mirrors 101410 from Layertec with a mean of ≈ -70 fs^2/reflection and Naneo Chord GDD mirror with a GDD ≈ -50 fs^2.

These resulting in a net GDD of $\approx -175\text{fs}^2$ per cavity round trip.

Pulse duration

The pulse duration of the fs pulses could be estimated through the pulse frequency spectrum. The center wavelength λ and the bandwidth $\Delta\lambda$ of the spectrum at full wave half maximum (FWHM) are the important parameters. These parameters have relationship with pulse frequency Δf which given as [181]

$$\Delta f = \frac{c}{\lambda^2}\Delta\lambda \tag{3.13}$$

For the cavity version with the GTI a typical pulse bandwidth is $\sim$ 11.5 nm, and for the chirped mirrors is $\sim$ 30 nm (Fig. 3.7). Note, that for the the fs cavity configuration with chirped mirrors it is also possible to generated very broad optput spectrum (more than 150 nm). The results for this case are presented in Sect. 3.2.

The minimum possible pulse duration of Ti:Sa laser can be estimated from Eq. 2.27, where we suppose that the femtosecond pulse is in the formation of hyperbolic secant pulse shape and $K = 0.315$ [78, 182]. Thus $\Delta t_1 \approx 58.4$ fs and $\Delta t_2 \approx 18$ fs.

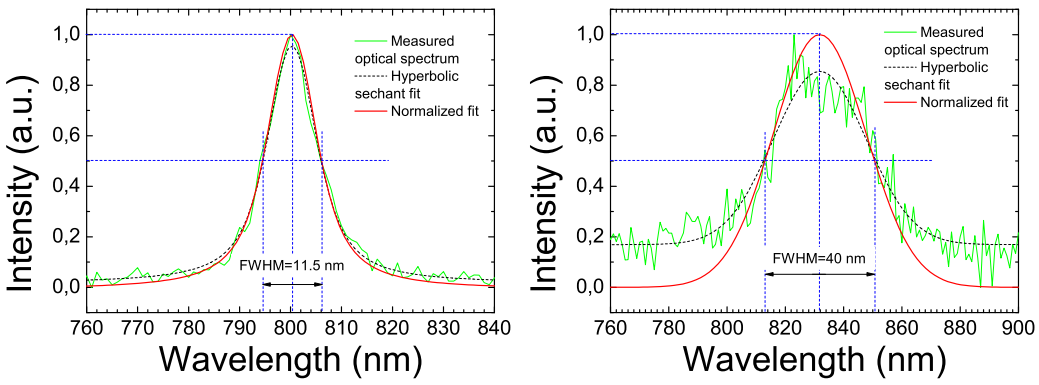

Figure 3.7: Emission optical spectrum of Ti:Sa laser in fs regime with total cavity dispersion $\sim -400\text{fs}^2$ (left) and $\sim -175\text{fs}^2$.

3.1.5 Elements for OFC stabilization

Passive stabilization

The performance of locked OFC has a direct link with the conditions of free-running OFC (see next chapter). Thus the improvement of the passive stability of a OFC is the first important step for frequency stabilization of its spectrum.

In order to increase the passive stability of the Ti:Sa cavity we have reduced the height of the beam with respect to the optical table at only 38 mm. The Ti:Sa cavity and all the optical components were isolated from external environmental perturbations. All the cavity optical path are surrounded by 20 mm thick Plexiglas boxes. We have reduced the thermal coupling between high power pump laser (Millennia Xs) and the Ti:Sa cavity by isolating the pump laser head from the main breadboard through a 2.5 cm thick Plexiglas slab. Note that Verdi V5 does not need to be isolated because has his own temperature stabilized support for the laser head.

The overall setup (pump, Ti:Sa cavity, f-$2f$ interferometer and schemes for beatnotes with 689 and 698 nm lasers) is mounted on an optical breadboard (90 cm $\times$90 cm) that is isolated from ground vibrations by using laminar flow damping legs.

All these tricks, together with the good stability of the temperature in the room (± 1°C) help to maintain a robust alignment of the optical path in long term measurements. In this condition, due to a residual change in temperature of the room we observe a maximum drift in the f_{rep} of the order of 20 mHz/s.

Active stabilization

As was noted before, a OFC has two degrees of freedom: f_{rep} and f_{CEO}, that should be stabilized to make precision frequency measurements. The stabilizations have been done by using PLLs, which are consists on an electronics part and electro-opto-mechanical actuators for control OFC parameters. In this section we describe the actuators.

f_{rep} stabilization The f_{rep} of a OFC is directly connected with the length of the cavity: $f_{rep} = c/2L$, where c is the speed of light and L is the cavity length. For this reason the cavity length change is used to control this frequency. The use

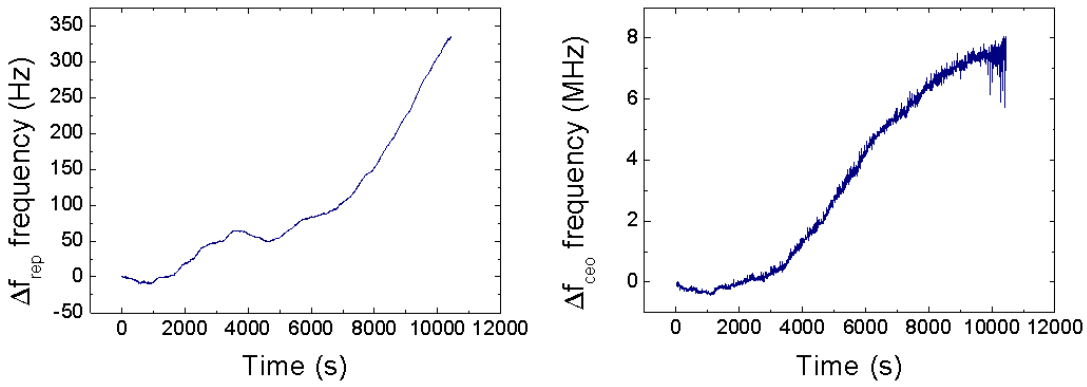

Figure 3.8: The passive stability of our OFC.

of PZT becomes a common technique for such requirements. Then the f_{rep} can be controlled by acting with PZT's on the cavity length.

The mirror, PZT and mirror mount form a system characterized by their mechanical resonances Ω^i_{res} and since this system is inside the feedback loop we can expect stable operation only at frequencies below the lowest resonance $\Omega_{res,low}$. This frequency is a function of the mass of the mirror, the mass of the mirror mount or counterweight, and the way the PZT and the mirror are connected. The first improvement is to use the smallest possible mirror substrate and PZT glued with a hard compound onto a massive backplate as the counterweight. This type of solution is found in many commercial systems, for example in any laser system with a extended optical resonator.

Such solution can give a large bandwidth of PLL (in some systems up to 180 kHz [183], see the idea in the App. F.3). However, small fast PZT are generally limited in the maximum excursion. This limits the maximum tuning of the f_{rep}. For example, PZT with sensitivity 0.05 nm/V and maximum voltage 100 V can tune f_{rep} within 0.3 Hz. For this reason it is often implemented a second actuator with a high voltage or multi-stack PZT that can correct the larger drifts at low frequency.

In our cavity we use as fast actuator a small plane mirror Layertec 108167 (diameter $d = 6.35$ mm, thickness $t = 3.0$ mm) glued to a fast PZT (Noliac^{TM} CMAR01, operating voltage 200 V, free stroke 2.7 μm), to a massive brass mount. The mount has an irregular shape with maximum dimensions $20 \times 20 \times 50$ mm.

Its mechanical resonances were investigated by interferometric method and the frequency and phase resonance we observed first at $\Omega_{res,low} \approx 40$ kHz. A slow PZT is fixed on an output coupler mirror in a normal mirror mount. It has an operating voltage of 150 V and can tune the f_{rep} of about 50 Hz.

Acoustooptic Modulator The f_{CEO} depends mostly on dispersion in a fs cavity (see Eq. 2.61). The easiest way to change the cavity dispersion is to change the intracavity power. Sufficiently fast for this task are acoustooptic modulators (AOM). Our AOM is from IntraAction Corp. and its optical rise-time is less than 265 ns, with a bandwidth of about 1.8 MHz (these parameters depends on beam diameter). The AOM is placed in the noise eater configuration (Fig. 3.9) in which varying the amplitude ΔA of the driving signal $\cos(\omega_{AOM} t)$ proportionally changes the light power in the first diffracted order ΔP, thereby modulating the power on the undiffracted beam $P - \Delta P$.

In our case, the AOM is aligned to have the power in the 1st order ΔP within 1% of P. The RF power to modulate the AOM is 16 dB (comes from the RF generator through Amplifier Mini-Circuit, model #ZHL-3A).

The sensitivity of the f_{CEO} to the pump power modulation is not linear (as was discussed in SbSect. 2.6.5 and will be shown in SbSect. 4.1.3). However, it is always possible to find a linear region of f_{CEO} dependence from the pump power $\delta f_{CEO}/\delta P$ (see Fig. 4.1a). In this region a typical sensitivity of the f_{CEO} is ~ 2 MHz/100 mW. That for 1% power modulation at P=4.5 W corresponds to $\Delta f_{CEO} \sim 900$ kHz.

The value of the ΔP is chosen small to avoid f_{CEO} overrunning from the linear response of $\delta f_{CEO}/\delta P$ (see Fig. 4.1a).

For the QOS OFC the $\delta f_{CEO}/\delta P$ is always linear (as far as we observed) and equal ~ 2 MHz/100 mW (see Fig. 3.17b).

Pump beam horizontal shifting For the same reasons as for f_{rep} stabilization, for a f_{CEO}case is also useful to have two PLL loops. A fast one is based on the AOM. A slow control is obtained by a pump beam shift.

To shift the pump beam through the fs cavity we are using a stack low voltage ring actuators (model HPSt 150/14-10/12, Piezomechanik GmbH) with 0.08 μm/V sensitivity. Due to the fact that the maximum voltage must never exceed 150 V

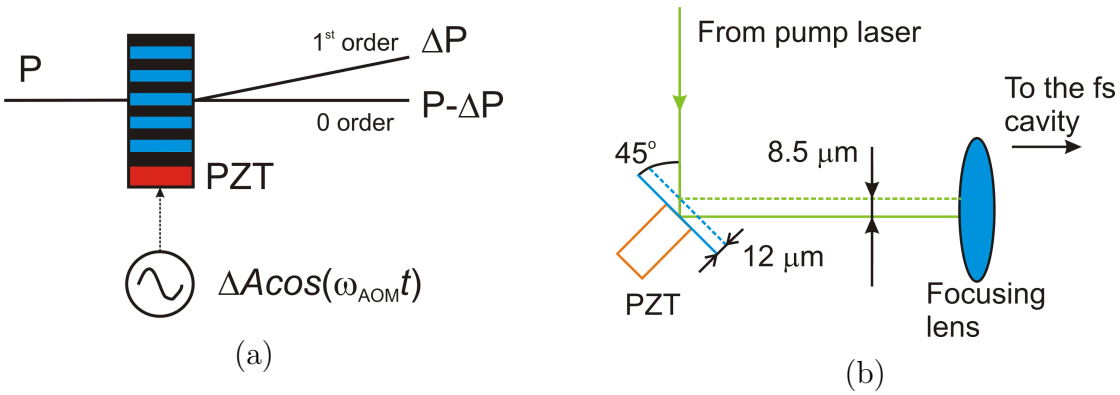

(a) (b)

Figure 3.9: (a) Configuration for using an AOM as a noise eater. Varying the amplitude of the driving signal proportionally changes the light power in the first diffracted order, thereby modulating the power on the undiffracted beam. (b) Pump beam horizontal shifting.

and that the shifting mirror placed at 45°, the calculated maximum beam shift of the pump beam X_{pb} on the focusing lens was estimated to be around 8.5 μm (see Fig. 4.1b). We measured the the corresponded sensitivity of the f_{CEO} as a function X_{pb} near to the "turning point" by slowly changing the voltage of the pump mirror PZT. The sensitivity was found to be $\sim 5 - 15$ MHz/150 V (see SbSect. 2.6.5 and SbSect. 4.1.3).

3.1.6 Final design

Fig. 3.10 shows the experimental design of our OFC with a detailed scheme of the Ti:Sa cavity (presented the version with GTI mirrors). All the mirrors (except the output coupler) are dielectric coated with $> 99\%$ reflectivity at the central wavelength of 800 nm. The pump beam is coupled into the cavity by a lens of focal length 75 mm through the dichroic curved mirror M1. The flat side of this mirror was AR coated for 532 nm to minimize losses.

Two PZTs actuate the flat folding mirror M3 and the OC of the Ti:Sa cavity for the control of the f_{rep} respectively for the fast (up to 40 kHz) and slow control.

The slow drift of the offset frequency f_{CEO} was controlled by observing the f-$2f$ interferometer (see SbSect. 3.1.8), actuating through a PZT on the position of the pump mirror (PM), while the short pumping power term stability (up to 100 kHz)

is provided by stabilizing the amplitude of the pump beam by AOM.

The positions of the curved mirrors are critical for producing a fs regime. Typically, a KLM is obtained by displacing one curved mirror away from the optimum mirror position for a cw operation.

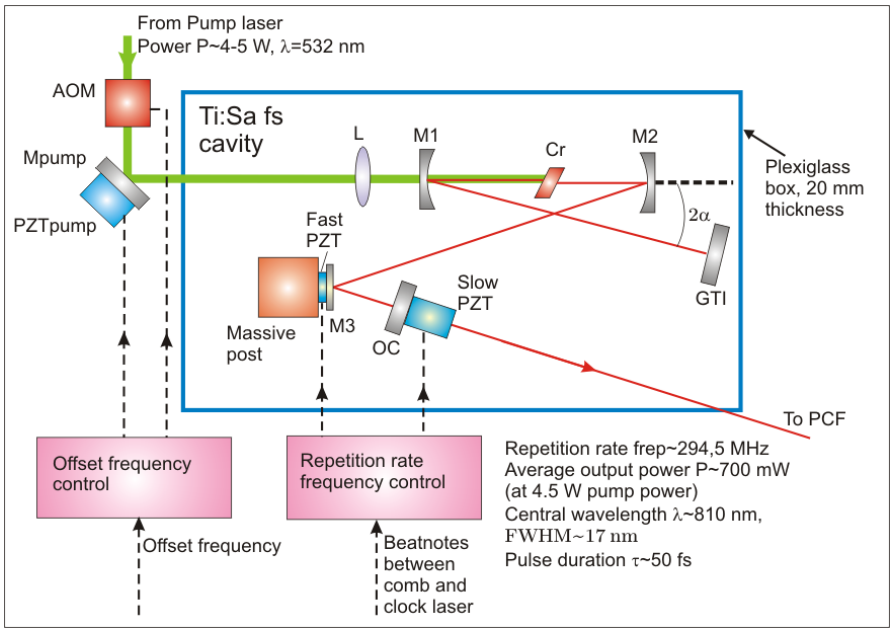

Figure 3.10: Experimental setup of Ti:Sa OFC. Prismless Ti:Sa laser cavity composed by M1 and M2 - curved mirrors, M3 - flat mirror, OC - output coupler, GTI - Gires-Tournois interferometer, α - astigmatism compensation angle; PCF - photonic crystal fiber, L - focusing lens, MP - pump mirror with PZT, AOM - acouso-optical modulator.

3.1.7 Photonic crystal fiber

Microstructure fibers played a key role in the production of coherent OFCs that span more than an octave of bandwidth. Theoretical aspects of the supercontinuum generation from a PCF were described in SbSect. 2.4.

Our PCF, type Femtowhite 800 from Crystal-Fibre, is a polarization-maintaining supercontinuum device for use in the 800 nm-range femtosecond lasers. It is a highly nonlinear, polarization-maintaining photonic crystal fiber with zero disper-

sion at 750 nm (see Fig. 3.11a). The fiber ends are sealed and mounted in quartz ferrules, and the polarization axis is indicated on the device. The nonlinear fiber is mounted in a robust aluminum housing, which can be easily mounted on a mount. The end facet of the device is shown schematically in Fig. 3.11.

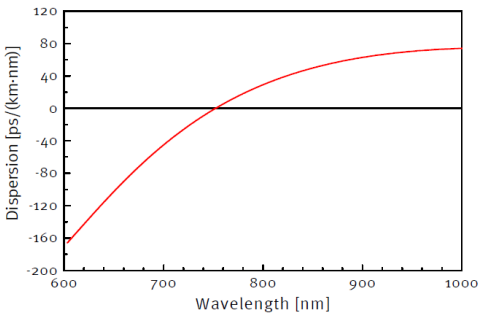

(a)

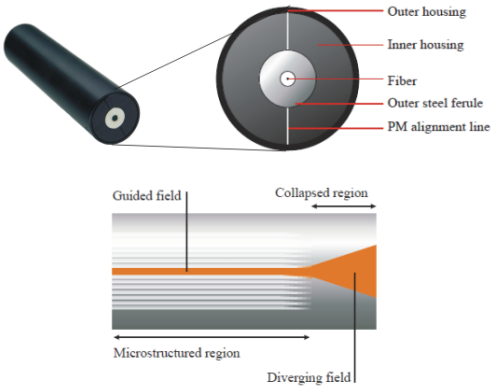

(b)

Figure 3.11: (a) Typical measured dispersion of the fiber in the FEMTOWHITE 800. Fig. from Appl. note for FEMTOWHITE 800. (b) Principle behind the beam expansion in the device. The figure shows the end of the fiber where part of the microstructure has been collapsed.

The microstructure in the fiber is collapsed over a distance of approximately 100 μm, causing the field to diverge into a larger spot size. The spot size in the raw fiber is approximately 1.6 μm, which is increased to $\times$ 2.3 μm as the effective spot-size to focus to at 100 μm from the end facet. The corresponding spot-size will be $\times$ 30 μm on the fiber end facet.

The PCF is placed in a V-shaped fixed aluminum mount. To align PCF the input and output collimators are placed in 2-axis translational stages. This solution give us a stable alignment of both the input coupler and the output coupler.

The input collimator was chosen from equation:

$$\varphi_{spot} = \frac{4\lambda f}{\pi D} \tag{3.14}$$

where f is a focus length of the lens, λ is a wavelength, D is a diameter of collimated beam, incident on lens. From the PCF data-sheet $\varphi_{spot} \leq$ MDF@780(focus) =

2.3 ± 0.3 μm, our $D \approx 1.7$ mm is measured by the knife-edge method (App. G.1) and fitted with the error function (App. G.2):

$$erf(x) = \frac{2}{\sqrt{\pi}} \int_0^x e^{-t^2} dt \tag{3.15}$$

For $\lambda = 800$ nm $f \leq 3.8 \pm 0.5$ mm. In practice we used a collimator C390TM-B from Thorlabs with $f = 2.75$ mm. The coupling efficiency of the PCF is $\approx 50\%$.

The optical spectrum after PCF is presented in Fig. 3.12. On this graph are also shown the wavelengths for which is necessary to have enough power in supercontinuum for our measurements: 532 nm and 1064 nm for f-2f interferometer, 698 nm for beatnotes with the clock laser, 689 nm for beatnotes with 689 nm laser. Our optical spectrometer is limited in wavelength over ~ 1000 nm and optical spectrum higher that this wavelength can't be presented. Instead we put the power level at $\lambda = 1064$ nm, measured by photodiode. The power distribution across supercontinuum is not constant. A small disaliments of PCF due to, for example, thermal fluctuations, can change it a lot. This can lead to situation where the power levels in the needed regions are insufficient. By rotating a $\lambda/2$ plate before the PCF, we can adjust the power distribution across the supercontinuum in order to find the best operative conditions. By the way, this instability is a problem for long-time frequency measurements.

3.1.8 f-$2f$ interferometer

The f_{CEO} is detected by f-$2f$ interferometer. Principle of the detection was discussed in the Sect. 2.3. In our case, the nonlinear crystal, that doubles the optical frequency, is a beta-barium-borate (BBO) crystal, type I. We chose the initial focusing parameters the same as in the experimental setup in the optical clock laboratory in ILP SB RAS (see App. A) and further optimized them.

To observe f_{CEO} signal, the delay between the two interferometer arms demands to be well adjusted. That is achieved by implementation of a fused-silica prism placed on an adjusted micrometer stage in of the arms.

In order to reduce the noise in f_{CEO} signal, we carefully optically filtered incoming beams in the interferometer. The beam is coming on an input mirror (Meller Griot (LWP-45-RS532-TP694-PW1025-UV)), that transmits in the red and infrared regions and reflects to the first interferometer arm the wavelength in the

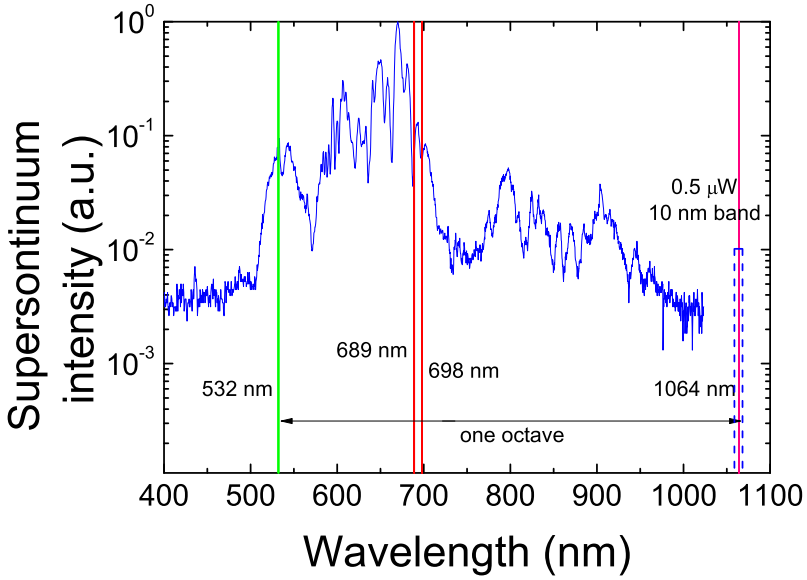

Figure 3.12: Supercontinuum optical spectrum after the PCF. Also there are shown important optical wavelengths for which is necessary to have enough power in supercontinuum: 532 and 1064 nm for f-2f interferometer, 698 nm for the beatnote with clock laser, 689 nm for the beatnote with 689 nm laser. At 1064 nm it is shown the power, measured by photodiode.

range 550 ± 50 nm. This beam reflected by the prism and is sent to the beamsplitter for beatnotes with beam from a second interferometer arm. The transmitted light after the input mirror is coming on a mirror from Meller Griot (SWP-45-RS1064-TP694-PW1025-UV), that reflect infrared wavelength with $\lambda = 1050 \pm 50$ nm into the interferometer arm with nonlinear crystal, and transmit a red light of wavelength $< \lambda = 700$ nm. This red part is used for beatnotes between the OFC and 698 nm and 689 nm lasers (see the Sect. 5.2). The infrared beam in interferometer becomes green after the BBO crystal and sent to the beamsplitter for beatnotes with green light of the first interferometer arm. After the beamsplitter, the light is filtered by a filter centered at $\lambda = 532$ nm with a passband of 10 nm. Then it focused to a fast photodiode by a lens with focus length $f = 50$ mm. This photodiode is typically used also for the detection of the f_{rep}.The observed f_{CEO} signal was 40-50 dB in 10-300 kHz bandwidth with the focal lens $f = 60$ mm,

$L_2 = 58$ mm, input beam radius, measured by the knife-edge method, ~ 3 mm.

For this parameters, the calculated waist of the beam inside the crystal $w_0 = 13.5\mu$m (see Fig. 3.13), the wave vector $k = 2\pi/\lambda_{1064} = 5.9 \times 10^6$ 1/m; the confocal parameter $b = k \times w_0^2 = 5.9 \times 10^6 \times (20 \times 10^{-6})^2 = 2.36$mm; $L/b = 4 \times 10^{-3}/2.36 \times 10^{-3} = 1.7$, where L is the crystal length.

Despite the good f_{CEO} S/N, from the theoretical point of view, this result could be further improved. The theoretical study of second-harmonic generation (SHG) using focused Gaussian beams by *Boyd* and *Kleinman* [184] has long been a reliable resource for those studying frequency-conversion processes. However, the Boyd-Kleinman theory applies only to cw beams and cannot be relied upon to describe harmonic generation correctly using fs pulses.

A theoretical model that describes SHG using fs pulses, by taking into account the associated critical effects of GDD was presented by *Saltiel* et al. in [185].

According to this model, in order to obtain the maximum frequency-doubling efficiency, three parameters must be optimized:

- the GDD, which accounts for the temporal walk-off between the fundamental and second harmonic pulses in propagation through the nonlinear medium. GDD is defined by a nonstationary length $L_{nst} = \tau/\alpha$, where τ is the time duration of the fundamental pulses, and the GDD parameter, $\alpha = 1/v_2 - 1/v_1$, where v_2 and v_1 are the group velocities of the second harmonic and fundamental wave respectively;

- the position of the focal spot, m;

- the strength of focusing, m = L/b, ($b = k_1 w_{01}^2$, where w_{01} and k_1 are the focal spot radius and the wave vector of the fundamental wave respectively).

The theory of SHG using focused cw beams [184], where GDD is negligible ($L_{nst} \gg L$), predicts an optimal focusing condition which is expressed by the ratio $L/b = 2.83$ (in our case $L/b = 1.7$). However, the theoretical model [185] for the cases where GDD is significant (i.e. where $L \geq L_{nst}$), says that depending on L/L_{nst} the optimum value for the ration L/b can be approximately one order of magnitude times greater.

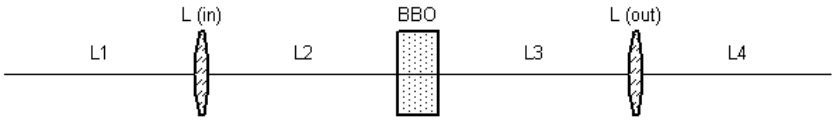

Figure 3.13: Scheme for beam focusing in BBO crystal $L_1 = 100$ mm, L_{in} focus length $f_{in} = 30$ mm, $L_2 = 28.9$ mm, BBO thickness $t = 4$ mm and index of refraction $n = 1.65$, $L_3 = 30$ mm, L_{out} focus length $f_{out} = 30$ mm and input waist radius $r = 0.5$ mm.

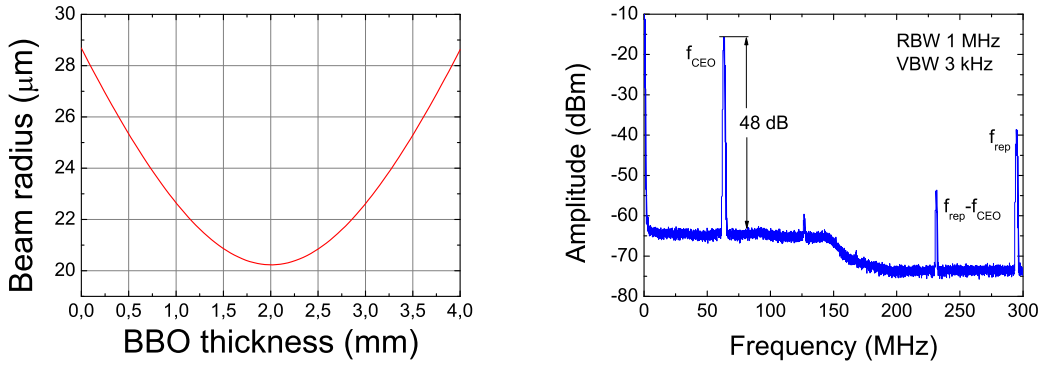

(a) (b)

Figure 3.14: (a) Scheme for beam focusing in the BBO crystal. (b) Typical f_{CEO} signal.

3.2 Quasi-octave spanning OFC

3.2.1 Main characteristics of QOS OFC

We also tested a Ti:Sa OFC in a regime with a large spanned optical spectrum ($>$ 100 nm), refereed here as quasi octave-spanning (QOS) OFC. This regime, at difference from the EB OFC regime, do not present a "turning point" (see SbSect. 2.6.5) and its f_{CEO} as a function of pump power has a simple linear dependence (see SbSect. 2.6.4).

The QOS OFC is realized modifying the fs cavity by replacing the GTI mirror by a chirped GDD mirrors pair plus one GDD mirror (Fig. 3.15). As was noted in SbSbSect. 3.1.4, this step reduces the total intracavity dispersion from ~ -400

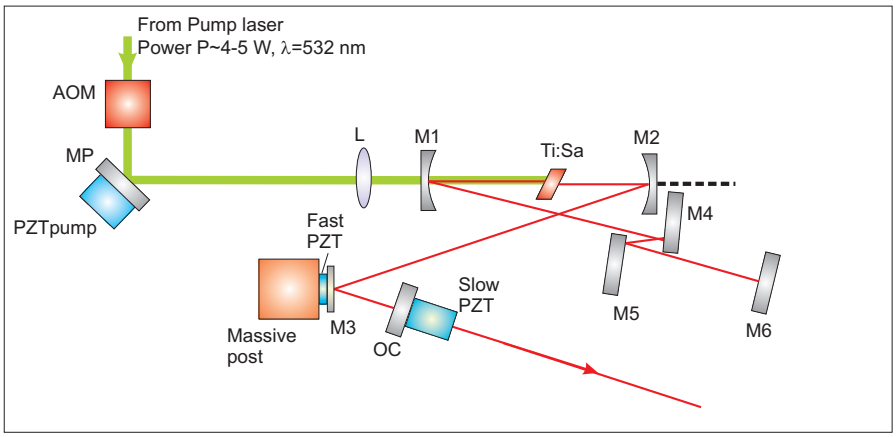

Figure 3.15: QOS OFC cavity scheme. The GTI mirror from Fig. 3.10 is replaced by chirped pair mirrors M4, M4 and GDD mirror M6.

fs^2 to ~ -175 fs^2. By final adjustment of the Ti:Sa cavity, it is possible to find the regime when the emitted optical spectrum directly from the Ti:Sa laser has a span about $700 - 900$ nm. An optical spectrum at different pump power levels is shown in Fig. 3.16. We believe, that the only reason why it is not an octave-spanning is a limitation of our cavity mirrors coatings. Our output coupler has a reflectance in 750-850 nm band. A full-octave spectrum with an output coupler reflectance band of $680 - 880$ nm was demonstrated, for example, by Bartels for a Gigahertz femtosecond laser [42]. On the Fig. 3.16b is presented the broadest observed optical spectrum with our QOS OFC.

QOS OFC output power as a function of the pump power presented in Fig. 3.17. Regions 4.0-4.5 W, 4.55-5.5 W and 5.5-6.1 W have different efficiencies. This fact also corresponds to different sensitivity of f_{CEO} as a function of the pump power (Fig. 3.17b). The last region at 5.5-6.3. W the continous wave components is observed in the optical spectrum, that explains the higher efficiency in this region. Also was observed different phase noise of f_{CEO} at these regions (Fig. 3.17b inset graphs shows f_{CEO} signals).

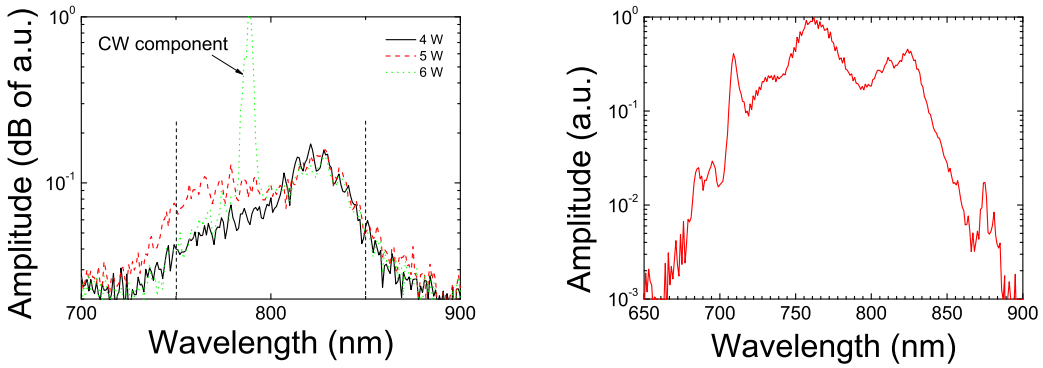

(a) (b)

Figure 3.16: (a) QOS OFC output optical spectrum at different levels of the pump power. Vertical dashed lines shows a reflectance band of our output coupler. (b) - QOS OFC broadest observed output optical spectrum.

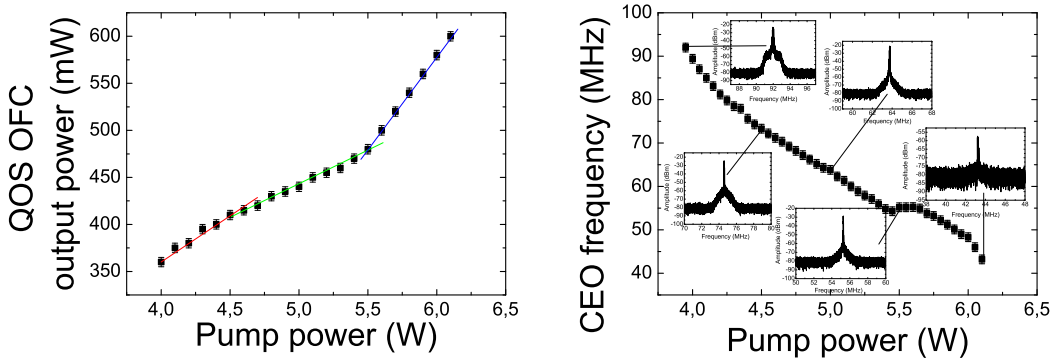

(a) (b)

Figure 3.17: (a) QOS OFC output power as a function of the pump power. (b) - f_{CEO} as a function of the pump power (case of the mml).

3.2.2 Passive stability of QOS OFC

Interesting results gives the passive stability measurement. In Fig. 3.18 typical behaviour of the f_{rep} of free-running QOS FOC is presented. Compared with free-running EB OFC case, a f_{rep} as a functon of time is changing faster ($\sim$ 1.25 Hz/s), but always has trend in one direction.

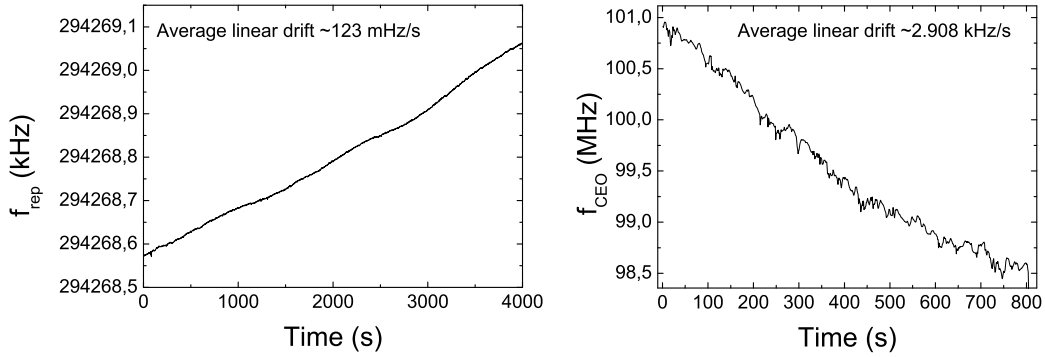

(a) (b)

Figure 3.18: (a) f_{rep} of the free-running QOS FOC. (b) f_{CEO} of the free-running QOS FOC.

3.3 Clock laser

The clock laser used to probe the $^1S_0$-$^3P_0$ strontium clock transition is a frequency-stabilized diode laser at 698 nm.

The master laser is a commercial diode laser (Hitachi HL6738MG, without AR-coated) mounted in an extended cavity (Littrow configuration) with a length of 30 mm. The diode operates at around 40°C and delivers about 10 mW of optical power at 83 mA driving current. The free running ECDL exhibits a frequency noise spectral density $S_\nu(f) \simeq 4.6 \times 10^8/f$ (Hz^2/Hz) up to few MHz until it reaches its white noise plateau at 10^3 (Hz^2/Hz) [186, 187].

Due to residual sensitivity to other environmental noise source, the stability of the locked laser is $\sigma_y = 1 - 2 \times 10^{-15}$ for integration times between 1 s and 100 s. For longer integration times, a residual 1 Hz/s cavity drift degrades the frequency stability. Accuracy and long-term stability is achieved by referring the laser to the clock $^1S_0$-$^3P_0$ transition of ultracold bosonic ^{88}Sr isotope confined in a optical lattice trap. [188].

The laser linewidth is reduced by Pound-Drever-Hall (PDH) frequency stabilization to optical cavities [189]. We use a first stabilization step to reduce the linewidth to < 1 kHz by locking the laser to a resonance of a pre-stabilization cavity. Then, we reduce further the linewidth by locking the pre-stabilized laser to a resonance of an ultra-high-finesse cavity [190, 191].

The first pre-stabilization cavity is realized with an Invar spacer sitting on a v-shaped aluminum block. It has a finesse of 10^4 and the resonance is about 150 kHz wide. The servo correction signal is sent to two actuation channels. As shown in Fig. 3.19, one is sent to a PZT attached to the extended cavity grating, while the second goes directly to the diode current with a servo bandwidth of about 2 MHz [169, 187, 192].

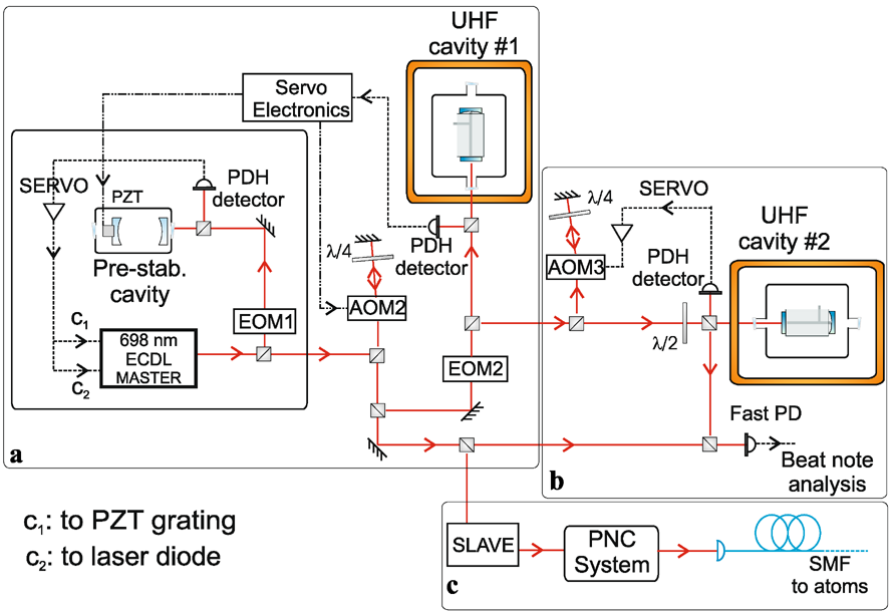

Figure 3.19: Experimental setup for the 698 nm clock laser frequency stabilization and characterization. Block (a): master diode laser with two-stage frequency stabilization; (b): second independently-stabilized ultra-high-finesse cavity and beat note interferometer to make laser characterization studies; (c) noise-compensated fiber link which deliver interrogation laser to the atoms. UHF: ultra-high finesse; AOMi : acousto-optic modulators; EOMi : electro-optic modulators; SMF: single-mode optical fiber; PNC: phase noise cancellation system [169].

The key feature of our frequency-stabilized clock laser is the ultra-high-finesse Fabry-Pérot resonator used as a local frequency reference. The high finesse cavity is realized with a 10 cm long ULE (High grade Corning 7972 glass) spacer with two optically contacted SiO_2 mirrors. The geometry of the spacer has been optimized with the help of finite element analysis (FEM) to reduce the effect of the

deformation induced by vibrations coming from the optical table [193]. The cavity is supported horizontally under vacuum (10^{-8} Torr, maintained with a 20 l/s ion pump) with two aluminium arms connected by three low-expansion invar shafts. The effective supporting points are four 2mm^2 square areas with Viton square pieces placed between the aluminium supporting points and the ULE spacer surface. The vacuum chamber has been built with thick aluminium walls (5 cm) to increase the thermal inertia of the system. The temperature of the outside surface of the vacuum is actively stabilized at 25 °C with a residual error in temperature of 25 mK by controlling the current passing through a high resistance (Alumel) cable wound around the can itself. With the help of finite element analysis (FEM) simulation we checked the cavity static distortion induced by accelerations in both vertical and horizontal directions, as a function of the position of the supporting points along the longitudinal z-axis of the cavity.

The thermal noise limit (see Fig. 3.20a) of our cavities has been estimated by taking noise values for ULE, fused silica and mirror coating as reported in the literature [194]. This value is about 3 times smaller with respect to the noise level in vertical cavities realized at the same wavelength for similar purposes [191], which yields a fractional frequency stability of 3.8×10^{-16}.

The finesse of the high finesse cavity has been deduced both by measuring the photon cavity lifetime $\tau = 43(2)\mu$s and by directly observing the linewidth $\Delta\nu = 3.7(0.5)$ kHz of the TEM_{00} mode of the cavity. The finesse measured is 4.1×10^5 within 4% of error, corresponding to 7 ppm total losses for each mirror [187, 195].

The second stabilization loop acts at low frequencies (up to 1 kHz) on the PZT of the pre-stabilization cavity to compensate for low frequency drifts, and at high frequency (up to 50 kHz) to the AOM used to shift the frequency of the laser through the driving RF frequency generator. The power coupled into the high finesse cavity, when the laser is locked to the lowest TEM_{00} mode of the cavity is about 60%, while the transmission is typically of the order of 15%, consistent with the measured mirror losses.

In Fig. 3.20a we show reported the frequency noise of the stabilized laser source, which was measured by sending part of the light, frequency shifted with an AOM, to a second independent high finesse cavity sitting on the same optical table, and analyzing the error signal obtained when the frequency of the beam is steered around the resonance of the second cavity. From the analysis of the error signal

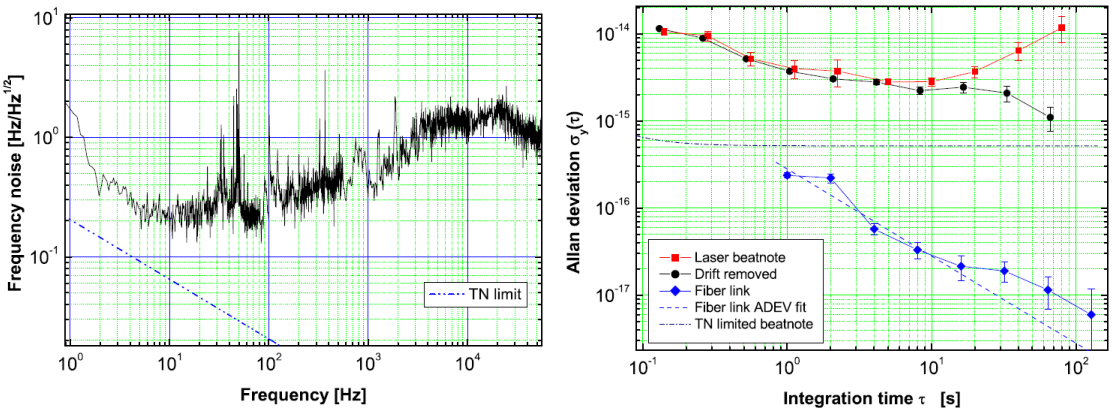

(a) (b)

Figure 3.20: (a) The frequency noise of the stable 698 nm laser source locked to its ultra-high-finesse cavity. The dashed line represents the calculated thermal noise limit due to the contribution of the ULE spacer, the fused silica mirror substrate and the Ta_2O_5/ SiO_2 coating. The spectrum takes into account the cavity response curve [169]. (b) Stability curves for the clock laser system. The plot shows the Allan deviation for the frequency-stabilized clock laser which approaches the thermal noise limit (dot-dashed line), while the fiber link does not limit the potential stability of the laser system. The dashed line corresponds to a white phase noise-limited Allan deviation $\sigma_y^{clock}(\tau) = 2.8 \times 10^{-16}\tau^{-1}$ for the fiber link [169].

on the second stabilization loop, we can calculate a laser linewidth of the order of 1 Hz.

The Allan deviation were measured by counting the beat note frequency with different gate times. The result (see Fig. 3.20b) is calculated by removing the linear drift with a computer controlled RF generator. The minimum $\sigma_y(\tau)$ is $1.1(3) \times 10^{-15}$ at $\tau = 67$ s.

A preliminary measurement of the thermal expansion coefficient near room temperature has been done by changing the temperature of one of the cavities while maintaining the other one stabilized and measuring the relative shift in the TEM_00 mode of the two cavities. We found a mean value of $5 \times 10^{-8}K^{-1}$ for the CTE (Coeff. of Thermal Expansion) in the temperature range of 22 - 25 °C.

Ultimately, we checked the sensitivity to acceleration of the stabilized laser system, by observing the frequency noise imposed into the laser by acceleration in

both vertical and horizontal directions. The acceleration noise has been measured with a triaxial accelerometer (Kinemetrics Episensor), while the frequency noise has been measured by using a resonance of the second high finesse cavity as a frequency discriminator. We found a value of 3 kHz/ms^{-2} and 20 kHz/ms^{-2} for the sensitivities respectively for vertical and horizontal directions, in good agreement with the results of our FEM simulations.

Chapter 4

Analysis of OFC frequency noise

In this chapter it is presented a detailed analysis of the frequency noise of EB OFC in free-running mode (Sect. 4.1). This information we will use to optimize the stabilization of the EB OFC (Sect. 4.2). In Sect. 4.3 we will discuss about the frequency stability of the stabilized EB OFC across all components. The last Sect. 4.4 consist the information of the sabilization results of the QOS OFC.

4.1 Free-running OFC behaviour

To optimize the controls for f_{CEO} and f_{rep} we studied the OFC intensity-related dynamics and determined the main frequency noise sources for the free-running OFC. The OFC tooth frequency noise estimations were proved with the experimental measurements of the f_{CEO} and the f_{b698} frequency linewidths.

4.1.1 Fixed point formalism

The power of the fixed-point formalism (SbSect. 2.6.2) to describe intracavity noise terms for a fs fiber laser was demonstrated by *Newbury* and *Swann* in [96]. We use the same approach to describe frequency noise of our Ti:Sa OFC. In the fixed point model each source of perturbation e.g. pump power, laser cavity, pump beam fluctuations etc. will cause the comb to expand or to contract about a single fixed frequency, ν_0^X. Mathematically, $\nu_0^X = n_0^X f_{rep} + f_{CEO}$, where $n_0^X = (\delta f_{CEO}/\delta X)/(\delta f_{rep}/\delta X)$, and X is the perturbation source [96, 113, 114]. The last equation implies that ν_0^X can be measured experimentally by changing a

given parameter (e.g. pump power, cavity length, pump beam position) and by measuring the resulting change of f_{rep} and f_{CEO}. To measure the low-frequency response of the OFC parameter to a given parameter fluctuation, we weakly modulate pump power, laser cavity and pump beam mirror PZT voltages with a 1-10 Hz frequency, and we monitored the resulting modulation of f_{CEO} and f_{rep} using frequency counters. This measurement was repeated for different settings of the given parameter modulation depth and, thus generating a series of values of df_{CEO}/dP and df_{rep}/dP. Thus, here we used a simple linear approximation and applied slow perturbations and than we averaged the data. For the fast perturbations the fixed point will be different (see the full transfer function study by *Schilt* et al. in [196]).

4.1.2 Characterization of the frequency noise terms

To develop a quantitative picture of the frequency noise, we will describe the frequency noise of each tooth of the comb through its noise power spectral density (PSD), $\int_0^\infty S_{\nu n} df = \langle \sigma_n^2 \rangle$, where $\langle \sigma_n^2 \rangle$ are the mean squared fluctuations of comb mode of index n. The total frequency noise PSD from multiple, uncorrelated noise sources is calculated by simply adding up the noise PSDs from the various sources, giving similarly as in [96]: $S_{\nu n}(f) = (S_{\nu n}^L(f) + S_{\nu n}^P(f) + S_{\nu n}^{ASE}(f)) + (S_{\nu n}^{SC}(f) + S_{\nu n}^{ShN}(f))$, where $S_{\nu n}^L(f)$ is the cavity length noise, $S_{\nu n}^P(f)$ is the amplitude noise of the pump laser and $S_{\nu n}^{ASE}(f)$ is the amplified spontaneous emission (ASE) PSDs. These intracavity noise terms can be described using the fixed-point formalism as [96]:

$$S_{\nu n}^X(f) = (\nu_n - \nu_0^X)^2 s_{rep}^X(f) \tag{4.1}$$

where $s_{rep}^X(f) = f_{rep}^{-2}(\delta f_{rep}/\delta X)^2 s_X(f)$ is the PSD of the fractional repetition-rate fluctuations driven by the fluctuations in the parameter X.

Other extracavity noise terms are respectively given by the supercontinuum noise PSD $S_{\nu n}^{SC}(f)$ and the shot noise PSD $S_{\nu n}^{ShN}(f)$.

4.1.3 Turning point

As pointed out in Sect. 2.6.3, 2.6.5, in a Ti:Sa OFCs, in which the fs pulse spectrum does not fill up all the available optical spectrum bandwidth, f_{CEO} shows a non-linear dependence as a function of pump laser intensity. Fig. 4.1a demonstrates a typical dependence of f_{CEO} as a function of the pump power for our fs laser. In particular we can observe a stationary point of f_{CEO} at about 4.5 ± 0.2 W (often referred as "turning point" [112]). For this value of pump power f_{CEO} is very insensitive to intensity changes in the cavity. The parameter of f_{CEO} sensitivity to intensity change is also critical to the cavity alignment. Near to the working point the linewidth of the f_{CEO} signal becomes smaller reaching its minimum of $\Delta\nu$=15 kHz at 4.36 W, as shown in Fig. 4.1a. This value must be related also to high intracavity dispersion of our cavity of Ti:Sa ($\sim -400\text{fs}^2$). Decreasing this value will reduce the minimum linewidth of f_{CEO} peak.

The measurement of the f_{rep} dependence as a function of the mml pump power is presented in Fig. 4.1b. This dependence has the coincidence with the measurement of the f_{rep} change due to the spectral shift for fiber lasers (see the Fig. 2.9 in SbSect. 2.6.7. While impact of other effects, as TOD, Gain and SS, on the f_{rep} were not observed.

Even if the f_{CEO} has in general a non-linear behavior in function of other fluctuations, we determine all the fixed points in regions where the f_{CEO} has a linear dependence away from the turning points.

The measured values of fixed frequencies are $\nu_0^P = 147$ THz and $\nu_0^L = 2.5$ THz. Our comb spans from 272.7 THz to 625 THz.

4.1.4 Intracavity and extracavity noise sources

The main contribution to the linewidth of each comb tooth comes from the intracavity noise terms. Moreover, among the intracavity terms the following technical noise terms dominate: $S^L_{\nu n}(f)$, $S^P_{\nu n}(f)$. For a Ti:Sa laser the main expected sources of technical noise are given by the pump laser fluctuations and cavity length fluctuations.

Pump laser can introduce noise through its beam-pointing instability and its amplitude noise. The cavity length instead can fluctuate due to many environmental effects: temperature changes coupled to length through thermal expansion,

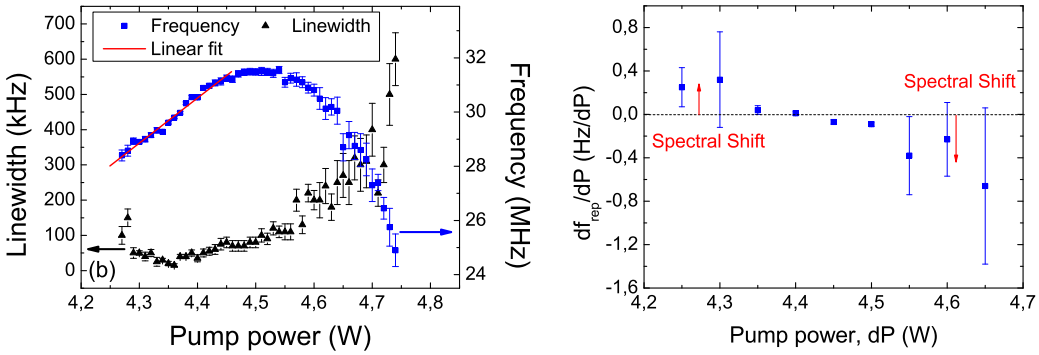

(a) (b)

Figure 4.1: (a) The measurement of the dependence of the f_{CEO} center (squares) and observed linewidth (triangles) as a function of pump power. For this measurement the mml pump laser has been employed. The measured linewidth reaches a minimum of 15 kHz at pump power P=4.35 W near to the turning point for f_{CEO} (see text for details). (b) The measurement of the f_{rep} dependence as a function of the mml pump power. This dependence has the coincidence with the measurement of the spectral shift for fiber lasers (see the Fig. 2.9 in SbSect. 2.6.7. The measurements (a) and (b) were done at different moments.

vibrations through supports and temperature induce fluctuations of the index of refraction of air.

4.1.5 Cavity length perturbations

We estimated the cavity length fluctuation term $S^L_{\nu n}(f)$ from the measured upper limit of the f_{rep} fluctuations at 1 Hz: $\langle|\delta f_{rep}|\rangle = 0.03$ Hz.

Supposing that these fluctuations are caused only by cavity length fluctuations (with a negligibly small contribution due to other effects) we can extract a value for the mean cavity length fluctuations $\langle|\delta L^{meas}|\rangle \approx 0.15$ nm (calculated for the actual cavity length of ~ 0.5 m). From this we then estimate the value of the PSD fractional frequency fluctuation induced by the cavity length fluctuations as follows:

$$s^L_{rep}(1\,\mathrm{Hz}) = \left(\frac{\delta f_{rep}/\delta L}{f_{rep}}\right)^2 s^L(1\,\mathrm{Hz}) = 1 \times 10^{-20} \tag{4.2}$$

For the estimation of comb tooth linewidth, broaden due to the cavity length fluctuations, we supposed a $1/f$ behavior for the quantity $s^L(f)$ before a sharper cut-off above audio frequencies at the frequency f_1. Very far from f_1 we have a $1/[(f_1-f)^2+\gamma^2]$ response, where γ can be of the same order of f_1. The net result is that the frequency noise for $f > f_1$ is filtered.

4.1.6 Amplitude noise from pump lasers

As mentioned before, two different types of commercial pump lasers have been tested with our comb: sml and mml.

As shown in Fig. 4.1.6 in the low frequency range (up to 7 kHz) the measured amplitude noise for the sml is typically higher than the amplitude noise for the mml. On the other hand, in the high frequency range starting from 10 kHz, the mml presents a higher amplitude noise (similar amplitude noise spectra have also been observed in [94, 109]).

Fitting the data, we find for sml a relative intensity noise (RIN) of $s^{sml} = 5\times10^{-9}/f$ Hz^{-1} curve, and for mml a RIN of $s^{mml} = 5\times10^{-5}/f^2$ Hz^{-1}. The PSD describing the fractional frequency fluctuation in terms of the pump laser RIN can then be calculated as [96]

$$s^P_{rep}(f) = Cs^{RIN} \tag{4.3}$$

where the repetition rate sensitivity parameter estimated for the typical power level for our OFC is $C = (P\delta f_{rep}/\delta P f_{rep})^2 = 1.3\times10^{-12}$. By using Eq. (4.3) we calculated the two values $s^{sml}_{rep}(1\,\text{Hz}) = 1.3\times10^{-17}$ Hz^{-1} and $s^{mml}_{rep}(1\,\text{Hz}) = 1.3\times10^{-21}$ Hz^{-1} for the sml and the mml respectively.

4.1.7 ASE-induced noise terms

The ASE-induced noise leads to fluctuations of different cavity parameters that have also different fixed points. However, as was discussed in [96], it can be described by two effects: a timing jitter and a phase jitter. The timing jitter dominates the comb linewidth of the tooth far away from the timing jitter fixed point (typically located near to the OFC carrier frequency) [96]

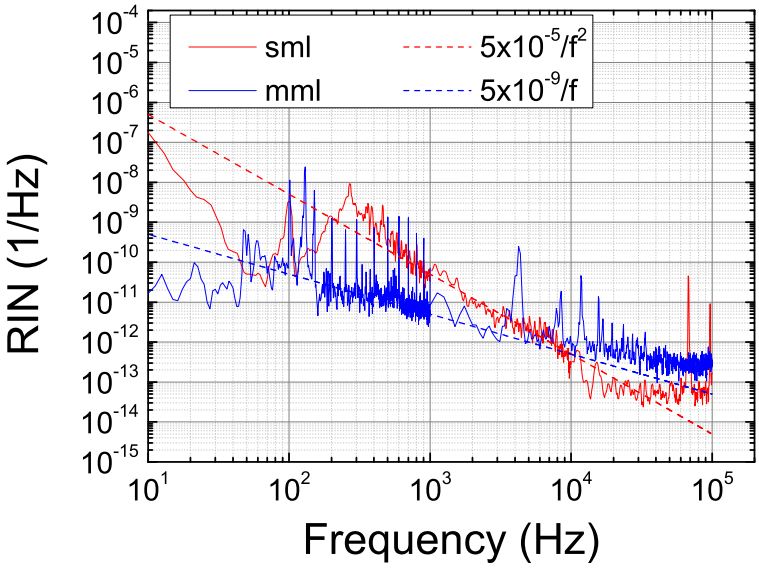

Figure 4.2: Measured amplitude noise of sml (red) and mml (blue) and their fits for frequency noise PSD calculations

$$\nu_0^{ASE,t} \simeq \nu_c \tag{4.4}$$

Using the equation for the timing jitter from [96] we get a value of $s_{rep}^{ASE,t}(1\,\text{Hz}) = 5.6 \times 10^{-28}$ that is negligible compared with other noise terms.

The phase jitter is instead due to the Schawlow-Townes limit [88,90,91], which is the same for all modes and in our case is equal to $\sim 10^{-4}$ Hz/Hz^2 and then also negligible compared to other technical noise terms.

4.1.8 Shot Noise and Supercontinuum Generation

The estimated extracavity noise terms, like the shot noise and the supercontinuum generation noise, were also found to be negligible by comparison with the other noise terms in region 1 Hz - 1 MHz.

To check this experimentally, we test the OFC in the different regime, when the optical spectrum broads from 680 nm to 880 nm. In this case, we measured f_{b698} in two situations. In the first one, we obtain the f_{b698} signal as was described

in **??**. While in the second situation, we split the OFC light before the OFC. One part on the splited beam was sent again to the PCF for the optical broadening and the detecting the f_{CEO}. The beam second part, was sent to the dichroic mirror bypass the PFC and further to the same optical way to detect f_{b698} signal.

The noise level of the detected f_{b698} signal in the case of the PCF in general is 10-15 dB higher than in the case of the f_{b698} detection without implementing the PCF. However, by tuning the waveplate before the PCF and adjusting the proper power level of the coupled OFC light into the PFC, we are able to get the best S/N of the f_{b698}. At this conditions, the noise level with PCF is equal or 2 dB higher that noise level of f_{b698} when the OFC optical spectrum is bypass the PFC. Also we compared the linewidth of the f_{b698} signal in the both cases. In the our level of precision, we didn't find any significant linewidth broadening of the f_{b698} due to the implementation of the PCF.

All the estimated noise contributions are summarized in Tab. 4.2.

4.1.9 OFC tooth linewidth estimation for free-running operation

From calculated frequency noise PSD we can estimate the linewidth of a comb tooth using approximated analytical expressions for simple PSD shapes: $\Delta\nu_n = \pi\sqrt{S_{\nu n}(0)f_c}$ for $S_{\nu n}(f) = S_{\nu n}(0)/(1+(f/f_c)^2)$, $\Delta\nu \gg f_c$ and $\Delta\nu_n = (4\ln(2)K[4.3+\ln(4.3\times 4\pi^2 K\tau_c^{2.1})]^{1/2}$ for $S_{\nu n}(f) = K/f$, if $(2\pi)^2 K\tau_c \gg 1$, where τ_c is the observation time [197] equal to 1 ms, $f_{3\ dB}$ is the 3 dB rolloff frequency. The Fig. **??** is the result of the calculation done for the mml case. The main contributions for OFC tooth frequency noise comes as expected from cavity length deviations. The measured beatnote signal between the optical comb and the clock laser gives a value of 125 ± 25 kHz, that is matched with the lower limit of the OFC tooth linewidth at 698 nm predicted by the model. The big gap between upper and lower limit of the linewidth for the cavity length fluctuations ($\sim$ 176 kHz) is due to the fact that the passive stability of the OFC even within one working day is not the same due to the environmental conditions change (mostly due to the room temperature) and the corresponded fluctuations of the f_{rep} at 1 Hz can be vary by the factor of 2-4 from lower to upper limit. Typically, the best conditions are reached after several hours of the OFC work. The $f_6$98 beatnote linewidth was

measured after 4-6 hours of the OFC work and this can explain why its linewidth matched with the lower limit of the approximation. The result for the pump laser amplitude noise fits with real linewidth of f_{CEO} measured in linear region close to the turning point (see Fig. **??**) and for the lower limit of the cavity length fluctuations it adds significant contribution.

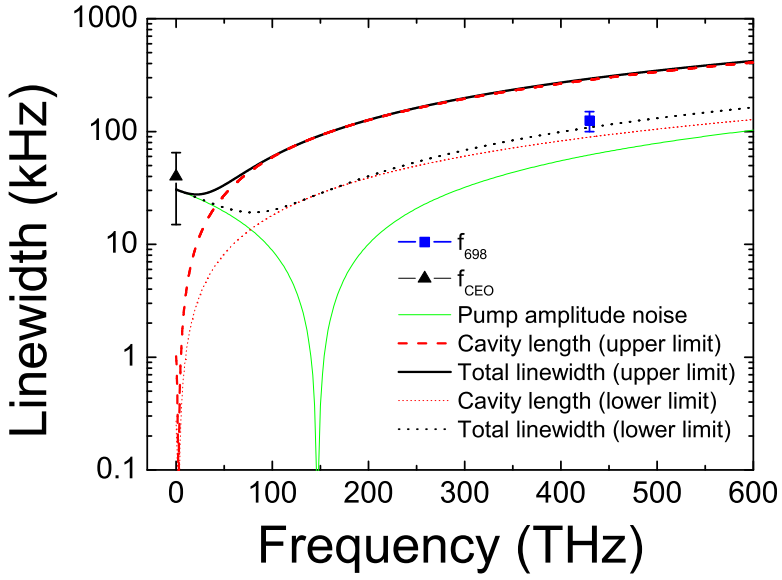

Figure 4.3: The calculated OFC tooth linewidth across the free-running OFC spectrum for pump laser amplitude noise for mml pump case (green dots) and the cavity length fluctuations (red dash) with the measured f_{698} (blue square) and f_{CEO} (black triangle) linewidths. The f_{CEO} linewidth is measured near to the turning point. The total OFC tooth linewidth is shown by the black solid curve.

4.2 Stabilization of the OFC

In Fig. 5.1 the experimental apparatus with details on the electronic devices used for the stabilization of both f_{rep} and f_{CEO} is presented. In next sections I will describe detection of the f_{rep} and f_{CEO} signals and their stabilization.

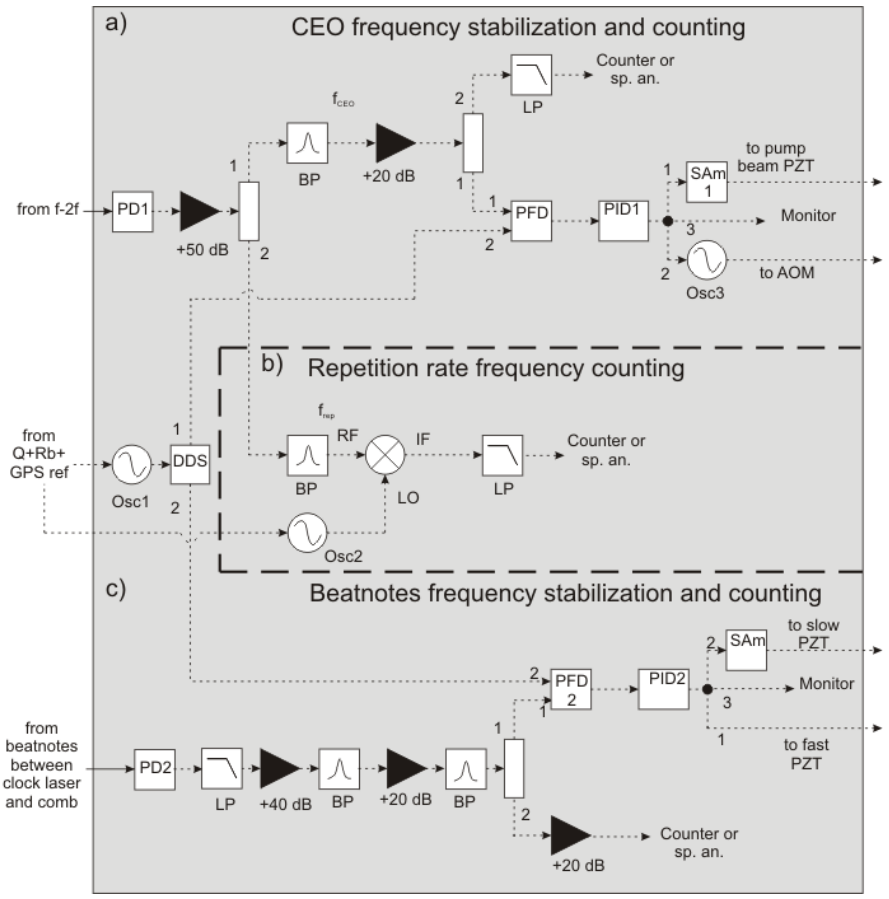

Figure 4.4: Electronics for the OFC stabilization. BP and LP - band- and low pass filters, sp.an - spectrum analyzer, Pd - photodetector, PFD - phase-frequency detector, SAm - servo amplifier, Osc - oscilator, Osc1,3 - HP generators, Osc - Marconi generator.

4.2.1 f_{CEO} stabilization

The f_{CEO} is measured by a standard technique of f-$2f$ interferometer [37]. The f-$2f$ output signal is filtered at wavelength $\lambda = 532 \pm 5$ nm. The signal detected by a fast Si photodiode (up to 500 MHz) is amplified by a low-noise amplifier (Miteq, bandwidth 500 MHz) and split into two channels by a splitter as shown in Fig. 4.4a. The exit 1 from the splitter is sent the signal to a tunable bandpass filter (bandwidth 2 MHz) that is tuned for the f_{CEO} (typically we adjust the OFC to have this value in a region $\sim 20 \pm 10$ MHz) and than it is again amplified

and spitted. A splitter exit number 2 is sent through a tunable low pass filter to a spectrum analyzer or a counter (HP, 12 digits). A typical amplitude of the signal here is $\sim 0 - 10$ dBm with S/N ratio 40 dB (Fig. 4.6) over 100 -300 KHz bandwidth. The splitter output number 1 is sent to the first channel of PFD1. The reference signal coming from a DDS generator is sent to the second channel of the PFD2. The DDS is locked to a reference oscillator (Osc1 - HP generator) which is refereed to a local oscillator (10 MHz). The local oscillator in our case is consists of a high purity quartz slaved to a rubidium standard with is steered at long term to GPS signal. In Fig. 4.5 is presented the Allan deviation of the local oscillator measured at the start of its work. A question about the current stability of it will be discussed in the Sect. 5.1. An error signal from the PFD1, which is proportional to the phase difference between the two input signals, is sent to our proportional-integral-derivative controller (PID1). An exit 2 from the PID1 is sent to an oscillator that is driving an AOM. Thereon a fast loop of the f_{CEO} stabilization is closing. A second part of the PID1 output is sent to a servo amplifier to integrate the error signal and to drive a high voltage multi stack PZT (up to $\sim$ 100 V) in order to compensate a slow drift of the f_{CEO}. The output signal from this servo is sent to a PZT that shifts the pump beam. Thereby the slow stabilization loop is closing. A third part of the signal is used to monitor the quality of f_{CEO} stabilization by an oscillator or a FFT.

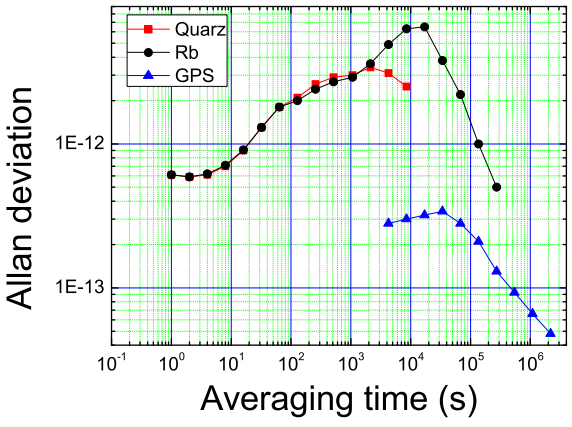

Figure 4.5: Allan deviation of our local oscillator.

The result of the f_{CEO} stabilization with different pump lasers is presented on the Fig. 4.6. Note that in the mml pump case we have implemented the PZT on the pump mirror that reflects the pump beam to the Ti:Sa cavity.

The graph shows that, with our AOM, we achieve 40 kHz bandwidth of the stabilization loop. And using the pump mirror PZT control in the case of mml, we reduced the phase noise of f_{CEO} down to the phase noise level of the sml case in the region 10 - 100 Hz. From 10 kHz Hz the phase noise of locked f_{CEO} with the mml and the sml are at the same level, even the sml case has a worst situation due to the peak at 100 kHz. This peak is that evident also in the RIN spectrum (Fig. 4.1.6a). We note that at the time of these measurements the PLL was not yet optimized, and this can be the main reason why in the mml case phase noise is much higher in 100 Hz - 10 kHz region.

4.2.2 f_{rep} stabilization: lock to the clock laser

In the Sect. 3.3 we noted that our clock laser, stabilized to an high finesse cavity, has a good short-term stability and for this reason it can be used as a frequency standard. In our scheme, the OFC f_{rep} is stabilized in the optical region to this clock laser. The frequency beatnote f_b fluctuations are related to the fluctuations in the frequency of this tooth OFC: $f_{rep} = (f_{698} \pm f_{CEO} \pm f_{b698})/n$. Here f_{698} - the clock laser frequency. In a self-referenced OFC the f_{CEO} is independently stabilized, and the fluctuations f_{rep} can be caused only by the fluctuations of f_{b698}. So, if we stabilize the f_{b698} to a reference, we stabilize at the same time f_{rep}. For this purpose, we achieve the f_{b698} signal by separating an infrared part of the OFC light after the PCF that is not useful for the f-$2f$ interferometer. The shape of the fs beam is corrected by using two cylindrical lenses. The beam is then superimposed on a polarization cube with the light from the clock laser. Then, the two matched beams are first filtered at a wavelength $\lambda = 695 \pm 5$ nm. Finally, beams are filtered by a $\lambda = 698 \pm 0.5$ nm bandwidth filter and beat on a fast photodiode.

On the Fig. 4.4c is presented electronics for the f_{b698} stabilization. The same type of the fast photodiode, as in the case of f_{CEO} detection, is used to detect the beat signal. The power from the clock laser was $\sim$ 2.70 mW and from the femtosecond laser it was $\sim$ 200 μW before the photodector. The beat signal

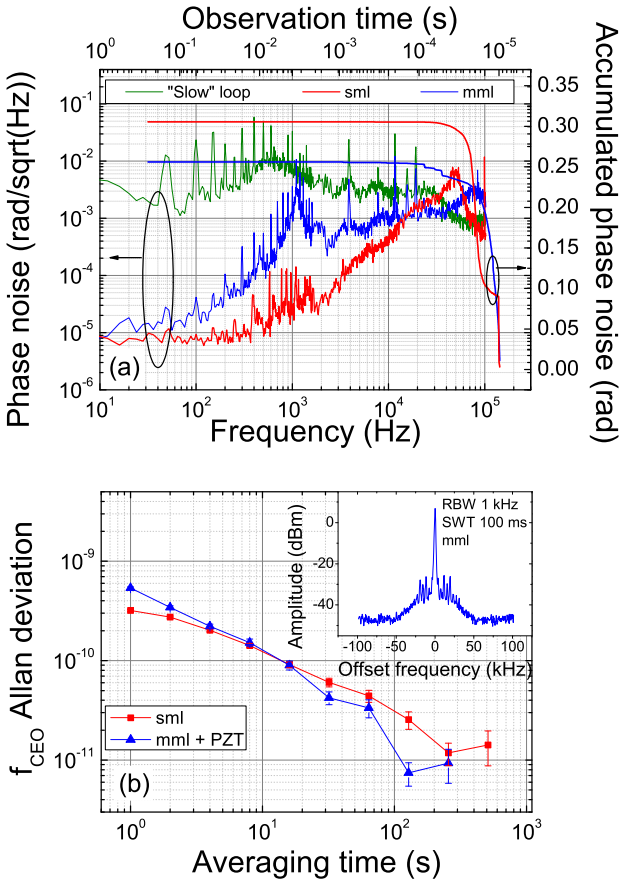

Figure 4.6: The noise spectral densities and the relative estimated Allan deviations of the phase-locked f_{CEO} (a),(b). (a) The measured phase noise of the locked f_{CEO}. Upper green curve: slow loop f_{CEO} phase noise (mml case) measured with a slow servo loop ($\leq$ kHz)acting on the pump laser AOM, when f_{CEO} was weakly locked at low frequencies, middle blue and lower red curves: the closed loop f_{CEO} phase noise with mml and sml pumps respectively. Blue and red lines show the accumulated phase noise respectively for mml and sml. Ellipses and arrows indicates to which vertical scale the curves are referred. (b) The Allan deviation for the phase-locked f_{CEO} estimated from the frequency counting measurement for the mml pump (red squares) and sml pump (blue triangles) cases. (spectrum of the recorded beatnote for mml pump shown in the inset).

have been observed with 40 dB S/N in 300-kHz bandwidth (Fig. 4.7a inset). The electronic signal is first filtered by low-pass filter (200 MHz). Then it is amplified a tunable narrow band-pass amplifier (typically we adjust a frequency of the beat note at $\sim$ 120 MHz) in two stages. The exit from the last bandpass filter is divided in two. The output two is sent to PFD2. Like in the case of the f_{CEO} stabilization loop, a signal from the DDS generator is sent to a second channel of PFD2. A signal from it goes to a PID2 and than actuates the laser cavity slow and fast PZTs in order to control laser length, i.e. the f_{rep} and f_{b698}.

The f_{rep} counting electronics is shown in the Fig. 4.4b. The signal is detected by the same detector that is used for the f_{CEO} detection. A signal from the exit 2 from the splitter is sent to a band pass filter tuned for $\sim$ 294.5 MHz and than is mixed with generator (Osc2) locked to the local oscillator in order to decrease a counted frequency. From an IF mixer output a signal $\sim$ 1 MHz is filtered by low pass filter and is sent to a counter.

The phase noise of the f_{b698} stabilization is shown in Fig. 4.7b. The bandwidth of the stabilization is $\sim$40 kHz. Fig. 4.7a shows the Allan deviation of the f_{b698} frequency counting. The frequency deviations of the f_{rep} was about $\sim$ 1 mHz (1 s) and $\sim$ 150 μHz (100 s).

4.3 OFC stabilization results discussion

4.3.1 Calculated frequency noise of different teeth of the stabilized OFC

To measure the frequency stability of a frequency comb one might perform tests at different wavelengths by employing several different stabilized laser sources. Since this represents an experimental challenge due to the availability of high stability laser sources, here we use a method to give an estimation of the frequency stability across the OFC through the analysis of in-loop servo signals used for the stabilization and of the beatnote signals with the optical reference.

The estimation is based on in-loop measurements of the frequency noise of f_{rep} and f_{CEO} locked signals, which give us the intracavity noise contributions the comb mode n. When n_{ref}-th comb tooth at frequency ν_{nref} is locked to an optical reference ν_{ref}, the n-th comb mode frequency noise is given by [96]:

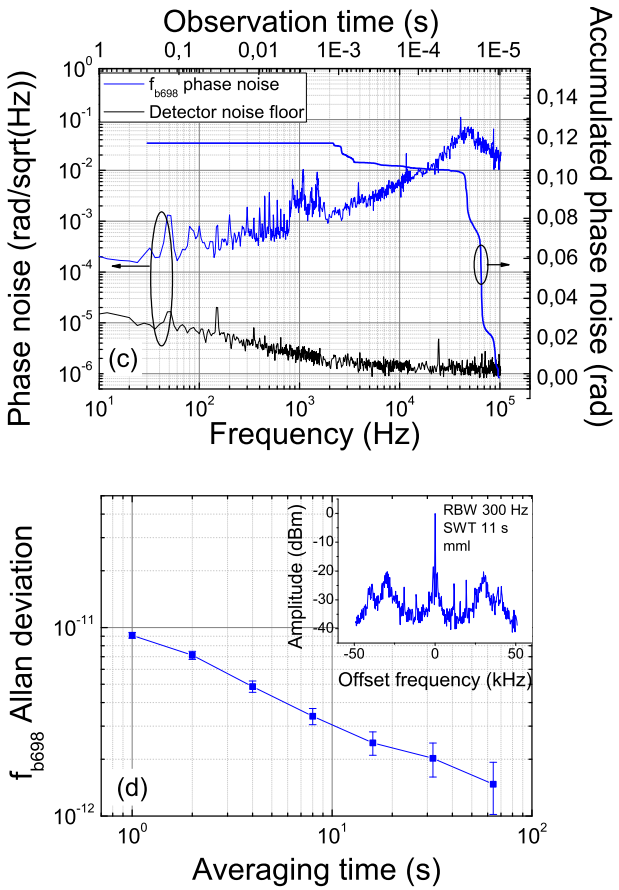

Figure 4.7: The noise spectral densities and the relative estimated Allan deviations of the phase-locked f_{b698} (a),(b). (a) The measured phase noise of the stabilized f_{b698} (blue), phase and frequency detector noise floor (black). Blue line shows the accumulated phase noise. Ellipses and arrows indicates to which vertical scale the curves are referred. (b) The Allan deviation for the f_{b698} estimated from the frequency counting measurement (the recorded beatnote spectrum is shown in the inset).

$$S_{\nu_n} = \left(\frac{n}{n_{ref}}\right)^2 S_{\nu nref} + (1 - n/n_{ref} f_{rep})^2 S_{CEO} + 2\xi n/n_{ref}(1 - n/n_{ref})\sqrt{S_{\nu nref} S_{CEO}} \tag{4.5}$$

where we have neglected the cross correlation term χ between the f_{CEO} noise

and f_{rep} noise, because all fixed points lies in a frequency range between of f_{CEO} and ν_{nref}, the cross- correlation term is always less than zero [96]. Thereby, Eq. (4.5) a reasonable upper limit to the residual frequency noise on the OFC teeth $\chi = 0$.

For our OFC, spanned in $\sim 500 - 1100$ nm region and the optical reference at 698 nm the ratio n/n_{ref} lies in $0.63 - 1.45$ range. Corresponding relative contribution of the f_{b698} frequency noise and f_{CEO} to a OFC tooth for our case is presented in Fig. 4.8. Here the shadow region shows bounds of the OFC. Black curve shows coefficients n/n_{ref} for S_{nref} and $1 - n/n_{ref}$ for S_{CEO}. From this graph it is clear that across all the OFC, the frequency stability of a OFC tooth determines mainly by the frequency stability of the f_{b698}. The frequency noise of f_{CEO} caused by the pump laser amplitude noise. For this reason, an impact of the amplitude noise from a pump laser through f_{CEO} on a frequency stability of a OFC tooth is negligible compared the cavity length fluctuations. However, because fixed points values for the amplitude noise, the noise of the pump laser has a strong direct impact on any OFC tooth stability. The only way to reduce this impact is to reduce the intracavity dispersion (that should change the fixed point value).

The supposition, that the S_{CEO} impact on the S_{ν_n} is negligible to compare with $S_{\nu nref}$, is true when $S_{CEO} \leq S_{\nu nref}$. On the left side of the Fig. 4.9 shows the frequency noise of the f_{CEO} (with the sml and the mml pump) and f_{b698} locks (only for the mml pump) recalculated from phase noise measurements (Fig. 4.6a and Fig. 4.7). The graph shows that $S_{CEO} < S_{\nu nref}$ in our case. In the right side of the Fig. 4.9 shown the frequency noise of different teeth of our EB OFC phase-locked to the clock laser.

So, the type of the pump laser (sml or mml) is not playing a critical role for the OFC freuency stability in our case.

The stability of OFC from results presented in Fig. 4.7 and Fig. 4.6 will give us an Allan deviation $\sigma(a) \approx 10^{-12}$. In the next Chapter 5 will be shown, that this value is due to the limit of our RF reference (Fig. 4.5) and the EB OFC frequency stability measurement relatively the optical reference, that operates at 689 nm, can improve this value (see Sect. 5.2). Unfortunately, our second optical reference give us a quite broad linewidth (> 1 kHz) that very far from our clock laser stability. In this situations we don't have any experimental way to prove a stability of our OFC.

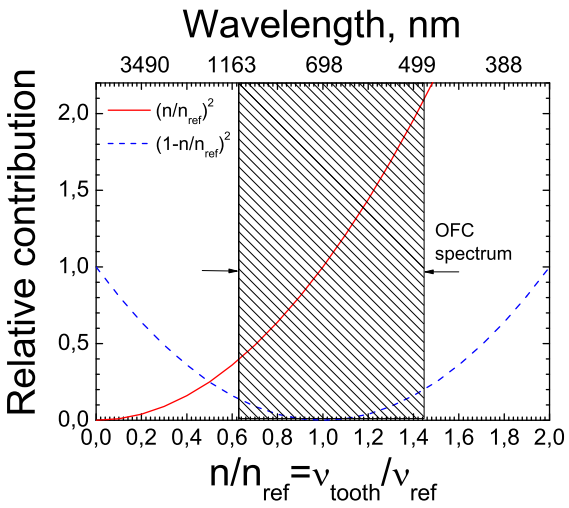

Figure 4.8: Relative contributions of the frequency noise of the f_{CEO} and the f_{b698} to a certain OFC tooth. Here two vertical lines shows bounds of the OFC. The black curve shows coefficient $(n/n_{ref})^2$ for S_{nref} and the green one a coefficient $(1 - n/n_{ref})^2$ for S_{CEO}.

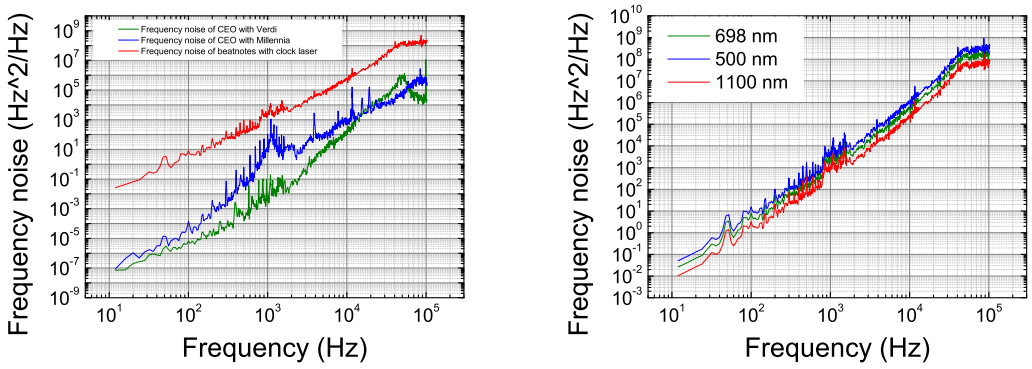

(a) (b)

Figure 4.9: Left:Frequency noise of the stabilized f_{CEO} (middle blue is mml, lowest green is sml case) and f_{b698} (upper red curve) signals. Right: Frequency noise of different teeth of our EB OFC phase-locked to the clock laser.

The only way in this case is to estimate a stability from the related measurements. Using the frequency noise measurements in Fig. 4.7, 4.6 and Eq. (4.5) we

calculated an Allan deviation for different integrated times across the OFC. For the 125 ms integration time is $\sim 5.2\times10^{-14}\pm4.5\times10^{-14}$. This value is coincidence with $\sim 1.15\times10^{-14}\pm1.4\times10^{-16}$ value for 130 ms integration time for the clock laser relative frequency stability measured in [169].

4.4 Stabilization of QOS OFC

4.4.1 Fixed points for QOS OFC

As for OFC with GTI mirror, we measured the fixed points for QOS OFC. For cavity length fluctuations fixed point is $\sim$ 1.47 THz, for pump beam position fluctuations $\sim$ 98 THz, pump power amplitude noise $\sim$ 98 THz. The fixed points of QOS OFC are not changed their values significantly to compare with corresponded values for OFC.

4.4.2 QOS OFC stabilization results

On the Fig. 4.10 are presented results of the frequency counting of the f_{b698} and the f_{rep} signals. Note, that the QOS OFC was phase locked to the clock laser, while f_{CEO} was not stabilized on presented data.

The phase noise of the locked f_{CEO} and of the f_{b698} signals are shown in Fig. 4.11. The noise level at the same level with the case of EB OFC (see Fig. 4.6 and 4.7). However, both locks are more long-term stable compared with EB OFC that give us a possibility to measure their phase noise up to 100 s and 10 s for f_{CEO} and for the f_{b698} correspondingly. In spite of these stabilization results are very preliminary, this long-term stability improvement is important result for any frequency measurement.

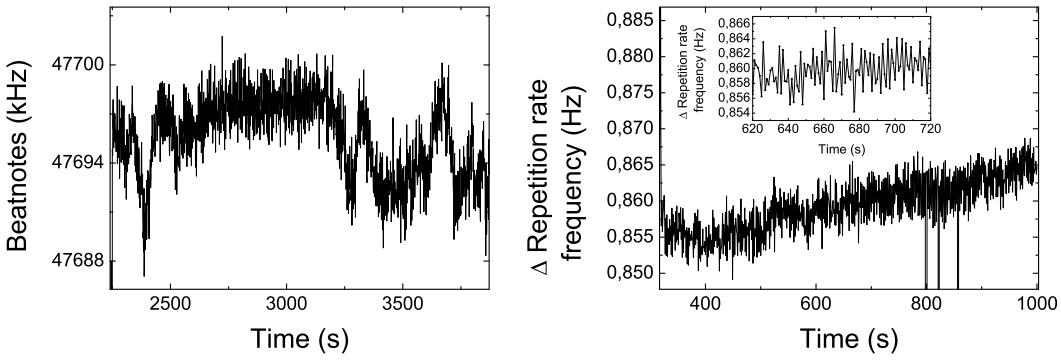

(a) (b)

Figure 4.10: Frequency counting of f_{b698} (Left) and f_{rep} (Right) signals of phase-locked QOS OFC to the clock laser.

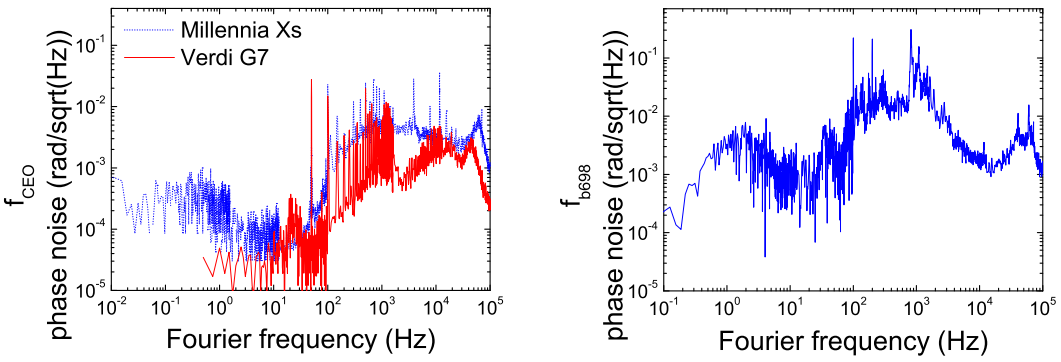

(a) (b)

Figure 4.11: f_{CEO} (a) and f_{b698} (b) phase noise of phase-locked QOS OFC.

Table 4.1: Values used in calculations

Symbol	Quantity	Value	Notes
f_{rep}	Repetition rate frequency	294.5 MHz	-
h	Planck constant	6.62×10^{-34}	
ν_c	Carrier frequency	375 THz	-
P_{out}	Average output power	700 mW	-
θ	Spontaneous emission factor	2	-
l_{tot}	Cavity losses (including the loss at the output coupler)	5	-
T_{oc}	Transmission of output coupler	0.03	-
T_{rt}	Round trip time	3.4 ns	$1/f_r$
E_p	Energy in pulse	2.377×10^{-9}	P_{out}/f_{rep}
P_p	Pump power	4.83 W	
	Sensitivity of rep rate per 1 W pump power change	69.4 Hz	
	Roll-off frequency	5 MHz	
RIN_V	Approximation of Verdi ampl noise	$5 \times 10^{(-7)}/f^{(-1,5)}$	Fig. 4.1.6
RIN_M	Approximation of Millennia ampl noise	$2 \times 10^{(-10)}/f^{(-0,6)}$	Fig. 4.1.6
f_{CEO}	Offset frequency (measured)	75 MHz	
n_{sp}	Effective spontaneous emission factor averaged over the length of the cavity	2	
$\Delta\lambda$	Width of fs spectrum	15 nm	
λ	Central wavelength	800 nm	
t_{rms}	Pulse duration	60 fs	
β_2	Net cavity dispersion	400 fs^2	
D_g	Gain dispersion (gain coefficient $\alpha(\omega)$)	10	[74]
q_{eff}	Quantum efficiency	0.8	
G	Overall gain	5.143	$\frac{P_{pump}}{P_{out}} q_{eff} \frac{\lambda_{eff}}{\lambda_c}$

Table 4.2: Fixed Point, Frequency Dependence, and Magnitude of the Various Contributions to the Frequency Noise on the Comb Lines

Noise Term	Fixed Point	Frequency Dependence	Magnitude at f=1Hz $s^X_{rep}(f)$ in Units of 1/Hz
Environmental (length)	~ 2.5 THz	f^{-1} f^{-1}	$\sim 3.5 \times 10^{-27}$ $\sim 1 \times 10^{-20}$
Pump noise	~ 147 THz	f^{-2} - sml f^{-1} - mml	1.3×10^{-17} - sml 1.3×10^{-21} - mml
Schawlow-Townes limit	NA	f^0	$\sim 10^{-4}$
Intracavity ASE (quantum limit)	~ 375 THz	f^0	5.6×10^{-28}
Supercontinuum and shot noise	NA	f^2	-

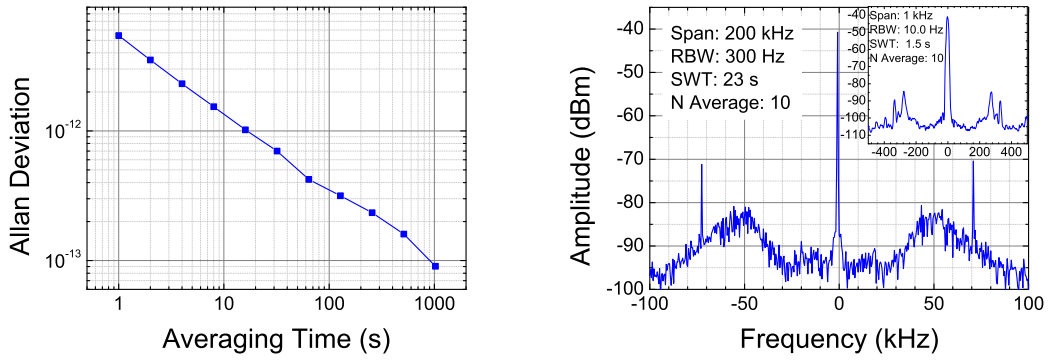

(a) (b)

Figure 4.12: (a) Allan deviation of the f_{CEO} of the QOS OFC pumped by Verdi G7. (b) - Locked f_{CEO} signal. In the inset span 1 kHz, the f_{CEO} resolution bandwidth is limited by the spectrum analyzer.

Chapter 5

OFC applications

In this chapter are presented several applications of the OFC: the absolute frequency measurement of the clock laser (Sect. 5.1), optical to optical ratio between the clock laser and 689 nm laser locked to the atomic resonance by OFC (Sect. 5.2) and the absolute frequency measurement of an unstable laser (Sect. 5.3), which was used in our case for precision measurement of gravity.

The optical frequency reference, used to stabilize the OFC, is always a 698 nm semiconductor laser source (Fig. 5.1a) employed in high resolution spectroscopy of the doubly forbidden $^1S_0$-$^3P_0$ clock transition in atomic strontium (Fig. 5.1b). A second semiconductor laser at 689 nm, resonant with the $^1S_0$-$^3P_1$ intercombination transition in atomic strontium, has also been employed to perform preliminary optical frequency comparisons with the stabilized OFC [188](Fig. 5.1b) (see details in App. C.1, [169] and in [187]). The locked 689 nm laser shows a typical fast linewidth of the order of 1 kHz after the propagation in a 200 m fiber when the PNC technique was not activated [169].

As shown in Fig. 5.1 the stabilized laser sources, the OFC and the strontium cold atom source are located in two separated laboratories, placed in two different buildings within the same University campus, respectively at Dipartimento di Fisica ed Astronomia (UNIFI) and at European Laboratory for Non-Linear Spectroscopy (LENS). The light from the stabilized laser is then transferred between the two labs through the 200 m fiber link [169].

In Fig. 5.1 the experimental apparatus with details on the electronic devices used for the stabilization of both f_{rep} and f_{CEO} are also presented. All the beat-

notes are detected with fast (300 MHz bandwidth) Si photodetectors. The signals are then amplified (typically 50 dB) and properly filtered with tunable RF cavity filters and finally sent to the frequency counters and the locking electronics. For phase-locking the signals, digital phase and frequency detectors (PFD) are employed. The RF signal is produced by a direct digital synthesizer, referenced to a 10 MHz high quality quartz (Oscilloquartz BVA) slaved to a Rb atomic clock and to a GPS receiver, and sent to the PFDs first channels. For the f_{rep} stabilization the f_{b698} signal is sent to the second channel of corresponding PFD. The error signal from the PFD is processed by a proportional-integral-derivative (PID) amplifier, split in two channels and sent respectively to the "slow" and "fast" PZTs acting on the two cavity mirrors. For the f_{CEO} stabilization slow drifts are corrected through a PZT that changes the position of the pump mirror [198], while fast fluctuations (up to 100 kHz) are corrected by changing the pump power with an acousto-optical modulator (AOM).

5.1 Frequency measurements of the clock laser locked to an ULE cavity

5.1.1 Absolute frequency measurement of the clock laser locked to an ULE cavity

To test the frequency stability and to demonstrate the feasibility of optical frequency measurements of the OFC, we measured the absolute optical frequency of a ultra-stable clock laser at 698 nm. At the same moment the OFC was locked to this clock laser. The scheme of the f_{b698}, that was presented in a previous chapter, is the same for the frequency measurement of the absolute frequency of the clock laser.

An absolute optical frequency can be determined by [39, 44]

$$f_{opt} = f_{comb} \pm f_{beat} \tag{5.1}$$

Thus, for a OFC referred to a microwave standard we have:

$$f_{opt} = n f_{rep} \pm f_{CEO} \pm f_{beat} \tag{5.2}$$

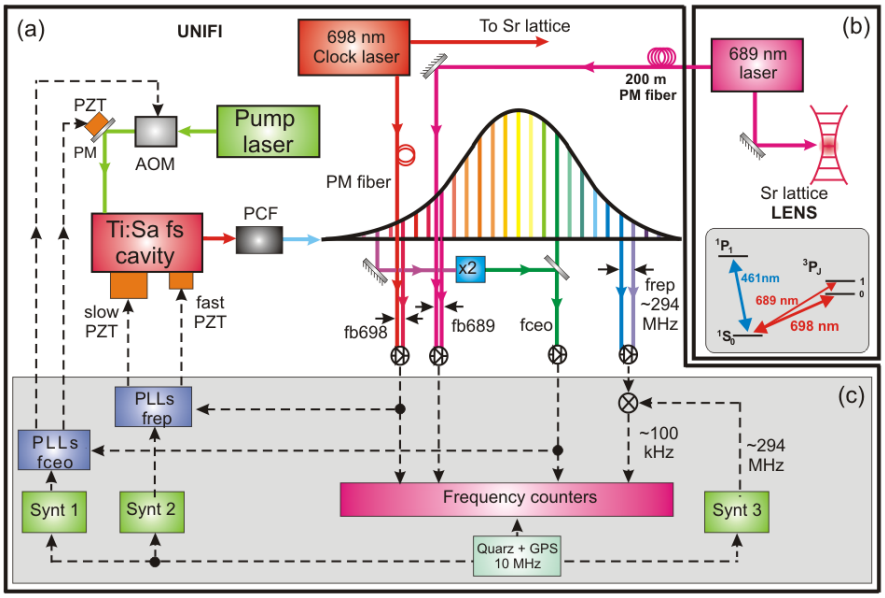

Figure 5.1: Schematic view of the experimental apparatus (a) with details on the electronics employed for stabilization of the OFC (c). Two frequency stabilized lasers respectively at 698 nm (resonant with strontium clock transition $^1S_0$-$^3P_0$)and 689 nm ((b) stabilized on the strontium second stage cooling transition $^1S_0$-$^3P_1$) are employed for the frequency stabilization of the OFC and for optical frequency ratio measurement. PM fiber - polarization-maintaining optical fiber, PCF - photonic crystal fiber, PLL - phase-locked loop, Synt - synthesizer, AOM - acousto-optical modulator, PM - pump mirror.

where the integer n can be solved by using a calibrated wavemeter with resolution better than $f_{rep}/2$. The signs in the equation can be determined by observing the variation of the f_{b698} while increasing the f_{CEO} and f_{rep} (see rules in Tab. 5.1).

The frequency, determined by our WaveMaster Wavelength Meter from Coherent (it's resolution is 100 MHz $< f_{rep}/2 = 147$ MHz), was $f_\lambda = 429\,286.3$ GHz. The f_{rep} of the stabilized OFC measured during 3000 seconds was 294 442 158.016 $\pm$ 0.062 Hz without linear drift removing (see Fig. 5.2a). The f_{CEO} was equal to $f_{CEO} = 32.723 \pm 2$ MHz without linear drift removing (see Fig. 5.2b). For these values the corresponding OFC tooth number n is equal to 1457965. The f_{b698}, measured during the same time period, was $f_{b698} = 181.104\,740$ MHz$\pm$1

kHz (see Fig. 5.3a). By putting this values into the Eq. (5.2) and using rules of Tab. 5.1 we had calculate the absolute frequency of the clock laser $f_{clock\ absolute}$ = 429 286 509 296kHz±20 kHz. Fig. 5.3b shows the Allan deviation of the measured optical frequency. The red curve stands for the f_{b698}. For the comparison, the local reference frequency stability is shown by black line (see Fig. fig:TorinoStand). The Allan deviation of the optical frequency measurement starts from 3×10^{-12} at 1 s averaging time and drops as $\tau^{-0.5}$ up to 10 s. Starts from 20 s it's rising as $\tau^{0.5}$. In the time region $\sim 40- \sim 100$ s a stability of our OFC is reaching a stability of our microwave standard. In the inset shown the clock laser absolute frequency counting where a linear drift of a value 1.258 kHz was removed.

Table 5.1: Rules for choosing sign of f_{CEO} and f_{rep} frequencies

$f_{rep} \uparrow$ **and** $f_b \uparrow$ $\Rightarrow f_b < 0$		$f_{rep} \uparrow$ **and** $f_b \downarrow$ $\Rightarrow f_b > 0$	
$f_{CEO} \uparrow$ and $f_b \uparrow$ $\Rightarrow f_{CEO} > 0$	$f_{CEO} \uparrow$ and $f_b \downarrow$ $\Rightarrow f_{CEO} < 0$	$f_{CEO} \uparrow$ and $f_b \uparrow$ $\Rightarrow f_{CEO} < 0$	$f_{CEO} \uparrow$ and $f_b \downarrow$ $\Rightarrow f_{CEO} > 0$

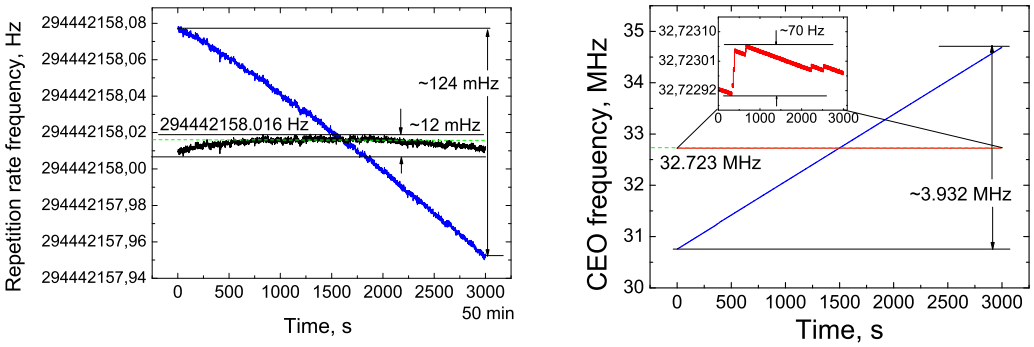

(a) (b)

Figure 5.2: (a) The f_{rep} measurement. (b) The f_{CEO} frequency measurement.

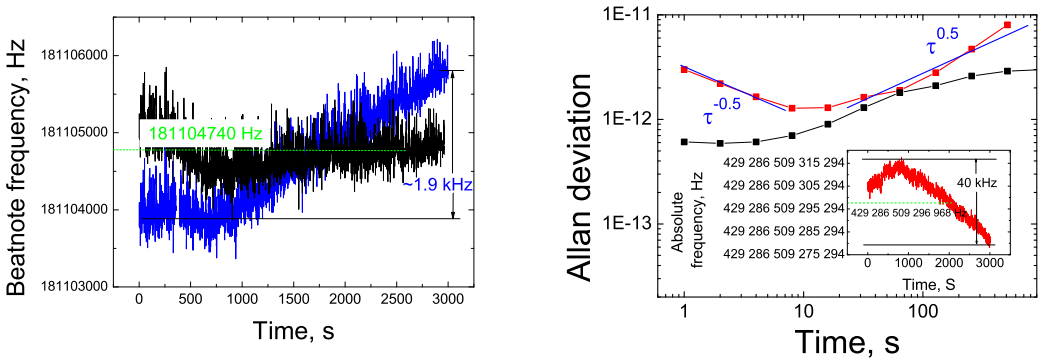

(a) (b)

Figure 5.3: (a) The f_{b698} frequency measurement. (b) The calculated Allan Deviation.

5.1.2 Calibration of the clock laser frequency by the OFC

The 698 nm clock laser can be locked to the several ULE cavity modes and its stability will be at the same level. However, in order to match the clock laser frequency and the atomic clock transition, the clock laser should be locked always to the ULE cavity mode. The frequency gap between the locked clock laser and the atomic clock transition can be hundreds of megahertz. This is not a problem, because this frequency gap can be reduced by AOMs, placed in the frequency shifter configuration to shift the clock laser frequency. The AOMs also are necessary, to tune the clock laser frequency and to reduce parasitic back reflections.

Once the clock laser frequency matched with the atomic transition, the cavity mode and all AOM frequency are calibrated and the "true" frequency of the clock laser can be found in day by day operation. However, the problem is to find the first time the right ULE cavity mode and AOMs frequencies.

Here I will describe the procedure that we did for the frequency calibration of our clock laser by the OFC.

Comparing with the SbSect. 5.1.1, the OFC was operated in quasi-octave spanning regime (see Sect. 3.2) and pumped by the Verdi G7 (see App. 3.1.3).

Due to the fact, that the OFC f_{rep} is around 300 MHz, the wavemeter precision should be better than ±100 MHz. As we experimentally found, the our WaveMaster Wavelength Meter from Coherent can give a larger error than ±100 MHz. For

this reason we used a wavemeter based on a Michelson interferometer and referenced to unstabilized HeNe laser from University of Hannover (see App. E), which can reach the relative accuracy 10^{-7}.

The absolute value measured by the HeNe wavemeter can be different from day to day due to, for example, its alignment. To calibrate it, we always measured the 689 nm laser locked to the ^{88}Sr atomic transition (see SbSec. C.1).

The measured wavelength ratio $\lambda_{input}/\lambda_{reference}$ for the 689 nm laser is $r_{689} = 1.0891926$ (the index of refraction $n_{689} = 1.000263957$ at T= 27.6∘C, humidity = 27%). Note that the 689 nm frequency send to the clean room from the LENS (see Fig. 5.1) is shifted from atomic resonance $f_{689} = 434829121311000$ Hz by two AOMs $\text{AOMoffset}_{689} = (83.739 + 80.626) * 10^6 = 164.365$ MHz.

The clock frequency is shifted by two AOMs: one is a double pass frequency shift $+200.863 \times 2 = 401.726$ MHz and another is a single pass shift +70.256 MHz (in the Fig. 3.19 both AOMs are in PNC system). When the frequency value of the locked to the ULE cavity clock laser is approximately 429227.4 ± 0.3 GHz (measured by the Coherent wavelength meter before the slave laser in Fig. 3.19), the ratio $\lambda_{698}/\lambda_{reference} = r_{698} = 1.1034096 \pm 1 \times 10^{-7}$ ($n_{698} = 1.000263875 \pm 1 \times 10^{-7}$). The clock laser frequency, measured by the HeNe wavemeter, is $f_{clock}^{HeNe} = (f_{689} + \text{AOMoffset}_{689}) \times \frac{r_{689}}{r_{698}} \left(\frac{n_{689}}{n_{698}}\right)^{-1} = 429228.1 \pm 0.1$ GHz. This value ~ 1.4 GHz far from the ^{88}Sr atomic clock transition and approximately is equal to the ULE cavity free-spectral range $f_{fsr} = 1.5$ GHz.

After the locking the lock laser to the proper ULE cavity mode, measuring the clock laser frequency with the OFC and the adjusting the double pass AOM frequency ($+215 \times 2 = 430$ MHz), we get, for the moment, a final result. The measurement with the HeNe wavemeter: $r_{689} = 1.0891928 \pm 1 \times 10^{-7}$, $r_{698} = 1.1034060 \pm 1 \times 10^{-7}$ ($n_{689} = 1.000263957$, $n_{698} = 1.000263875$ for T = 28.8∘ C, humidity = 28%). $f_{clock}^{HeNe} = 429227.73 \pm 0.1$ GHz.

The frequency measurement of the clock laser by the OFC locked to the it, give us $f_{rep} = 294.5193547 \pm 1 \times 10^{-7}$ MHz, $f_{CEO} = +71.2 \times 10^6$ Hz; $f_b = -10.7 \times 10^6$ Hz. These results in $f_{clock}^{OFC} = 429228.2 \pm 1.46 \times 10^{-3}$ GHz and this is ~ 83.038 MHz far from the resonance. This frequency gap we plan to fill up by adding a 70-80 MHz AOM before atoms to tune clock laser frequency.

5.2 OFC frequency stability in the the radio-frequency and in the optical region

The accuracy of frequency measurements are finally limited by the frequency instability of the time-base RF reference standard. In our case this is the stability of a Quartz with very high spectral purity served at long-term region to GPS signal (Fig. 5.1c) with the *declared* value 6×10^{-13} at 1 s.

An accurate measurement can be made by the measurement of optical frequency ratios (see, for example, [103]). We tested our apparatus by making through the OFC a comparison of frequency stability between the 698 nm clock laser and 689 nm laser. Because our OFC, as was shown in previous section, is stabilized to the clock laser, we had achieve a real comparison of OFC stability frequency relatively 689 nm laser stabilized to ^{88}Sr $^1S_0$-$^3P_1$ transition. This frequency stability measurement we compared with OFC stability measurement relatively RF standard.

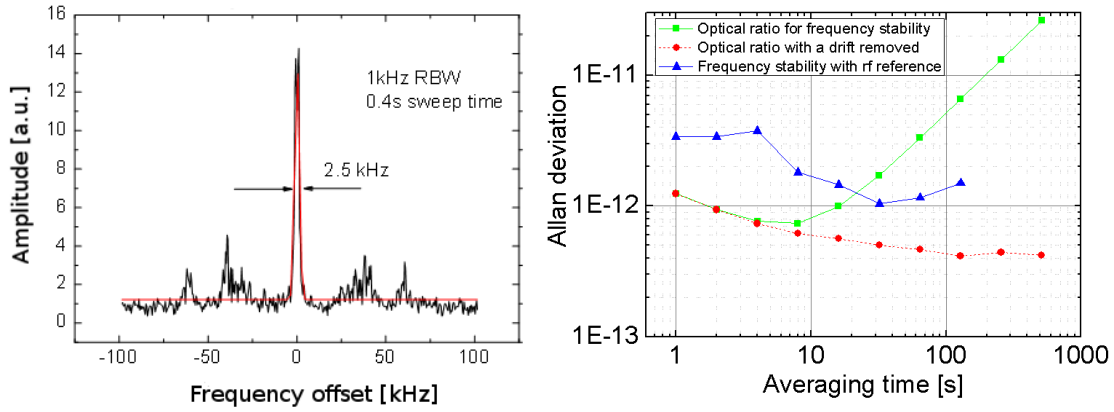

(a) (b)

Figure 5.4: (a) Beat-notes between the OFC and 689 nm laser. (b) - Allan deviation of the OFC against RF reference (blue curve) and of the optical ratio (green curve) with linear cavity drift removed (red curve).

For the optical frequency ratio measurements the light from 689 nm laser is transferred over 200 m fiber link to the OFC lab Fig. 5.1 (in this measurement we have not yet activate the fiber phase noise compensation). This signal was beaten with corresponded part of the OFC light after the PCF. In this condition

the typical observed linewidth with the stabilized OFC is of the order of several hundred Hz - several kHz (Fig. 5.4a). This value we believe to be limited by the 689 laser and not by the stabilized OFC.

In Fig. 5.4b we present the Allan deviation plot of the stability of the OFC relatively to the 689 nm laser (green curve) and the RF local oscillator (blue curve). In the short-term region the stability of the OFC is limited by the linewidth of 689 nm laser. Starting approximately from 10 s the stability of the OFC is limited by the reference high finesse cavity temperature drift that results in a frequency drift of the clock laser and finally in the frequency instability of the fs OFC. Comparing this result with the OFC frequency stability measurement relatively RF local oscillator the optical-optical ratio gives better result up to 20 s integration time. Further, linear frequency drift must be take into account and removed from the data measurement. In this case, we obtain the red curve, which gives a stability at $\sigma_y = 3 \times 10^{-13}$ level after 100 s integration time.

5.3 Absolute frequency measurement of unstable lasers with the OFC

5.3.1 Introduction

In this section, we report the implementation of our Ti:Sa fs OFC for the characterization of the frequency stability of a commercial single-mode high power frequency doubled Nd-YVO laser (Verdi V5 Coherent). This laser has found a wide application as a low noise pump for solid-state Ti:Sa lasers and is often employed in atomic physics experiments as a high power source for dipole trap. This laser is generally characterized by a low AM noise, but can show a quite large frequency jitter (> 50 MHz) both in short term (< 1 ms) and in long term (> 10 s) [199].

Here we demonstrate how an OFC can be used to measure simultaneously the absolute frequency jitter at different temporal scales, showing how these device can find application also to perform precise absolute frequency characterization of unstable lasers.

These measurements are of particular interest in the field of atomic physics in which high power CW solid state laser are typically employed to trap cold atoms in

far off-resonance optical dipole traps with different geometries, ranging from single beam trap, crossed beam traps or multidimensional optical lattices. Especially in the last case, information about frequency jitter is important, since in this kind of trap laser frequency noise may convert in position fluctuations of the trap wells, resulting in additional atom losses.

Here the absolute calibration of Verdi laser emission frequency have been used to improve the accuracy of the measurements of the local gravitational acceleration value by the use of ^{88}Sr ultra-cold atoms trapped in 1D vertical realized with radiation from Verdi laser.

5.3.2 Experimental Setup

As was mentioned in SbSec. C.1 the wavelength of the light λ_L emitted by the Verdi laser is used for for precision measurement of gravity through the observation of Bloch oscillation of trapped atoms by using the Eq. D.1. To obtain absolute frequency measurements of Verdi, part of its radiation is then sent through a 200 m single-mode fiber to the laboratory where is operating the fs OFC (see Fig. D.1).

In the case of direct stabilization in the optical domain the frequency stability of the optical standard will transfer to all OFC components, and the frequency noise on the f_{rep} signal is reduced by a factor n: $f_{rep} = (f_V \pm f_{CEO} \pm f_b)/n$, where f_V is the Verdi frequency, f_{CEO} is the f_{CEO}, f_b is the beanotes between the OFC tooth and the optical standard and n is integer defining the OFC tooth with a value of the order of 10^6.

For this experiment, the output radiation from the 200-m transfer is superimposed in a polarization beam-splitter with radiation from the femtosecond OFC (filtered at $\lambda = 532 \pm 5$ nm) and the beat signal with the corresponding tooth is observed on a fast photodetector.

5.3.3 Experimental results

The observed beat-notes with Verdi laser are presented in Fig. 5.5a. The typical fast linewidth is about 10 - 15 MHz broad due to Verdi laser fast frequency jitter on timescale of few ms [200]. Due to the typical low signal to noise observed (< 25 dB on 300 kHz bandwidth) and its fast frequency jitter, it is in general not possible to use standard frequency counters to perform precise frequency measurements.

To overcome this difficulty, we then lock the f_{rep} of the OFC by stabilizing this beat-note to an RF frequency synthesizer.

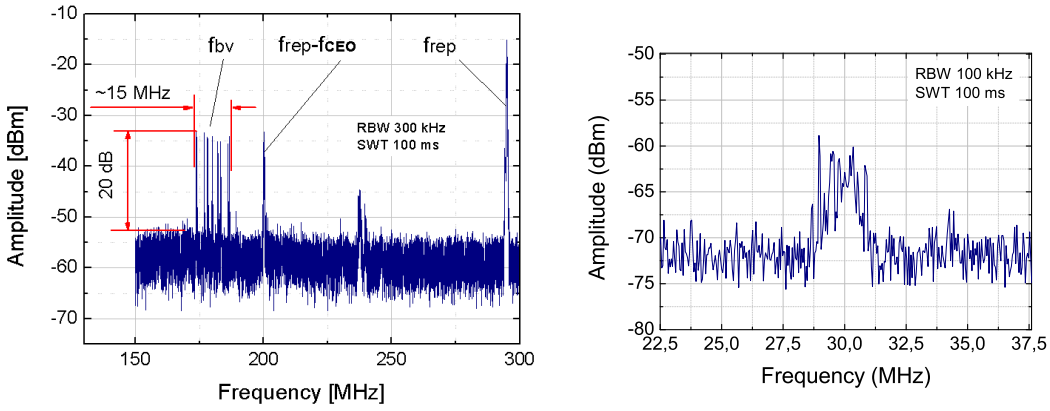

(a) (b)

Figure 5.5: Beat-notes between Verdi and the OFC. (a) free-running beatnotes, (b) locked beat-notes locked regime.

After detection the beatnote signal is amplified, filtered and split in two channels. One channel from RF power splitter is used to monitor the OFC stabilization, while the second one is sent to a phase-frequency detector (PFD).The reference signal for the stabilization (sent to the second PFD input) comes from a local 30 MHz generator referenced at long term to GPS reference signal.

The servo signal for stabilization generated by the PFD (that is proportional to phase difference between the two input signals) is then sent to a PID (proportional-integrated-derivative) controller that is used to actuate two PZT attached to two OFC cavity mirrors for slow and fast (up to 40 kHz) cavity length change.

In lock condition, as shown in Fig. 5.5b, the beat-note signal is stabilized at 30 MHz and the frequency jitter is then imposed on OFC f_{rep}. Thanks to the large demultiplication factor of the OFC ($\sim 1.9 \times 10^6$) the 10 - 15 MHz frequency jitter at 532 nm gets divided down to about 1 Hz and imposed on the f_{rep} signal that is typically observed with S/N> 50 dB over 300 kHz bandwidth. The f_{rep} signal is then counted easily with a frequency counter set with 1 s gate time.

In order to determine the absolute frequency of the Verdi we also count the f_{CEO}. In our setup this signal is sufficiently long term stable compared to Verdi frequency instabilities, so for this measurement a stabilization of this signal was

not required. In this case, the absolute value of the Verdi frequency is given by equation $f = n \times f_{rep} \pm f_{CEO} \pm f_b$. To determine the correct tooth number at the beginning and at the end of each measurement we employ a HeNe wavemeter (App. E), calibrated with a stabilized laser on the 689 nm $^1S_0$-$^3P_1$ ^{88}Sr transition, that allows an evaluation of the Verdi laser frequency with an uncertainty of the order of 100 MHz.

In Fig. 5.6 the result of an absolute frequency measurement that lasts for about 10^4 s is shown. Long term deviation of Verdi frequency greatly depends on many factors, mainly related to temperature, and laser power setting. To increase long term stability we performed this measurement after that of the laser was operating continuously for a long time (about two days) at the same power setting. Moreover, we covered the laser head with a thermal insulation foam to increase the passive temperature stability.

From this measurement we can clearly see periodical deviation of the frequency at two different regimes. Firsts, we observe a long-term oscillation of the Verdi frequency with period ∼1000 s and amplitude 130-140 MHz, secondly there is a fast oscillation with a shorter period ∼33 s and an amplitude 30 - 70 MHz with typical value 30 - 50 MHz (see Fig. 5.6 inset). The missing data in this set are caused to a OFC unlock from the Verdi signal.

We think that this represents a lower limit for long-term frequency fluctuations of unstabilized Verdi laser for the reasons explained above. After shutdown period, these lasers can show in fact both quite different absolute frequency (offset by several GHz) and large frequency drift rate at start up (up to 100 MHz in one minute).

Absolute determinations of Verdi frequency (for the measurement shown in Fig. 5.6 the mean value is 563257825±75 MHz) have been used to determine gravity with 10^{-7} relative uncertainty by observing at the same time Bloch oscillation of ultra-cold ^{88}Sr atoms trapped in vertical standing wave SbSec. C.1.

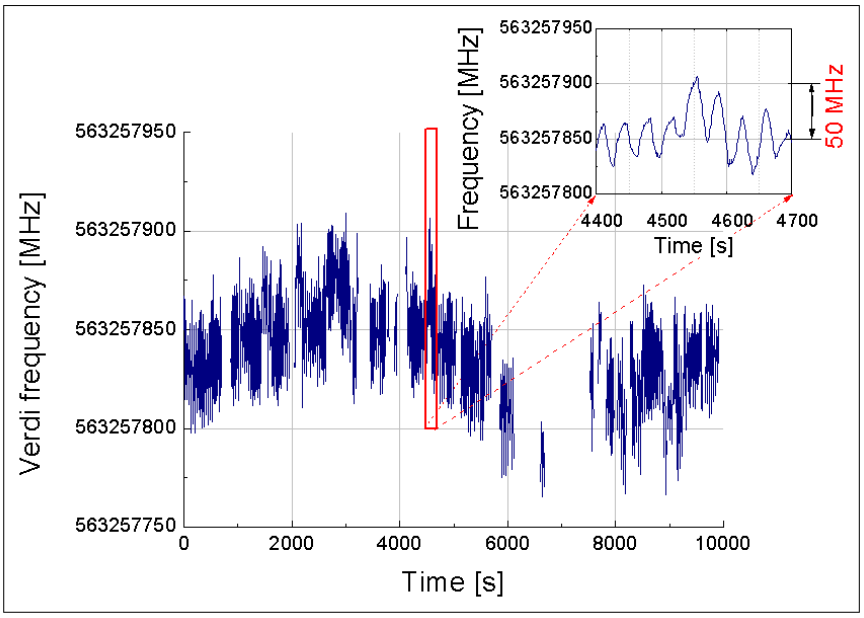

Figure 5.6: Verdi absolute frequency measurement. In the inset are shown the Verdi frequency fluctuations at shorter time scale.

Chapter 6

Conclusions

To conclude we have developed the OFC based on Ti:Sa fs laser stabilized to the clock laser. OFC operates with the high frequency stability (better than $\sigma_y(1s) \approx 4 \times 10^{-12}$) also when it is pumped by mml. At the first step we carefully design the laser cavity and took care about the protection of it from the an environment perturbations. Than the intensity-dependent dynamics and frequency noise of the free-running fs laser were characterized and are used for the optimizations of OFC stabilization PLLs.

OFC f_{rep} was successfully locked to the optical standard. For this we used the two PZT transducers for compensation both the fast noise and a frequency drift in long-term time region. Unfortunately, due to the stability limit of our microwave reference we have not reached desirable stability of our OFC. For this reason, we have tested a OFC stability performance by performing an optical-optical comparison of the stable laser at 689 nm and the clock laser at 698 nm (see SbSect 5.2). The result of this comparison shows that the OFC frequency stability in the case of the optical-optical comparison, is higher that in the case of the optical-RF comparison (Fig. 5.4). This means that the OFC frequency stability is limited by the local RF reference stability. In turn, in the the optical-optical comparison case, OFC frequency stability is limited by the linewidth of the optical reference at 689 nm in short-term and by the thermal cavity drift of the clock laser in a long-term time domain.

To approximate a level of the OFC stability, we studied in details its frequency noise at free-running regime and phase-lock spectrum together with the fixed point

formalism. These results in that the frequency stability of an OFC tooth has the short term stability at level of $\sigma_y(1s) \approx 10^{-14}$ (SbSect. 4.3).

The study of intensity-related dynamics help us to stabilize f_{CEO} both with sml and mml at mHz level (Fig. 4.6). In the QOS regime of the OFC we reached μHz level of f_{CEO} stabilization (Fig. 4.12) with mml.

The OFC was successfully tested in several applications: the clock laser freqwuncy measurements and calibration, optical to optical ratio between the clokc laser and 689 nm laser stabilized to the ^{88}Sr atomic transition and the absolute frequency measurement of the unstable laser. To date, the set up is fully ready to make a frequency measurement with our transportable Sr clock and its frequency comparisons with other optical clocks.

Bibliography

[1] T. H. Maiman. stimulated optical radiation in ruby. *Nature*, 187:493, 1960.

[2] S. N. Bagayev, A. K. Dmitriyev, V. M. Klementyev, M. V. Okhapkin, P. V. Pocasov, B. N. Skvortsov, B. A. Timchenko, and V. F. Zakharyash. Progress towards an optical clock. *Laser Phys.*, 6:612–616, 1996.

[3] D. A. Jennings, K. M. Evenson, and D. J. E. Knight. Optical frequency measurements. *Proc. IEEE*, 74:168, 1986.

[4] C. O. Weiss, G. Kramer, B. Lipphardt, and H. Schnatz. *Topics in Applied Physics: Frequency Measurement and Control Advanced Techniques and Future Trends*. Berlin: Springer, 2000. Optical frequency measurement by conventional frequency multiplication.

[5] T. G. Blaney, N. R. Cross, D. J. E. Knight, G. J. Edwards, and P. R. Pearce. Frequency measurement at 4.25 thz (70.5μm) using a josephson harmonic mixer and phase-lock techniques. *Journal of Physics D: Applied Physics*, 13(8):1365, 1980.

[6] C. Freed. *Tunable Lasers Handbook*. New York: Academic, 1995. CO2 isotope lasers and their application in tunable laser spectroscopy.

[7] C. O. Weiss, G. Kramer, B. Lipphardt, and E. Garcia. Frequency-measurement of a ch_4 hyperfine line at 88-thz optical clock. *IEEE J. Quantum Electron.*, 24:1970, 1988.

[8] A. Clairon, A. Dahmani, B. Filimon, and J. Rutman. Precise frequency measurements of co_2/o_so_4 and hene/ch_4-stabilized lasers. *IEEE Trans. Instrum. Meas.*, 34:265–268, 1985.

[9] F. Nez, M. D. Plimmer, S. Bourzeix, L. Julien, F. Biraben, R. Felder, O. Acef, J. J. Zondy, P. Laurent, A. Clairon, M. Abed, Y. Millerioux, and P. Juncar. Precise frequency measurement of the 2s-8s/8d transtions in atomic hydrogen: New determination of the rydberg constant. *Phys. Rev. Lett.*, 69(16):2326–2329, Oct 1992.

[10] O. Acef, J. J. Zondy, M. Abed, D. G. Rovera, A.H. Gérard, A. Clairon, Ph. Laurent, Y. Millerioux, and P. Juncar. A co_2 to visible optical frequency synthesis chain: accurate measurement of the 473 thz hene/i_2 laser. *Optics Communications*, 97(1-2):29 – 34, 1993.

[11] G. Kramer, B. Lipphardt, and C. O. Weiss. Coherent frequency synthesis in the infrared. *Proc. IEEE Frequency Control Symp.*, pages 39–43, 1992.

[12] Th. Udem, A. Huber, B. Gross, J. Reichert, M. Prevedelli, M. Weitz, and T. W. Hänsch. Phase-coherent measurement of the hydrogen $1S - 2S$ transition frequency with an optical frequency interval divider chain. *Phys. Rev. Lett.*, 79:2646–2649, Oct 1997.

[13] P. S. Ering, D. A. Tyurikov, G. Kramer, and B. Lipphardt. Measurement of the absolute frequency of the methane e-line at 88 thz. *Optics Communications*, 151(4-6):229 – 234, 1998.

[14] A. S. Shelkovnikov, E. V. Kovalchuk, M. A. Gubin, R. Felder, O. Acef, D. G. Rovera, G. Kramer, B. Lipphardt, and S. N. Lea. Absolute frequency measurement, with a set of transportable methane optical frequency standards. In *Proc. Joint Meeting IEEE Int. Frequency Control Symp. and UFFC Conf.*, page 7425, 1999.

[15] O. Acef and et. al. *Accurate frequency measurements and intercomparisons of HeNe/CH_4 (= 3.39 μm), CO_2/OsO_4 (= 10.6 μm) frequency stabilized lasers and a Cs primary standard, Conf. on Precision Electromagnetic Measurements.* Piscataway, NJ: IEEE, Washington, USA, 1998.

[16] M. A. Gubin, D. A. Tyurikov, A. S. Shelkovnikov, E. V. Kovalchuk, G. Kramer, and B. Lipphardt. Transportable hene/ch_4 optical frequency standard and absolute measurements of its frequency. *IEEE J. Quantum Electron.*, 31:2177–2182, 1995.

[17] Y. S. Domnin, N. B. Kosheljaevsky, V. M. Tatarenkov, and P. S. Shumjatsky. Precise frequency measurements in submillimeter and infrared region. *IEEE Trans. Instrum. Meas.*, 29(7):264, 1980.

[18] Y. S. Domnin, L. N. Kopylov, A. N. Malimon, V. P. Tenishev, and P. S. Shumyatskii. Absolute measurements of the frequency of an he-ne/ch_4 standard over a decade. *Sov. J. Quantum Electron.*, 26(4):1081, 1996.

[19] Y. Miki, A. Onae, T. Kurosawa, Y. Akimoto, and E. Sakuma. Frequency chain to 3.39 m ch4-stabilised hene laser using josephson point contact as harmonic mixer. *Japan. J. Appl. Phys.*, 33:1655–8, 1994.

[20] V. P. Chebotayev, V. G. Goldort, V. M. Klementyev, M. V. Nikitin, B. A. Timchenko, and V. F. Zakharyash. Development of an optical time scale. *Applied Physics B: Lasers and Optics*, 29:63–65, 1982. 10.1007/BF00694370.

[21] V. M. Klementev, Y. A. Matyugin, and V. P. Chebotayev. Mixing of the frequencies 88.37 thz (= 3.39 m), 125.13 thz (= 2.39 m), and 260.1 thz (= 1.15 m) in a gas, and production of continuous coherent emission with combined frequency 473.6 thz ($\lambda = 0.63\mu$m). *JETP Lett.*, 24:5–8, 1976.

[22] D. A. Jennings, C. R. Pollock, F. R. Petersen, R. E. Drullinger, K. M. Evenson, J. S. Wells, J.L. Hall, and H.P. Layer. Direct frequency-measurement of the i_2-stabilized hene 473-thz (633-nm) laser. *Opt. Lett.*, 136-8, 1983.

[23] V. P. Chebotayev. Optical time scale. *J. Physique*, C8-505C508-512:42, 1981.

[24] J. Ye, L. S. Ma, and J. L. Hall. Molecular iodine clock. *Phys. Rev. Lett.*, 87(27):270801, Dec 2001.

[25] L. Hollberg, C. W. Oates, G. Wilpers, E. A. Curtis, C. W. Hoyt, S.A. Diddams, A. Bartels, and T.M. Ramond. Optical clocks with cold atoms and stable lasers. In P. Hannaford, editor, *Proc. 16th International Conf. on Laser Spectroscopy 2003*, pages 14–21. Singapore: World Scientific, 2004.

[26] J. C. Bergquist, S. A. Diddams, C. W. Oates, E. A. Curtis, L. Hollberg, R. E. Drullinger, W. M. Itano, D. J. Wineland, and T. Udem. A single $^1 99^h g+$

optical clock. In V. V. Chu and et al, editors, *Proc. 15th International Conf. on Laser Spectroscopy*, pages 106–14. Singapore: World Scientific, 2002.

[27] S. A. Diddams, Th. Udem, J. C. Bergquist, E. A. Curtis, R. E. Drullinger, L. Hollberg, W. M. Itano, W. D. Lee, C. W. Oates, K. R. Vogel, and D. J. Wineland. An Optical Clock Based on a Single Trapped $199Hg^+$ Ion. *Science*, 293(5531):825–828, 2001.

[28] W. H. Oskay and et al. The mercury-ion optical clock and the search for temporal variation of fundamental constants. In *Proc. 2003 Joint Meeting of the IEEE International Frequency Control Symp. and the EFTF Conf.*, page 7881, 2003.

[29] Th. Udem, J. Reichert, R. Holzwarth, and T. W. Hänsch. Accurate measurement of large optical frequency differences with a mode-locked laser. *Opt. Lett.*, 24(13):881–883, 1999.

[30] J. Reichert, R. Holzwarth, Th. Udem, and T. W. Hänsch. Measuring the frequency of light with mode-locked lasers. *Optics Communications*, 172(1-6):59 – 68, 1999.

[31] S. A. Diddams, D. J. Jones, J. Ye, S. T. Cundiff, J. L. Hall, J. K. Ranka, R. S. Windeler, R. Holzwarth, Th. Udem, and T. W. Hänsch. Direct link between microwave and optical frequencies with a 300 thz femtosecond laser comb. *Phys. Rev. Lett.*, 84(22):5102–5105, May 2000.

[32] L. Krainer, R. Paschotta, G. J. Spuhler, I. Klimov, C. Y. Teisset, K. J. Weingarten, and U. Keller. Tunable picosecond pulse-generating laser with a repetition rate exceeding 10 ghz. *Electron. Lett.*, 38:225–227, 2002.

[33] S. C. Zeller, L. Krainer, G. J. Spühler, K. J. Weingarten, R. Paschotta, and U. Keller. Passively mode-locked 40-ghz er:yb:glass laser. *Applied Physics B: Lasers and Optics*, 76:787–788, 2003. 10.1007/s00340-003-1181-z.

[34] D. Huang, E. A. Swanson, C. P. Lin, J. S. Schuman, W. G. Stinson, W. Chang, M.R. Hee, T. Flotte, K. Gregory, C.A. Puliafito, and J.G. Fujimoto. Optical coherence tomography. *Science*, 254(5035):1178–1181, NOV 22 1991.

[35] M. Bellini and T. W. Hänsch. Phase-locked white-light continuum pulses: toward a universal optical frequency-comb synthesizer. *Opt. Lett.*, 25(14):1049–1051, 2000.

[36] S.N. Bagayev, S.V. Chepurov, V.M. Klementyev, S.A. Kuznetsov, V.S. Pivtsov, V.V. Pokasov, and V.F. Zakharyash. A femtosecond self-mode-locked ti:sapphire laser with high stability of pulse-repetition frequency and its applications. *Applied Physics B: Lasers and Optics*, 70:375–378, 2000. 10.1007/s003400050060.

[37] H. R. Telle, G. Steinmeyer, A. E. Dunlop, J. Stenger, Sutter D. H., and U. Keller. Carrier-envelope offset phase control: A novel concept for absolute optical frequency measurement and ultrashort pulse generation. *Applied Physics B Lasers and Optics*, 69:327–, 1999.

[38] J. K. Ranka, R. S. Windeler, and A. J. Stentz. Visible continuum generation in air-silica microstructure optical fibers with anomalous dispersion at 800 nm. *Opt. Lett.*, 25(1):25–27, Jan 2000.

[39] D. J. Jones, S. A. Diddams, J. K. Ranka, A. Stentz, R. S. Windeler, J. L. Hall, and S. T. Cundiff. Carrier-envelope phase control of femtosecond mode-locked lasers and direct optical frequency synthesis. *Science*, 288(5466):635–639, 2000.

[40] U. Morgner, R. Ell, G. Metzler, T. R. Schibli, F. X. Kärtner, J. G. Fujimoto, H. A. Haus, and E. P. Ippen. Nonlinear optics with phase-controlled pulses in the sub-two-cycle regime. *Phys. Rev. Lett.*, 86(24):5462–5465, Jun 2001.

[41] T. M. Fortier, D. J. Jones, and S. T. Cundiff. Phase stabilization of an octave-spanning ti:sapphire laser. *Opt. Lett.*, 28(22):2198–2200, 2003.

[42] A. Bartels. *Femtosecond Optical Frequency Comb: Principle, Operation, and Applications*, chapter 3: Gigahertz femtosecond lasers, pages 78–96. Kluwer Academic Publishers / Springer Norwell, MA, 2005.

[43] A. Yu. Nevsky, R. Holzwarth, J. Reichert, Th. Udem, T. W. Hansch, J. von Zanthier, H. Walther, H. Schnatz, F. Riehle, P.V. Pokasov, M. N. Skvortsov,

and S. N. Bagayev. Frequency comparison and absolute frequency measurement of i2-stabilized lasers at 532 nm. *Optics Communications*, 192(3-6):263 – 272, 2001.

[44] Th. Udem, R. Holzwarth, and T. W. Hänsch. Optical frequency metrology. *Nature*, 416(6877):233–237, March 2002.

[45] K. Takahata, T. Kobayashi, H. Sasada, Y. Nakajima, H. Inaba, and F.-L. Hong. Absolute frequency measurement of sub-doppler molecular lines using a $3.4 - \mu m$ difference-frequency-generation spectrometer and a fiber-based frequency comb. *Phys. Rev. A*, 80(3):032518, Sep 2009.

[46] P. Maddaloni, P. Cancio, and P. De Natale. Optical comb generators for laser frequency measurement. *Measurement Science and Technology*, 20(5):052001, 2009.

[47] T.-A. Liu, R.-H. Shu, and J.-L. Peng. Semi-automatic, octave-spanning optical frequency counter. *Opt. Express*, 16(14):10728–10735, Jul 2008.

[48] P. Del'Haye, O. Arcizet, M. L., Gorodetsky, R. Holzwarth, and Kippenberg T. J. Frequency comb assisted diode laser spectroscopy for measurement of microcavity dispersion. *Nat Photon*, 3(9):529–533, September 2009.

[49] F. R. Giorgetta, I. Coddington, E. Baumann, W. C. Swann, and N. R. Newbury. Fast high-resolution spectroscopy of dynamic continuous-wave laser sources. *Nat Photon*, 4(12):853–857, December 2010.

[50] F. Adler, M. J. Thorpe, K. C. Cossel, and J. Ye. Cavity-enhanced direct frequency comb spectroscopy: technology and applications. *Ann. Rev. Anal. Chem.*, 3:175–205, 2010.

[51] S. A. Diddams, L. Hollberg, and V. Mbele. Molecular fingerprinting with the resolved modes of a femtosecond laser frequency comb. *Nature*, 445(7128):627–630, February 2007.

[52] Ch. Gohle, B. Stein, A. Schliesser, Th. Udem, and Th. W. Hänsch. Frequency comb vernier spectroscopy for broadband, high-resolution, high-sensitivity absorption and dispersion spectra. *Phys. Rev. Lett.*, 99(26):263902, Dec 2007.

[53] N. R. Newbury, P. A. Williams, and W. C. Swann. Coherent transfer of an optical carrier over 251 km. *Opt. Lett.*, 32(21):3056–3058, Nov 2007.

[54] J. Kim, J. A. Cox, J. Chen, and F. X. Kärtner. Drift-free femtosecond timing synchronization of remote optical and microwave sources. *Nat Photon*, 2(12):733–736, December 2008.

[55] A. Bartels, S. A. Diddams, C. W. Oates, G. Wilpers, J. C. Bergquist, W. H. Oskay, and L. Hollberg. Femtosecond-laser-based synthesis of ultrastable microwave signals from optical frequency references. *Opt. Lett.*, 30:667–669, 2005.

[56] S. A. Diddams, M. Kirchner, T. Fortier, D. Braje, A. M. Weiner, and L. Hollberg. Improved signal-to-noise ratio of 10 ghz microwave signals generated with a mode-filtered femtosecond laser frequency comb. *Optics Express*, 17(5):3331–3340, 2009.

[57] T. M. Fortier, M. S. Kirchner, F. Quinlan, J. Taylor, J. C. Bergquist, T. Rosenband, N. Lemke, A. Ludlow, Y. Jiang, C. W. Oates, and S. A. Diddams. Generation of ultrastable microwaves via optical frequency division. (Submitted on 19 Jan 2011 (v1), last revised 29 Apr 2011 (this version, v3)), 2011.

[58] T. Steinmetz, T. Wilken, C. Araujo-Hauck, R. Holzwarth, T.W. Hänsch, L. Pasquini, A. Manescau, S. D'Odorico, M. T. Murphy, Th. Kentischer, W. Schmidt, and Th. Udem. Laser Frequency Combs for Astronomical Observations. *Science*, 321(5894):1335–1337, 2008.

[59] S. G. Karshenboim. Some possibilities for laboratory searches for variations of fundamental constants. *Can. J. Phys.*, 78(7):639–678, 2000.

[60] V. A. Dzuba, V. V. Flambaum, and J. K. Webb. Calculations of the relativistic effects in many-electron atoms and space-time variation of fundamental constants. *Phys. Rev. A*, 59(1):230–237, Jan 1999.

[61] L. E. Hargrove, R. L. Fork, and M. A. Pollack. Locking of hene laser modes induced by synchronous intracavity modulation. *Appl. Phys. Lett.*, 5:4, 1964.

[62] H. W. Mocker and R. J. Collins. Mode competition and self-locking effects in a qswitched ruby laser. *Appl. Phys. Lett.*, 7:270–273, 1965.

[63] A. J. De Maria, D. A. Stetser, and H. Heynau. Self mode-locking of lasers with saturable absorbers. *Appl. Phys. Lett.*, 8:174176, 1966.

[64] C. V. Shank and E. P. Ippen. Subpicosecond kilowatt pulses from a mode-locked cw dye laser. *Appl. Phys. Lett.*, 24:373375, 1974.

[65] I. S. Ruddock and D. J. Bradley. Bandwidth-limited subpicosecond pulse generation in mode-locked cw dye lasers. *Appl. Phys. Lett.*, 29:296–297, 1976.

[66] J. C. Diels, E. W. V. Stryland, and G. Benedict. Generation and measurement of pulses of 0.2 ps duration. *Opt. Commun.*, 25:93, 1978.

[67] R. L. Fork, B. I. Greene, and C. V. Shank. Generation of optical pulses shorter than 0.1 ps by colliding pulse modelocking. *Appl. Phys. Lett.*, 38:617619, 1981.

[68] G. T. Maker and A. I. Ferguson. Frequency-modulation mode locking of diodepumped nd:yag laser. *Opt. Lett.*, 14:788790, 1989.

[69] G. T. Maker and A. I. Ferguson. Frequency-modulation mode-locking and q-switching of diode-laser-pumped nd-ylf laser. *Electron. Lett.*, 25:1025–1026, 1989.

[70] U. Keller, K. D. Li, B. T. Khuri-Yakub, D. M. Bloom, K. J. Weingarten, and D. C. Gerstenberger. High-frequency acousto-optic modelocker for picosecond pulse generation. *Opt. Lett.*, 15:4547, 1990.

[71] K. J. Weingarten, D. C. Shannon, R. W. Wallace, and U. Keller. Two gigahertz repetition rate, diode-pumped, mode locked, nd:yttrium lithium fluoride (ylf) laser. *Opt. Lett.*, 15:962–964, 1990.

[72] T. Juhasz, S. T. Lai, and M. A. Pessot. Efficient short-pulse generation from a diodepumped nd:ylf laser with a piezoelectrically induced diffraction modulator. *Opt. Lett.*, 15:1458–1460, 1990.

[73] D. J. Kuizenga and A. E. Siegman. Fm and am mode locking of the homogeneous laser - part ii: Experimental results in a nd:yag laser with internal fm modulation. *IEEE J. Quantum Electron.*, 6:709–715, 1970.

[74] A. E. Siegman. *Lasers*. University Science Books, Mill Valley, California, 1986.

[75] P. F. Moulton. Spectroscopic and laser characteristics of ti:al_2o_3. *J. Opt. Soc. Am. B*, 3(1):125–133, 1986.

[76] Y. Ishida, N. Sarukura, and H. Nakano. *Ultrafast Phenomena*, PD11:11, 1990. OSA, California,.

[77] D. E. Spence, P. N. Kean, and W. Sibbett. 60-fsec pulse generation from a self-mode-locked ti:sapphire laser. *Opt. Lett.*, 16(1):42–44, 1991.

[78] U. Keller, G. W. 'tHooft, W. H. Knox, and J. E. Cunningham. Femtosecond pulses from a continuously self-starting passively mode-locked ti:sapphire laser. *Opt. Lett.*, 16(13):1022–1024, 1991.

[79] F. Salin, J. Squier, and M. Piché. Mode locking of ti:ai_2o_3 lasers and self-focusing: a gaussian approximation. *Opt. Lett.*, 16(21):1674–1676, 1991.

[80] D. K. Negus, L. Spinelli, N. Goldblatt, and G. Feugnet. *Advanced Solid-State Lasers*. Optical Society of America, Washington D.C., 1991.

[81] T.W. Hänsch. Nobel lecture: Passion for precision. *Rev. Mod. Phys.*, 78(4):1279–1295, Nov 2006.

[82] I. P. Christov, M. M. Murnane, H. C. Kapteyn, J. Zhou, and Ch.-P. Huang. Fourth-order dispersion-limited solitary pulses. *Opt. Lett.*, 19(18):1465–1467, Sep 1994.

[83] R. Szipöcs, K. Ferencz, Ch. Spielmann, and F. Krausz. Chirped multilayer coatings for broadband dispersion control in femtosecond lasers. *Opt. Lett.*, 19(3):201–203, Feb 1994.

[84] D. H. Sutter, G. Steinmeyer, L. Gallmann, N. Matuschek, F. Morier-Genoud, U. Keller, V. Scheuer, G. Angelow, and T. Tschudi. Semiconductor saturable-absorber mirror assisted kerr-lens mode-locked ti:sapphire laser producing pulses in the two-cycle regime. *Opt. Lett.*, 24(9):631–633, May 1999.

[85] D. B. Sullivan, D. W. Allan, D. A. Howe, and F. L. Walls. *NIST technical note 1337: Characterization of clocks and oscillators,*. 1990.

[86] S. T. Cundiff and J. Ye. Colloquium: Femtosecond optical frequency combs. *Rev. Mod. Phys.*, 75(1):325–342, Mar 2003.

[87] R. Loudon. *Quantum Theory of Light*. Clarendon, Oxford, UK, 2000.

[88] A. L. Schawlow and C. H. Townes. Infrared and optical masers. *Phys. Rev.*, 112:1940–1949, 1958.

[89] H. Haus and A. Mecozzi. Noise of mode-locked lasers. *IEEE J. Quantum Electron*, 29:983–996, 1993.

[90] R. Paschotta. Noise of mode-locked lasers (part i): numerical model. *Applied Physics B: Lasers and Optics*, 79:153–162, 2004. 10.1007/s00340-004-1547-x.

[91] R. Paschotta. Noise of mode-locked lasers (part ii): timing jitter and other fluctuations. *Applied Physics B: Lasers and Optics*, 79:163–173, 2004. 10.1007/s00340-004-1548-9.

[92] N. R. Newbury and B. R. Washburn. Theory of the frequency comb output from a femtosecond fiber laser. *IEEE J. Quantum Electron*, QE-41:1388–1402, 2005.

[93] R. Paschotta, A. Schlatter, S. C. Zeller, H. R. Telle, and U. Keller. Optical phase noise and carrier-envelope offset noise of mode-locked lasers. *Appl. Phys. B*, 82:265–273, 2006.

[94] L. Matos, O. D. Mücke, J. Chen, and F. X. Kärtner. Carrier-envelope phase dynamics and noise analysis in octave-spanning ti:sapphire lasers. *Opt. Express*, 14(6):2497–2511, Mar 2006.

[95] M. J. Ablowitz, B. Ilan, and S. T. Cundiff. Noise-induced linewidth in frequency combs. *Opt. Lett.*, 31:1875–1877, 2006.

[96] N. R. Newbury and W. C. Swann. Low-noise fiber-laser frequency combs (invited). *J. Opt. Soc. Am. B*, 24(8):1756–1770, Aug 2007.

[97] J. K. Wahlstrand, J. T. Willits, C. R. Menyuk, and S. T. Cundiff. The quantum-limited comb lineshape of a mode-locked laser: Fundamental limits on frequency uncertainty. *Opt. Express*, 16(23):18624–18630, 2008.

[98] C. R. Menyuk, J. K. Wahlstrand, J. Willits, R. P. Smith, Th. R. Schibli, and S. C. Cundiff. Pulse dynamics in mode-locked lasers: relaxation oscillations and frequency pulling. *Opt. Express*, 15 (11):6677–6689, 2007.

[99] J. K. Wahlstrand, J. T. Willits, T. R. Schibli, C. R. Menyuk, and S. T. Cundiff. Quantitative measurement of timing and phase dynamics in a mode-locked laser. *Opt. Lett.*, 32:3426–3428, 2007.

[100] L.-S. Ma, L. Robertsson M. Zucco R.S. Windeler G. Wilpers C. Oates L. Hollberg Z. Bi, A. Bartels, and S.A. Diddams. Optical frequency synthesis and comparison with uncertainty at the 1019 level. *Science*, 303:1843–1845, 2004.

[101] L.-S. Ma, Z. Bi, A. Bartels, K. Kim, L. Robertsson, M. Zucco, R. S. Windeler, G. Wilpers, C. Oates, L. Hollberg, and S. A. Diddams. Frequency uncertainty for optically referenced femtosecond laser frequency combs. *IEEE J. Quantum Electron.*, 43:139–146, 2007.

[102] A. Bartels, C. W. Oates, L. Hollberg, and S. A. Diddams. Stabilization of femtosecond laser frequency combs with subhertz residual linewidths. *Opt. Lett.*, 29:10811083, 2004.

[103] J. Stenger, H. Schnatz, Ch. Tamm, and Telle. H. R. Ultraprecise measurement of optical frequency ratios. *Physical Review Letters*, 88:73601–, 2002.

[104] T. R. Schibli, D. C. I. Hartl, M. J. Yost, A. Martin, M. E. Marcinkevi, Fermann, and J. Ye. Optical frequency comb with submillihertz linewidth and more than 10 w average power. *Nature Photonics*, 2:355359, 2008.

[105] L. Xu, Ch. Spielmann, A. Poppe, T. Brabec, F. Krausz, and T. W. Hänsch. Route to phase control of ultrashort light pulses. *Opt. Lett.*, 21(24):2008–2010, 1996.

[106] H. A. Haus and E. P. Ippen. Group velocity of solitons. *Opt. Lett.*, 26(21):1654–1656, Nov 2001.

[107] T. M. Fortier, J. Ye, S. T. Cundiff, and R. S. Windeler. Nonlinear phase noise generated in air-silica microstructure fiber and its effect on carrier-envelope phase. *Opt. Lett.*, 27(6):445–447, 2002.

[108] F. W. Helbing, G. Steinmeyer, J. Stenger, H. R. Telle, and U. Keller. Carrier-envelope-offset dynamics and stabilization of femtosecond pulses. *Applied Physics B: Lasers and Optics*, 74:s35–s42, 2002. 10.1007/s00340-002-0898-4.

[109] S. Witte, R. T. Zinkstok, W. Hogervorst, and K. S. E. Eikema. Control and precise measurement of carrier-envelope phase dynamics. *Appl. Phys. B*, 78(1):5–12, 2004.

[110] Y. Chen, F. X. Kärtner, U. Morgner, S. H. Cho, H. A. Haus, E. P. Ippen, and J. G. Fujimoto. Dispersion-managed mode locking. *J. Opt. Soc. Am. B*, 16(11):1999–2004, Nov 1999.

[111] M. J. Ablowitz, B. Ilan, and S. T. Cundiff. Carrier-envelope phase slip of ultrashort dispersion-managed solitons. *Opt. Lett.*, 29(15):1808–1810, Aug 2004.

[112] K. W. Holman, R. J. Jones, A. Marian, S. T. Cundiff, and J. Ye. Intensity-related dynamics of femtosecond frequency combs. *Opt. Lett.*, 28(10):851–853, May 2003.

[113] H. R. Telle, B. Lipphardt, and J. Stenger. kerr-lens mode-locked lasers as transfer oscillators for optical frequency measurements. *Appl. Phys. B*, 74:1, 2002.

[114] N. Haverkamp, H. Hundertmark, C. Fallnich, and H. R. Telle. Frequency stabilization of mode-locked erbium fiber lasers using pump power control. *Applied Physics B: Lasers and Optics*, 78:321–324, 2004. 10.1007/s00340-003-1397-y.

[115] B. R. Washburn, W. C. Swann, and N. R. Newbury. Response dynamics of the frequency comb output from a femtosecond fiber laser. *Opt. Express*, 13(26):10622–10633, 2005.

[116] F. Träger, editor. *Handbook of lasers and optics*. Springer, 2007.

[117] J.-C. Diels and W. Rudolph. *Ultrashort Laser Pulse Phenomena : Fundamentals, Techniques, and Applications on a Femtosecond Timescale*. Academic Press, San Diego, 1996.

[118] L. Mandel and E. Wolf. *Optical Coherence and Quantum Optics*. Cambridge Univ. Press, Cambridge, 1995.

[119] R. Bracewell. *The Fourier Transform and Its Applications*. McGraw-Hill, Singapore, 2000.

[120] A. W. Albrecht, J. D. Hybl, S. M. Gallagher Faeder, and D. M. Jonas. Experimental distinction between phase shifts and time delays: Implications for femtosecond spectroscopy and coherent control of chemical reactions. *J. Chem. Phys.*, 111:10934–10956, 1999.

[121] A. Präkelt, M. Wollenhaupt, C. Sarpe-Tudoran, and T. Baumert. Phase control of a two-photon transition with shaped femtosecond laser-pulse sequences. *Phys. Rev. A*, 70:063407–1–063407–10, 2004.

[122] S. De Silvestri, P. Laporta, and O. Svelto. The role of cavity dispersion in cw mode-locked lasers. *IEEE J. Quant. Electron.*, 20:533–539, 1984.

[123] J. D. McMullen. Chirped-pulse compression in strongly dispersive media. *J. Opt. Soc. Am.*, 67:1575–1578, 1977.

[124] J. C. Diels and W. Rudolph. *Ultrashort Laser Pulse Phenomena*. Academic, San Diego, 1996.

[125] W. Sellmeier. Zur erklärung der abnormen farbenfolge im spectrum einiger substanzen. *Annalen der Physik und Chemie*, 219:272–282, 1871.

[126] I. H. Malitson. Interspecimen comparison of the refractive index of fused silica. *J. Opt. Soc. Am.*, 55(10):1205–1208, Oct 1965.

[127] F. Gires and P. Tournois. Interferometre utilisable pour la compression d'impulsions lumineuses modulees en frequence. *C. R. Acad. Sci. Paris*, 258:6112, 1964.

[128] P. M. W. French. The generation of ultrashort laser pulses. *Rep. Prog. Phys.*, 58:169–267, 1995.

[129] S. A. Akhmanov, V. A. Vysloukh, and A. S. Chirkin. *Optics of Femtosecond Pulses*. American Institute of Physics, New York, 1992.

[130] W. Demtröder. *Laser spectroscopy*. 3ed., Springer, 2003. (T)(K)(600dpi)(1008s)(ISBN 3540652256) PEo.

[131] J. Heppner and J. Kuhl. Intracavity chirp compensation in a colliding pulse mode-locked laser using thinfilm interferometers. *Appl. Phys. Lett.*, 47:453–455, 1985.

[132] N. Matuschek, F.X. Kartner, and U. Keller. Exact coupled mode theories for multilayer interference coatings with arbitrary strong index modulation,. *IEEE J. Quant. Electron.*, 33:295–302, 1997.

[133] N. Matuschek, F.X. Kartner, and U. Keller. Analytical design of double-chirped mirrors with customtailored dispersion characteristics. *IEEE J. Quant. Electron.*, 35:129–137, 1999.

[134] L. G. Cohen and C. Lin. Pulse delay measurements in the zero material dispersion wavelength region for optical fibers. *Appl. Opt.*, 16(12):3136–3139, Dec 1977.

[135] A. Sugimura and K. Daikoku. Wavelength dispersion of optical fibers directly measured by difference method in the 0.8-1.6 μm range. *Rev. Sci. Instrum.*, 50 (3):434, 1979.

[136] N. Seikai S. Tateda, M. Shibata. Interferometric method for chromatic dispersion measurement in a single-mode optical fiber. *IEEE J. Quantum Electron.*, 17 (3):404–407, 1981.

[137] H.-T. Shang. Chromatic dispersion measurement by white-light interferometry on metre-length single-mode optical fibres. *Electron. Lett.*, 17 (17):603, 1981.

[138] Ch. Dorrer. Chromatic dispersion characterization by direct instantaneous frequency measurement. *Opt. Lett.*, 29(2):204–206, Jan 2004.

[139] O. Svelto. *Principles of Lasers*. Springer, Berlin, New York, 4 edition, 1998.

[140] U. Keller. Recent developments in compact ultrafast lasers. *Nature*, 424(6950):831–838, August 2003.

[141] Th. Brabec and F. Krausz. Nonlinear optical pulse propagation in the single-cycle regime. *Phys. Rev. Lett.*, 78(17):3282–3285, Apr 1997.

[142] A. L. Gaeta and R. S. Windeler. *Microstructure fiber and whitelight generation*, chapter 4, pages 97–111. 2005.

[143] J. Ye and S. T. Cundiff. *Femtosecond Optical Frequency Comb Technology: Principle, Operation, and Applications*, chapter Chapter 4: Microstructure fiber and whitelight generation, pages 97–111. Springer, New York, 2005.

[144] T. Kinoshita. The fine structure constant. *Reports on Progress in Physics*, 59(11):1459, 1996.

[145] T. Kinoshita. Improvement of the fine-structure constant obtained from the electron g-2. *IEEE Trans. Instrum. Meas.*, 50:568–571, 2001.

[146] J. M. Hensley. PhD thesis, Stanford University, 2001.

[147] R. E. Ell, U. Morgner, F. X. Kärtner, J. G. Fujimoto, E. P. Ippen, V. Scheuer, G. Angelow, T. Tschudi, M. J. Lederer, A. Boiko, and B. Luther-Davies. Generation of 5 fs pulses and octave spanning spectra directly from a ti:sapphire laser. *Opt. Lett.*, 26:373, 2001.

[148] G. Steinmeyer and U. Keller. *Femtosecond Optical Frequency Comb: Principle, Operation, and Applications*, chapter 5: Optical comb dynamics and stabilization, pages 112–132. Kluwer Academic Publishers / Springer, Norwell, MA, 2005.

[149] Th. Brabec and F. Krausz. Intense few-cycle laser fields: Frontiers of nonlinear optics. *Rev. Mod. Phys.*, 72(2):545–591, Apr 2000.

[150] N. Haverkamp, B. Lipphardt, J. Stenger, H. R. Telle, C. Fallnich, and H. Hundertmark. *Conference On Ultrafast Phenomena*. Vancouver, BC, 2002.

[151] K. W. Holman, R. J. Jones, A. Marian, S. T. Cundiff, and J. Ye. Detailed studies and control of intensity-related dynamics of femtosecond frequency combs from mode-locked ti:sapphire lasers. *IEEE Journal of selected topics in quantum electronics*, 9:4, 2003.

[152] H. A. Haus. Mode-locking of lasers. *IEEE J. Sel. Top. Quantum Electron.*, 6:1173–1185, 2000.

[153] G. P. Agrawal. *Nonlinear Optics*. Academic Press, San Diego, 2001.

[154] H. A. Haus and Y. Lai. Quantum theory of soliton squeezing: a linearized approach. *J. Opt. Soc. Am. B*, 7(3):386–392, Mar 1990.

[155] F. W. Helbing, G. Steinmeyer, U. Keller, R. S. Windeler, J. Stenger, and H. R. Telle. Carrier-envelope offset dynamics of mode-locked lasers. *Opt. Lett.*, 27(3):194–196, Feb 2002.

[156] R. L. Fork, O. E. Martinez, and J. P. Gordon. Negative dispersion using pairs of prisms. *Opt. Lett.*, 9(5):150–152, 1984.

[157] R. E. Sherriff. Analytic expressions for group-delay dispersion and cubic dispersion in arbitrary prism sequences. *J. Opt. Soc. Am. B*, 15(3):1224–1230, Mar 1998.

[158] J. Stenger and H. R. Telle. Intensity-induced mode shift in a femtosecond laser by a change in the nonlinear index of refraction. *Opt. Lett.*, 25(20):1553–1555, Oct 2000.

[159] M. Sheik-Bahae, D. C. Hutchings, D.J. Hagan, and E. W.; Van Stryland. Dispersion of bound electron nonlinear refraction in solids. *IEEE J. Quantum Electron.*, 27:1296–1309, 1991.

[160] R. Desalvo, A. A. Said, D. J. Hagan, E. W. Van Stryland, and M. Sheik-Bahae. Infrared to ultraviolet measurements of two-photon absorption and n_2 in wide bandgap solids. *IEEE J. Quantum Electron.*, 32:1324–1333, 1996.

[161] I. Coddington, W. C. Swann, L. Lorini, J. C. Bergquist, Y. Le Coq, C. W. Oates, Q. Quraishi, K. S. Feder, J. W. Nicholson, P. S. Westbrook, S. A. Diddams, and N. R. Newbury. Coherent optical link over hundreds of metres and hundreds of terahertz with subfemtosecond timing jitter. *Nat Photon*, 1(5):283–287, May 2007.

[162] J. L. Hall. Nobel lecture: Defining and measuring optical frequencies. *Rev. Mod. Phys.*, 78(4):1279–1295, Nov 2006.

[163] S. A. Diddams. The evolving optical frequency comb [invited]. *J. Opt. Soc. Am. B*, 27(11):B51–B62, Nov 2010.

[164] T. A. Birks, W. J. Wadsworth, and P. St. J. Russell. Supercontinuum generation in tapered fibers. *Opt. Lett.*, 25(19):1415–1417, 2000.

[165] K. F. Kwong, D. Yankelevich, K. C. Chu, J. P. Heritage, and A. Dienes. 400-hz mechanical scanning optical delay line. *Opt. Lett.*, 18(7):558–560, Apr 1993.

[166] A. Poppe, R. Holzwarth, A. Apolonski, G. Tempea, Ch. Spielmann, T.W. Hnsch, and F. Krausz. Few-cycle optical waveform synthesis. *Applied Physics B: Lasers and Optics*, 72:373–376, 2001. 10.1007/s003400000526.

[167] D. R. Walker, Th. Udem, Ch. Gohle, B. Stein, and T. W. Hänsch. Frequency dependence of the fixed point in a fluctuating frequency comb. *Applied Physics B*, 89:535–538, 2007.

[168] D. C. Heinecke, A. Bartels, T. M. Fortier, D. A. Braje, L. Hollberg, and S. A. Diddams. Optical frequency stabilization of a 10 ghz ti:sapphire frequency comb by saturated absorption spectroscopy in ^{87}rb. *Phys. Rev. A*, 80:053806, 2009.

[169] M. Tarallo, N. Poli, M. Schioppo, D. Sutyrin, and G. Tino. A high-stability semiconductor laser system for a ⁸⁸sr-based opti-

cal lattice clock. *Applied Physics B: Lasers and Optics*, 103:17–25, 2011. 10.1007/s00340-010-4232-2.

[170] M. G. Tarallo. *Development of a Strontium optical lattice clock*. PhD thesis, University of Pisa, 2009.

[171] M. S. Pshenichnikov, A. Baltuska, R. Szipcz, and D. A. Wiersma. *Ultrafast Phenomena XI*, chapter Sub-5-fs pulses: generation, characterization, and experiments, page 3. Springer, Berlin, Heidelberg, 1998.

[172] Z. Cheng, G. Tempea, T. Brabec, K. Ferenc, C. Spielmann, and F. Krausz. *Ultrafast Phenomena XI*, chapter Generation of intense diffraction-limited white light and 4-fs pulses, page 8. Springer, Berlin, Heidelberg, 1998.

[173] A. Baltuska, Z. Wei, M. S. Pshenichnikov, and D. A. Wiersma. Optical pulse compression to 5 fs at a 1mhz repetition rate. *Opt. Lett.*, 22:102, 1997.

[174] M. Nisoli, S. De Silvestri, O. Svelto, R. Szipöcs, K. Ferenc, C. Spielmann, S. Sartania, and F. Krausz. Compression of high-energy laser pulses below 5 fs. *Opt. Lett.*, 22:522, 1997.

[175] P. K. Mukhopadhyay, M. B. Alsous, K. Ranganathan, S. K. Sharma, P. K. Gupta, J. Gupta, George J., and T. P. S. Nathan. Simultaneous q-swithing and mode-locking in an intracavity frequency doubled diode-pumped nd:yvo4/ktp green laser with cr4+:yag. *Optics Communication*, 222:399–404, 2003.

[176] W. T. Silfvast. *Laser Fundamentals*. United State: Cambridge University Press, 2004.

[177] A. M. Kowalevicz. *Novel Femtosecond Laser Development with Application in Biomedical Imaging and Photonic Device Fabrication*. PhD thesis, Harvard university, 2004.

[178] A. L. Lytle, E. Gershgoren, R. I. Tobey, M. M. Murnane, H. C. Kapteyn, and D. Müller. Use of a simple cavity geometry for low and high repetition rate modelocked ti:sapphire lasers. *Optics Express*, 12(7):1409–1416, 2004.

[179] J. Turunen. Astigmatism in laser beam optical systems. *Appl. Opt.*, 25(17):2908–2911, Sep 1986.

[180] H. W. Kolgenik, E. P. Ippen, A. Dienes, and C. V. Shank. Astigmatically compensated cavities for cw dye lasers. *IEEE J. of Quantum Electronic*, 8:373–379, 1972.

[181] T. D. Donnelly and C. Grossman. Ultrafast phenomena: A laboratory experiment for undergraduates. *Am. J. Phys.*, 66 (8):677–685, 1998.

[182] S. Schneider, A. Stockmann, and W. Schulbauer. Self-starting mode-locked cavity-dumped femtosecond ti:sapphire laser. *Optics Express*, 6 (11):220–226, 2000.

[183] T. C. Briles, D. C. Yost, A. Cingöz, J. Ye, and Th. R. Schibli. Simple piezoelectric-actuated mirror with 180 khz servo bandwidth. *Opt. Express*, 18(10):9739–9746, 2010.

[184] G. D. Boyd and D. A. Kleinman. Parametric interactions of focused gaussian light beams. *J. Appl. Phys.*, 39:3897–, 1968.

[185] S. M. Saltiel, K. Koynov, B. Agate, and W. Sibbett. Second-harmonic generation with focused beams under conditions of large group-velocity mismatch. *J. Opt. Soc. Am. B*, 21(3):591–598, 2004.

[186] R. W. Fox, H. G. Robinson, A. S. Zibrov, N. Mackie, J. Marquardt, J. Magyar, and L. Hollberg. In *Proc. SPIE Int. Soc. Opt. Eng.*, volume 1837, page 360, 1992.

[187] N. Poli, G. Ferrari, M. Prevedelli, F. Sorrentino, R. E. Drullinger, and G. M. Tino. Laser sources for precision spectroscopy on atomic strontium. *Spectrochimica Acta Part A: Molecular and Biomolecular Spectroscopy*, 63(5):981 – 986, 2006. 5th International Conference on Tunable Diode Laser Spectroscopy, 2005.

[188] N. Poli, M. G. Tarallo, M. Schioppo, C. W. Oates, and G. M. Tino. A simplified optical lattice clock. *Appl. Phys. B*, 97:27–33, 2009.

[189] R. W. P. Drever, J. L. Hall, F. V. Kowalski, J. Hough, G. M. Ford, A. J. Munley, and H. Ward. Laser phase and frequency stabilization using an optical resonator. *Applied Physics B: Lasers and Optics*, 31:97–105, 1983. 10.1007/BF00702605.

[190] B. C. Young, F. C. Cruz, W. M. Itano, and J. C. Bergquist. Visible lasers with subhertz linewidths. *Phys. Rev. Lett.*, 82(19):3799–3802, May 1999.

[191] A. D. Ludlow, X. Huang, M. Notcutt, T. Zanon-Willette, S. M. Foreman, M. M. Boyd, S. Blatt, and J. Ye. Compact, thermal-noise-limited optical cavity for diode laser stabilization at 1×10−15. *Opt. Lett.*, 32(6):641–643, Mar 2007.

[192] G. Ferrari, P. Cancio, R. Drullinger, G. Giusfredi, N. Poli, M. Prevedelli, C. Toninelli, and G. M. Tino. Precision frequency measurement of visible intercombination lines of strontium. *Phys. Rev. Lett.*, 91(24):243002, Dec 2003.

[193] L. Chen, J. L. Hall, J. Ye, T. Yang, E. Zang, and T. Li. Vibration-induced elastic deformation of fabry-perot cavities. *Phys. Rev. A*, 74(5):053801, Nov 2006.

[194] K. Numata, A. Kemery, and J. Camp. Thermal-noise limit in the frequency stabilization of lasers with rigid cavities. *Phys. Rev. Lett.*, 93(25):250602, Dec 2004.

[195] G. Rempe, R. J. Thompson, H. J. Kimble, and R. Lalezari. Measurement of ultralow losses in an optical interferometer. *Opt. Lett.*, 17(5):363–365, Mar 1992.

[196] S. Schilt, N. Bucalovic, V. Dolgovskiy, Ch. Schori, M.C. Stumpf, G. Di Domenico, S. Pekarek, A. E. H. Oehler, Th. Südmeyer, U. Keller, and P Thomann. Fully stabilized optical frequency comb with sub-radian ceo phase noise from a sesam-modelocked 1.5-μm solid-state laser. *Opt. Express*, 19(24):24171–24181, Nov 2011.

[197] L. B. Mercer. 1/f frequency noise effects on self-heterodyne linewidth measurements. *J. Lightwave Technol.*, 9:485–493, 1991.

[198] W.-Y. Cheng, T.-H. Wu, S.-W. Huang, S.-Y. Lin, and C.-M. Wu. Stabilizing the frequency of femtosecond ti:sapphire comb laser by a novel scheme. *Applied Physics B*, 92:13–, 2008.

[199] N. Beverini, N. Poli, D. Sutyrin, F.-Y. Wang, M. Schioppo, M. G. Tarallo, and G. M. Tino. Absolute frequency measurement of unstable lasers with optical frequency combs. In *Proc. SPIE*, page 79931I, 2010.

[200] Wavelength control white paper. Technical report, Coherent, 2010.

[201] M.N. Skvortsov, M.V. Okhapkin, A.Yu. Nevsky, and S.N. Bagaev. Optical frequency standard based on a nd:yag laser stabilised by saturated absorbtion resonances in molecular iodine using second-harmonic radiation. *Quantum Electron*, 34 (12):1101–1106, 2004.

[202] Yu.A. Matyugin, M.V. Okhapkin, M.N. Skvortsov, S.M. Ignatovich, and S.N. Bagaev. Study of the hyperfine structure of emission lines of i_2 molecules by the method of three-level spectroscopy. *Quantum Electron*, 38 (8):755–763, 2008.

[203] C. Grebing, M. Görbe, K. Osvay, and G. Steinmeyer. Isochronic and isodispersive carrier-envelope phase-shift compensators. *Applied Physics B*, 97(3):575–581, 2009.

[204] I.M. Beterov and V.P. Chebotaev. *Progress in Quantum Electronics*, 3:1, 1974.

[205] N. Poli, M. G. Tarallo, M. Schioppo, C. W. Oates, S. Chepurov, D. Sutyrin, A. De Michele, N. Beverini, and G. M. Tino. Strontium optical lattice clock. In *Proceedings of the 5th International Symposium "Modern Problems of Laser Physics (MPLP'2008)*, page 327, Novosibirsk, Russia, August 24-30 2008.

[206] N. Poli, R. E. Drullinger, G. Ferrari, and et al. In *Proc. SPIE*, volume 6673, page 66730F, 2007.

[207] F. Sorrentino, G. Ferrari, N. Poli, R. E. Drullinger, and Tino G. M. Laser cooling and trapping of atomic strontium for ultracold atoms physics, high-

precision spectroscopy and quantum sensors. *Mod. Phys. Lett. B*, 20:1287–1320, 2006.

[208] N. Poli, M. G. Tarallo, M. Schioppo, C. W. Oates, S. Chepurov, D. Sutyrin, A. De Michele, N. Beverini, and G. M. Tino. Strontium optical lattice clock. In *Proceedings of the 5th International Symposium "Modern Problems of Laser Physics" (MPLP'2008) Novosibirsk, Russia, August 24-30*, page 327, August 24-30 2008.

[209] G. Ferrari, N. Poli, F. Sorrentino, and G. M. Tino. Long-lived bloch oscillations with bosonic sr atoms and application to gravity measurement at the micrometer scale. *Phys. Rev. Lett.*, 97(6):060402, Aug 2006.

[210] M. Planat, editor. *Noise, Oscillators, and Algebraic Randomness : From Noise in Communication Systems to Number Theory. Lectures in Physics*, volume 550. Springer-Verlag Heidelberg.

[211] E. Rubiola. *Phase noise and frequency stability in oscillators.* Cambrige University Press.

[212] R. W. Cahn, P. Haasen, and E. J. Kramer, editors. *Materials Science and Technology*, volume 11. Wiley-VCH, Weinheim, 1994.

[213] J. J. Gagnepain. *Piezoelectricity.* Gordon & Breach, New York, 1982.

[214] W. Jitschin and G. Meisel. Fast frequency control of a cw dye jet laser. *Applied Physics A: Materials Science & Processing*, 19:181–184, 1979. 10.1007/BF00932394.

[215] J. L. Hall. Stabilizing lasers for applications in quantum optics. In J.D. Harvey and D.F. Walls, editors, *Quantum Optics IV*. Springer Verlag: Proceedings of the Fourth International Conference, Hamilton NZ, 1986.

[216] J. L. Hall, M. S. Taubman, and J. Ye. *Handbook of Optics: Fiber Optics and Nonlinear Optics*, volume 4, chapter Laser Stabilization, page 27.1. McGraw-Hill, New York, 2001.

[217] T. Day, E. K. Gustafson, and R. L. Byer. Sub-hertz relative frequency stabilization of two-diode laser-pumped nd:yag lasers locked to a fabry-perot interferometer. *IEEE J. Quan. Elec.*, 28:1106, 1992.

[218] C. E. Wieman and L. Hollberg. Using diode lasers for atomic physics. *Rev. Sci. Instrum.*, 62:1, 1991.

[219] E. Hecht. *Optics*. Addison-Wesley, Reading, Mass, 1998.

[220] R. V. Pound. Electronic frequency stabilization of microwave oscillators. *Rev. Sci. Instrum.*, 17:490, 1946.

[221] G. Franklin, J. D. Powell, and A. A. Emami-Naeini. *Feedback control of dynamic systems*. Menlo Park: Addison-Wesley Publishing, 1988.

[222] P. Horrowitz and W. Hill. *The Art of Electronics*. Cambridge Univ. Press, Cambridge, 2 edition, 1989.

[223] J. Magnes, D. Odera, J. Hartke, M. Fountain, L. Florence, and V. Davis. Quantitative and qualitative study of gaussian beam visualization techniques. *Arxiv preprint physics/0605102*, 2006.

Appendix A

The absolute frequency measurement of molecular iodine

In this chapter report, as an application of the OFC technology, the work on absolute frequency measurement on iodine molecule in the far infrared that I have performed in a stage at the Institute of Laser Physics SB RAS in Novosibirsk.

A.1 Introduction

The absorption spectrum of molecular iodine I_2 is widely used as a frequency scale for the calibration of tunable laser in 500-800 nm optical range. The narrow optical resonances, obtained by saturated absorption laser spectroscopy, are even used as high accuracy frequency references. The transitions, which can be suitable for optical standards, might be discovered in the I_2 optical spectrum up to 1.35 μm wavelength range by the three-level laser spectroscopy method. The optical region 0.9-1.35 μm has a particular interest due to the fact that presently there are no high accuracy reference standards, while there are many tunable lasers used for spectroscopy, communication technology and metrology.

A.2 Apparatus

A.2.1 Ti:Sa OFC

The OFC that is used in the measurements is based on a femtosecond laser with f_{rep} at 500 MHz. As a pump source is used a commercial laser Verdi V8. The f_{rep} is stabilized to Nd:YAG/I_2 optical frequency standard created in ILP SB RAS [201]. This stabilization was done by two phase lock loop (PLL) with two PZT to which was attached two laser cavity mirrors. In the slow PLL was used stock PZT allowing to work in bandwidth up to $\sim$ 5 kHz. For the fast PLL was implemented ring PZT with low frequency bandwidth at 30 kHz. To control the pump power level was used an acousto-optic modulator with bandwidth up to 20 kHz.

The output radiation from the fs Ti:Sa laser was broadened by the PCF Femtowhite 8000 more than octave from 400 nm to 1100 nm. The green part of the output signal from the PCF was beat with signal from Nd:YAG/I_2 standard and a beatnote signal was sent to the phase detector and than to the slow and fast PZT of the Ti:Sa laser. In this way the phase stabilization of the f_{rep} to Nd:YAG/I_2 frequency standard was obtained. Another part of the PCF output was sent to the f-2f interferometer. The output signal from it was sent to the phase detector and than to an AOM order to stabilize f_{CEO}. Thus was made a stabilization of the both OFC degrees of freedom: f_{rep} and f_{CEO}.

The optical cavity of the femtosecond Ti:Sa laser is placed in the metal box 40 $\times$ 40 $\times$ 40 mm to protect it from an environmental noise. The box is tightly fixed on a 1000 $\times$ 500 breadboard that is placed on a big 8 $\times$ 1 m massive table.

The stability of the OFC is measured against a commercial hydrogen maser. The measured relative instability is 1×10^{-12} at 1 s and for averaging times less than 1000 s it is determined by the microwave standard. For longer times more than 1000 s the frequency drift of the Nd:YAG/I_2 optical standard is dominant [201].

A.2.2 An apparatus for obtaining and investigations of emissive transitions optical resonances

The apparatus for obtaining and investigations of emissive transitions optical resonances was done by *Matygin* et al. [202]. It is a combine of the two laser spectrom-

eter. First is a saturated absorption spectrometer, the second one is a three-level laser spectrometer. As an exciting radiation the second harmonic of cw Nd:YAG laser is used. An external cavity diode laser is used to product a probe radiation in an optical range of 968-998 nm. The apparatus are guarantee a phase lock of probe beam frequency to an emissive transition and at the same time phase lock of a pump laser to an absorption transmission. Only in this case the probe laser frequency is equal to emissive transition frequency. The measurement of probe beam frequency gives the value of emissive transition frequency.

A.3 Modification of the setup

Some modifications of OFC setup were done during measurements of the molecular iodine.

A.3.1 New PZT mount

To obtain f_{rep} stabilization in long-term the PZT with big range of length tunability is typically used. It is attached to a massive block plus a mirror. The main problem of this system is its mechanical resonances that limit the bandwidth of PLL. These resonance strongly depend on characteristics of PZT, overall mass of system to which PZT attached and method (quality) of glue of PZT to the massive block. The proper design of PLL should consider the resonance of such system.

The most accurate method of PZT bandwidth measurement is based on the Michelson interferometer. In Fig. A.1 the experimental setup is presented.

The setup is a typical Michelson interferometer. An interference picture detected by the photodetector PD. The signal from PD sent to the channel 2 of the oscilloscope and to the lock system. From the generator of low frequencies the signal going through a low frequency amplifier to PZT and to the channel 1 of the oscilloscope. Another part of the generator signal goes to the lock system. The output signal from the lock system control the additional PZT and change the length of the beam path.

Example of PZT bandwidth measurements is presented in Fig. A.2 (frequency response) and Fig. A.3 (phase response). Two resonances are observed at 46 and 51 kHz both in frequency and phase responses. Note, that amplitude of frequency

resonance is not critical because in principal can be compensated by proper design of PLL. While the phase change when it is reached 180◦ will limit the bandwidth of PLL. In this measurement we can see phase change of about 80◦ each.

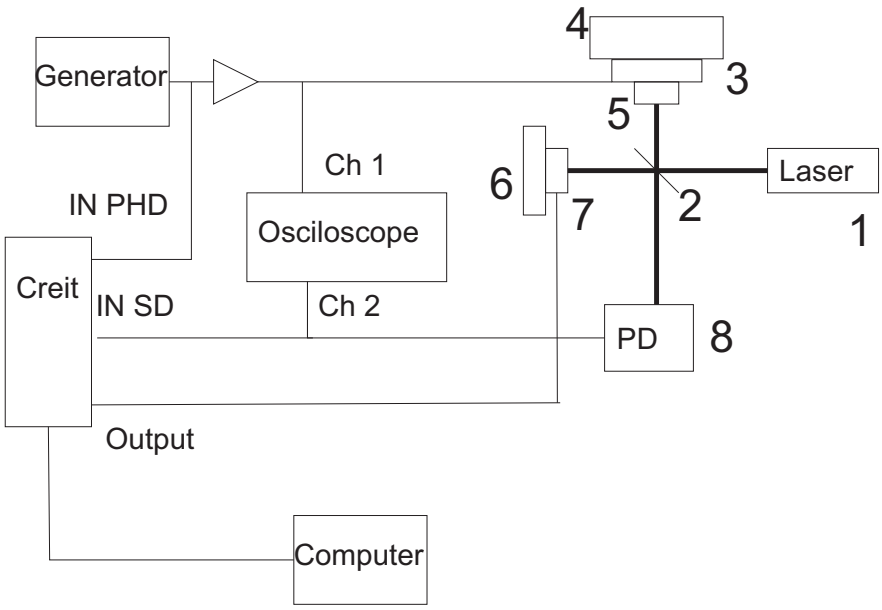

Figure A.1: *The setup for PZT resonances measurement. 1 is commercial He-Ne laser, 2 is a mirror, 3 is the tested PZT, 4 is a massive block, 5 is a plane mirror, 6 is an additional PZT, 7 is plane mirror, 8 is a photodetector*

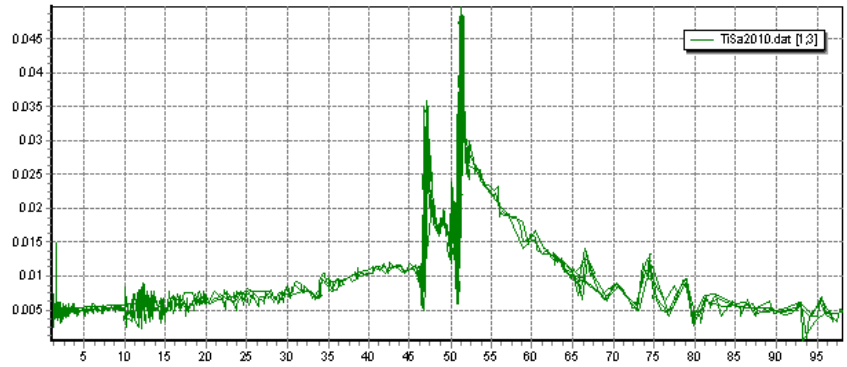

Figure A.2: *PZT frequency resonance*

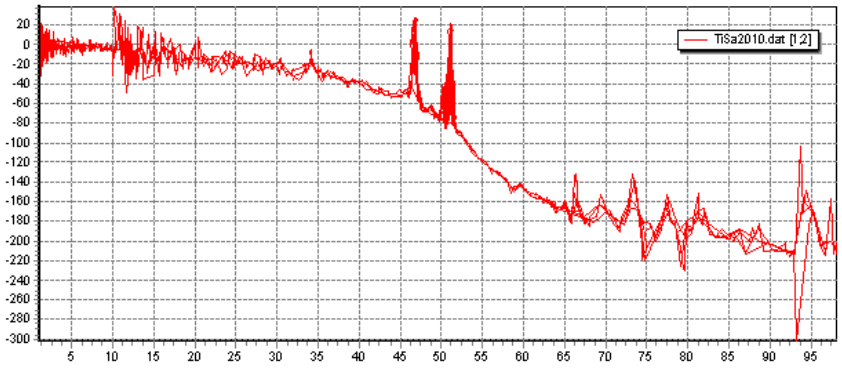

Figure A.3: *PZT phase resonance*

A.3.2 Carrier-envelope phase-shift management

Many experiments in frequency metrology [44, 86] rely on the precise control of the $\Delta\phi_{CEO}$ of fs oscillators and amplifier systems. The control of this parameter typically requires manipulation of the phase and the group velocities inside a fs oscillator cavity. One important consideration for the choice of a device for manipulating the $\Delta\phi_{CEO}$ is the rate at which the $\Delta\phi_{CEO}$ can be modulated. Orthogonality of a $\Delta\phi_{CEO}$ modulator is a second important issue. The most straightforward approach for introducing a change of the $\Delta\phi_{CEO}$ is variation of material dispersion in the beam path. In the simplest case this has been accomplished by inserting glass plates of various thickness into the cavity or beam path or by rotating a single glass plate [203].

To prepare Ti:Sa OFC for the applications where $\Delta\phi_{CEO}$ control is becomes important, a wedge pair mechanism is start to be designed.

A.4 Measurement

For the frequency measurements of the intervals between hyperfine structure components of the emissive transitions is used a heterodyne method. It based on the measurement of the frequency distance between two probe lasers, which frequencies are phase locked to the different hyperfine structure components of the same emissive transition. The frequency measurement is done by the Ti:Sa OFC.

The measured frequency f_d was determined by the equation $f_d = n \times f_m \pm f_{CEO} \pm f_{bd}$, where f_{bd} is the beatnote between the diode laser and corresponding tooth of the OFC. In turn, $f_{CEO} = f_i \pm f_{h1}$ and $f_{bd} = f_m \pm f_{h2}$, where f_i is the intermidiate frequency, f_i is a measured frequency, f_{h1} and f_{h2} are heterodyne frequencies. The f_i, f_{h1} and f_{h2} are synthesized from the hydrogen microwave standard. The frequencies of 20 transitions were measured: R56(32-48) a1, P58(32-48) a1, P85(33-48) a1, R87(33-48) a1, R88(33-48) a10 and all 15 components of R86(33-48) line. The results are presented in the Tab. A.1.

Table A.1: Measured frequencies of molecular iodine

Line	Component	Transition frequency (kHz)
P58 (32-48)	a1	304 360 509 340 (14)
R56(32-48)	a1	304 569 862 427 (19)
R87 (33-48)	a1	305 158 831 718 (13)
P85 (33-48)	a1	305 473 035 236 (11)
P88 (33-48)	a10	305 112 914 648 (15)
R86 (33-48)	a1	305 430 191 096 (22)
R86 (33-48)	a2	305 430 419 457 (65)
R86 (33-48)	a3	305 430 450 726 (5)
R86 (33-48)	a4	305 430 460 143 (48)
R86 (33-48)	a5	305 430 490 794 (10)
R86 (33-48)	a6	305 430 556 161 (63)
R86 (33-48)	a7	305 430 570 683 (3)
R86 (33-48)	a8	305 430 604 295 (53)
R86 (33-48)	a9	305 430 618 684 (36)
R86 (33-48)	a10	305 430 719 880 (30)
R86 (33-48)	a11	305 430 832 083 (28)
R86 (33-48)	a12	305 430 839 995 (27)
R86 (33-48)	a13	305 430 864 083 (33)
R86 (33-48)	a14	305 430 872 845 (36)
R86 (32-48)	a15	305 430 984 743 (31)

A.5 Discussion

The measurements root-mean-square deviation $\sigma \sim 2$kHz at 100 s. Big deviations were observed for longer measurement periods. The maximum deviation from the average value was 30 kHz. For different lines σ was 11-22 kHz. The deviations of measured values from day to day were up to 40 kHz.

The precision of the OFC is at the level of 1 kHz. For this reason the deviations should be caused by the frequency instability of the diode laser. The measured frequency stability of the diode laser locked to a hyperfine structure component of the iodine emissive transition $\sigma(1 - 100\text{s}) \sim 1 - 3 \times 10^{-11}$ for the averaging time 1-100 s. The frequency drift of diode laser was observed for the longer averaging time. This probably explained by not optimized parameters of the diode PLL.

The systematic errors are probably caused by the frequency shift due to the instability of iodine steam pressures in the cell. From the other works this shift can be evaluated from the other works. In the work [204] for iodine absorption lines in the infrared region the frequency shift due to the pressure is 5 kHz/Pa. The measurements of were done at the iodine cell temperature at 8∘C and corresponding iodine steam pressure is 9 Pa. Suppose that an absorption line frequency shift happens due to the shift of an upper state. So, in the emission transition the state shift should be the same as the state shift in an absorption transition. In our case this is 45 kHz. Finally, summing this value with the precision of our measurements, we estimate the inaccuracy of the results better than 100 kHz or 3×10^{-10}.

A.6 Conclusion

Were done measurements of the absolute frequency components of hyperfine structure of the molecule iodine $^{127}I_2$ emissive transitions in corresponded regions (32-48) and (33-48). The precision of the measurement in a comparison with other results, was improved by 2 orders of magnitude.

Appendix B

Ti:Sa physical properties

Table B.1: Physical properties of Ti:Sa

chemical formula	Ti^{3+}:Al_2O_3
crystal structure	hexagonal
mass density	3.98 g/cm^3
Moh hardness	9
Young's modulus	335 GPa
tensile strength	400 MPa
melting point	2040°C
thermal conductivity	33 W/(mK)
thermal expansion coefficient	$\sim 5\times10^{-6}$K^{-1}
thermal shock resistance parameter	790 W/m
birefringence	negative uniaxial
refractive index at 633 nm	1.76
temperature dependence of refractive index	13×10^{-6}K^{-1}
Ti density for 0.1% at. doping	$4.56\times10^{19} cm^{-3}$
fluorescence lifetime	3.2 μs
emission cross section at 790 nm	$41\times10-20$cm^2

Appendix C

Cooling and trapping strontium atoms

In this and the next sections I will describe shortly the apparatus of our strontium optical clock that was developed by our group at European Laboratory for Non-linear Spectroscopy (LENS) for the realization of an optical frequency standard based on neutral strontium atoms and that was used for the measurement with our OFC. The further details of its can be found in [169, 170, 205].

Strontium vapours are generated from a Sr dispenser in the oven region. Atoms are then decelerated in a 30 cm long Zeeman slower, and finally trapped and cooled in the MOT chamber. With the current setup it is possible to cool and trap about 10^7 ^{88}Sr atoms at μK temperatures in hundreds of ms. The laser sources for trapping and cooling are based on semiconductor laser diodes (see a level scheme of Sr with the transition lines in Fig. 5.1b). For the first cooling and trapping stage on the $^1S_0$-$^1P_1$ transition we used two frequency doubled infrared lasers that deliver respectively 200 mW at 461 nm (922 nm extended cavity diode laser amplified with a tapered amplifier and doubled in doubling cavity with BiBO crystal) and 1 mW at 497 nm (994 nm ECDL frequency doubled with $KNbO_3$ crystal). For the second stage cooling on the $^1S_0$-$^3P_1$ transition, a frequency stabilized ECDL at 689 nm is employed [187, 206, 207].

C.1 689 nm laser

The second stabilized laser is a 689 nm diode laser, based on the same design that the clock 698 nm source. This laser is referred to the $^1S_0$-$^3P_1$ intercombination transition in atomic strontium optically cooled in a magneto-optical-trap (MOT) [187].

The scheme of the red source at 689 nm resonant with the intercombination $^1S_0$-$^3P_1$ transition for the bosonic strontium isotope is reported in Fig. C.1

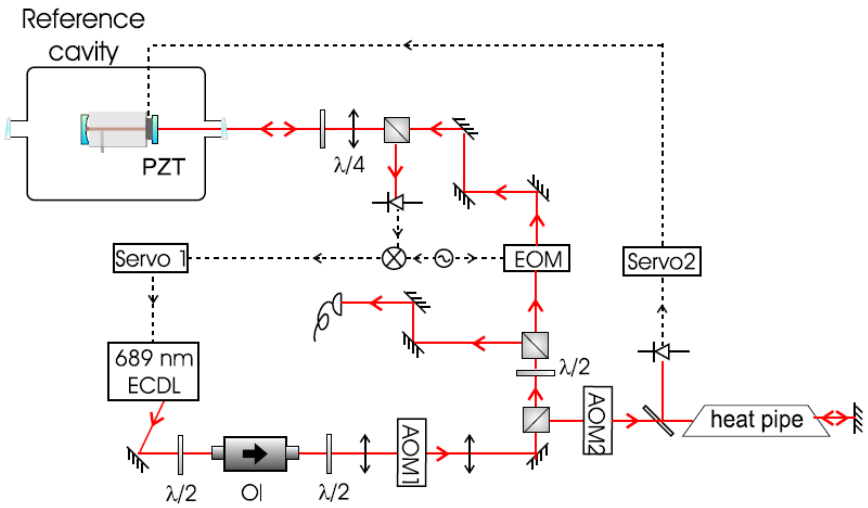

Figure C.1: 689 nm laser experimental scheme [169].

The master laser is a 689 nm diode laser mounted in extended cavity configuration (ECDL, Littrow mount). The reduction of the fast linewidth is realized by locking the laser to a resonance of a reference cavity with standard PDH technique. The laser electric field is phase modulated at 11 MHz with an electro-optic modulator (EOM) with a modulation index $m < 1$, while the error signal is obtained by demodulating the light reflected from the cavity. In order to reduce the optical feedback from the cavity, we use an optical isolator and an AOM in cascade at the output of the laser.

The cavity is composed by two mirrors (99.95% reflectivity at 689 nm), a plane and a curved one (r = 50 cm) and a 10 cm quartz spacer. The cavity is placed on a massive iron V-block (20 kg approx.) aligned along an horizontal axis. The

vacuum chamber that contains the cavity and the iron block is evacuated (10^{-6} Pa) and the vacuum is maintained with a 2 l/s ion pump. In order to attenuate the vibrations from the optical table, pieces of Viton O-ring and rubber are used interposed between the cavity and the iron and between the iron and the vacuum cell. The optical table is also supported with an active air damping system.

The reflected light from the cavity is collected with PDH detector: it is composed by a Si photodiode, amplified with a fast and low current noise transimpedance amplifier and finally down-converted with a mixer. The level of the voltage noise at the output of the detector is -110 dBV/Hz$^{1/2}$ which corresponds to the shot noise of 100 μW of incident light. The cavity resonance has a $\Delta\nu_{FWHM} = 170$ kHz and the slope of the error signal is 3.4 V/MHz. The error signal has then SNR ~ 200 in a bandwidth of 3 MHz. The error signal for locking the laser to the cavity is then sent to the laser via three channels: (1) to the PZT of the external cavity of the laser with a bandwidth of 2 kHz; (2) to the laser current driver with a bandwidth of 50 kHz; (3) directly to the diode with a bandwidth of 3 MHz.

For the long term stability of the laser we actively stabilize the length of the reference cavity with a lock to an atomic signal coming from saturation spectroscopy on a strontium heat pipe. For this purpose we use a PZT transducer, placed between the flat mirror of the cavity and the quartz spacer, for tuning the cavity length (PZT sensitivity 38 MHz/V). In order to reduce electronic noise induced by the PZT, two different voltages are applied to the two side of the PZT transducer: the first for coarse tuning of the cavity (up to 2 GHz) comes from a battery, while the small cavity length correction (up to 2 MHz) is delivered from low noise electronics.

The drift of the cavity in normal operation is of the order of 20 MHz/hr. In order to correct for this slow drift, we send the integrated error signal to the PZT of the cavity with an overall bandwidth of about 50 Hz. In normal operating condition, the dynamic range of the servo electronics allows a stable lock for about one day. The overall system (master laser, vacuum cell and optics) is quite compact and it fits on a single 60 cm $\times$ 60 cm aluminum breadboard.

Appendix D

Apparatus for precision measurement of gravity

The experimental setup is described in Fig. D.1. In brief, an ultracold sample of ^{88}Sr atoms is produced in a two-steps magneto-optical-traps operating on the dipole allowed $^1S_0$-$^1P_1$ transition at 461 nm and on the $^1S_0$-$^3P_1$ intercombination transition at 689 nm. Atoms are then transferred in 1D vertical lattice realized with about 2 W of laser radiation at 532 nm from Verdi V5. This system is employed for precision measurement of gravity through the observation of Bloch oscillation of trapped atoms [188]. The beam is vertically aligned and retro-reflected by a mirror, producing a standing wave with a period $\lambda_L/2 = 266$ nm. In this condition, the acceleration of gravity g is proportional both to the Verdi laser frequency and Bloch oscillation frequency through the formula

$$g = \frac{2h\nu_b}{(m_{Sr}\lambda_L)}, \tag{D.1}$$

where m_{Sr} is the atomic mass, λ_L is the lattice wavelength, ν_b is the observed Bloch oscillation frequency, and $\bar{h}$ is the Planck constant. Since m_{Sr} and $\bar{h}$ are well known (relative uncertainty 5×10^{-8}), the force acting along the lattice axis can be determined by measuring the Bloch frequency ν_b and the wavelength of the light λ_L emitted by the Verdi V5 laser. More details about the experimental setup can be found also in [187, 188, 207, 208] and in [209].

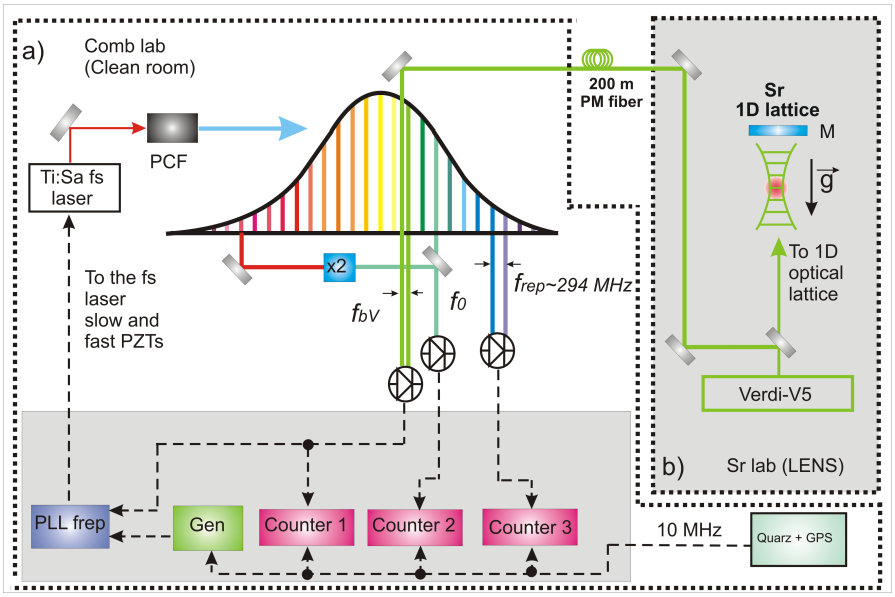

Figure D.1: Experimental setup for Verdi frequency calibration and 1D ^{88}Sr optical lattice. The output radiation from Verdi is focused on the ultra-cold ^{88}Sr cloud (b) and part of it is then sent through 200 m fiber to the OFC lab for frequency measurements (a). The beat-note signal between Verdi and the OFC is used to stabilize the f_{rep} of the femtosecond laser though PLL electronics that actuates slow and fast PZTs in the Ti:Sa cavity. All other interesting signals are counted with standard frequency counters. f_{bV} is the beat-notes between Verdi and OFC, f_0 is the CEO frequency, f_{rep} - repetition rate frequency, Gen - the RF reference synthesizer, PCF - photonic crystal fiber, M - retro-reflecting mirror for 1D lattice.

Appendix E

HeNe-laser based wavemeter

The wavemeter is not a commercial instrument. It has been developed in a Diploma thesis project at the Institute for Quantum Optics of the University of Hannover. Its relative accuracy 1×10^{-6} or better, the spectral range is 400-1100 nm, reference is unstabilized HeNe laser with $\lambda_{vacuum} = 632.9914$ nm, the free-spectral range is $\Delta\nu_{FSR}$ MHz.

E.1 Principle of Operation

The wavemeter is based on a Michelson interferometer in Genzel arrangement with retro-reflectors ("cat-eyes") in each arm (Fig. E.1). An unstabilized HeNe laser is used as a wavelength reference. While the mirrors are moving at relatively constant speed (i.e., in the middle of linear movement) fringes are counted for both the reference and the input laser. Near the end-points, where the movement of the carriage is more strongly accelerated, the interferometer signal is interpolated between two zero crossing using an internal high-frequency oscillator. This results in a high relative accuracy in very compact setup and allows a high measurement rate which is important for easy handling and wavelength tuning of lasers.

There is an internal microprocessor that controls the measurement process and calculates wavelength, frequency, etc.

E.2 Practical use: alignment of the input laser beam

To achieve the full accuracy of the wavemeter the input laser beam has to be carefully aligned. First method is to use the reference HeNe beam as a guide beam. For this it is necessary to align the input laser beam (while not touching any mirrors or beam splitters of the wavemeter assembly itself) such that its beam and the reference beam (coming from mirror 3) coincide both at splitter 3 and tho to three meters away from splitter 3 outside the wavemeter assembly (Fig. E.1). The best way to achieve this is to have one external mirror 4 as close as possible to splitter 3 and the fiber coupler 1 far away from it. With the fiber coupler 1 the overlap at splitter 3 can be optimized, and then the alignment of the close mirror 4 will change the overlap of the beams far away from splitter 3, (almost) without affecting the overlap at splitter 3. To achieve convergence this process should be repeated as often as necessary.

However, we found, that this method does not give the best accuracy of the wavemeter. For this reason, we modified the alignment scheme. We add the removable mirror after the splitter 2 that send the input laser beam and the reference HeNe beam to fiber coupler 2. The mirror 5 and the fiber coupler 2 mount are used for the alignment the HeNe-laser reference beam. The fiber coupler 1 and mirror 4 are used for the alignment the input beam of measured laser. The alignment is finished when maximum power level is detected by photodetector for both beam at the end of the fiber.

Another important thing, to achieve the wavemeter full accuracy, is power level on the input beam. There are four BNC connectors that can be used to maximize fringe contrast and fringe height. They provide the monitor signals of reference laser and input laser fringes. The best accuracy is achieved when the reference and input laser signals gives equal amplitudes of the monitored signals. To control the amplitude of the input laser signal we add a polarizing splitter 4 and a $\lambda/2$ before the splitter 3.

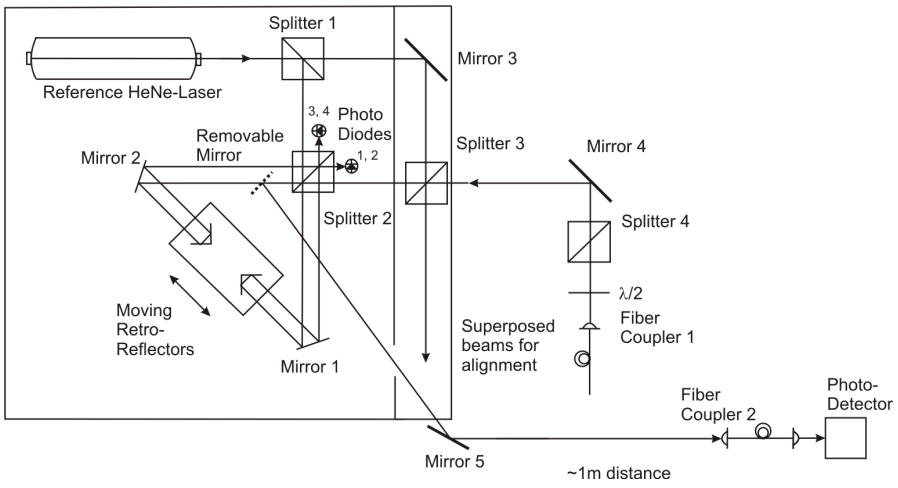

Figure E.1: Optical setup of the wavemeter.

Appendix F

Frequency Stabilization of Lasers

In the final Sect. F the laser stabilization basis is described.

Noise, stability, linewidth, reproducibility, and the uncertainty of the frequency are important parameters of any frequency-stabilized laser. In general, the laser frequency fluctuates about a mean value which itself may drift and walk randomly. Such variations may be caused, e.g., by changes in the temperature, air pressure, vibrations, acoustics or by fluctuations within the active laser medium itself.

F.1 Oscillator phase noise

Ideal sinusoidal oscillators of frequency f_0 have a mathematically strict spectrum in the form of delta functions, centered at $-f_0$ and f_0. However, practical oscillators seldom exhibit this kind of clean spectrum. They tend to have spreading of spectral energy around the carrier frequency, as shown in Fig. F.1. The spreading or spillage of energy to neighboring points around f_0 can cause unwanted behavior at both transmitter and receiver mixers. This spillage of spectral energy behave like unwanted phase-modulation and is called phase noise.

F.1.1 Representing phase noise

Ideal receiver carrier should be equal to transmitter carrier

$$v_0 \cos(\omega_0 t) \tag{F.1}$$

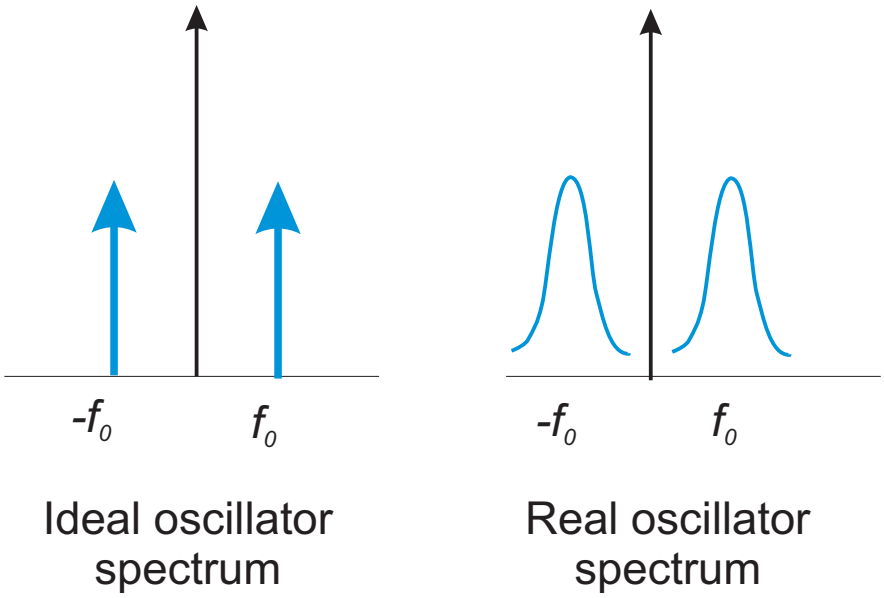

Figure F.1: Oscillator Spectrum; Ideal sinusoidal oscillator will have a Delta function spectrum. Practical oscillators will have energy spread around the oscillator frequency. Figure shown here is a two sided power spectrum representation of ideal and practical oscillators.

The receiver carrier signal in a real receiver can be written as,

$$v(t) = v_0(1 + \alpha(t)) \cos\left(\omega_0 t + \phi(t) + \frac{\beta}{2}t^2\right) \tag{F.2}$$

The long term drift effect of the oscillator due to ageing is reflected in β, $\alpha(t)$ is the amplitude noise and $\phi(t)$ represents phase noise. The phase noise $\phi(t)$ will have deterministic component as well as random components. The deterministic component is attributed by physical phenomena like supply voltage, temperature change, output impedance of the oscillator etc. The random nature of the phase noise is usually represented with a power spectral density expressed in power law.

Instantaneous frequency of $v(t)$ is

$$f(t) = \frac{1}{2\pi}\frac{d}{dt}\left(2\pi f_0 + \phi(t)\right) \tag{F.3}$$

The fractional frequency offset is then,

$$y(t) = \frac{\Delta f(t) - (f(t) - f_0)}{f_0} = \frac{1}{2\pi f_0}\frac{d\phi(t)}{dt} \tag{F.4}$$

Since $\phi(t)$ is assumed to be stationary, $y(t)$ is also stationary. Thus, the autocorrelation function $R_y(\tau)$ can be written as,

$$R_y(\tau) = \langle y(t), y(t-\tau)\rangle \tag{F.5}$$

The double sided PSD S_y^{DS} is obtained by performing Fourier transform on $R_y(\tau)$.

$$S_y^{DS}(f) = \int_{\infty}^{\infty} R_y(\tau)e^{-j2\pi f\tau}d\tau \tag{F.6}$$

from which, the one sided PSD S_y^f can be written as,

$$S_y(f) = \begin{cases} 2S_y^{DS}(f), & f \geq 0 \\ 0, & f < 0 \end{cases} \tag{F.7}$$

F.1.2 Power spectral density of the Phase Noise

Instead of representing the power spectrum of the instantaneous frequency change, it is possible to use the power spectral density (PSD) of the phase noise $\phi(t)$ itself. These two representations are equivalent. Both these representations are used in literature.

First the autocorrelation of $\phi(t)$ is computed:

$$R_\phi(\tau) = \langle \phi(t), \phi(t-\tau)\rangle \tag{F.8}$$

Upon Fourier transform, we get the double sided PSD $S_\phi^{DS}(f)$

$$S_\phi^{DS}(f) = \int_{\infty}^{\infty} R_\phi(\tau)e^{-j2\pi f\tau}d\tau \tag{F.9}$$

The commonly used single sideband representation $S_\phi(f)$ or simply $S(f)$ is:

$$S(f) = \begin{cases} 2S_\phi^{DS}(f), & f \geq 0 \\ 0, & f < 0 \end{cases} \tag{F.10}$$

Phase noise power spectral density are mathematically represented using the power law formula. Even though oscillators do not strictly adhere to the exact integer power representation, it is widely used to perform analytical calculations.

A simplified model of the random phase noise has a PSD of the form,

$$S(f) = a + \begin{cases} b, & f_3 \geq f \\ \frac{c}{f}, & f_2 \geq f \geq f_3 \\ \frac{d}{f^2}, & f_1 \geq f \geq f_3 \end{cases} \tag{F.11}$$

Phase noise power spectral density is usually represented as dBc. This expresses the statistical power of the phase noise signal with respect to the statistical power of the carrier signal in passband.

F.1.3 Power law model

From experimental observations, the phase noise power spectrum is approximated by the well known power law model [210]. The oscillator phase noise thus follows the PSD formula,

$$S_y(f) = \sum_{n=-2}^{2} h_n f^n \tag{F.12}$$

This Eq. F.12 correspond to five independent noise process listed in Table F.1. Expressed in this functional form, phase noise PSD follows a piecewise exponential relationship with the offset frequency (from oscillator center frequency). When the PSD is specified in dB scale (as is the practice) and on a log abscissa scale (log(f)) this turns out to be like piecewise linear relationship. Thus frequency random walk has a slope of -20 dB/octave and flicker noise 10 dB/octave.

Practical oscillators may not exactly have the slopes to be -20 dB/octave or -10 dB/octave. They could be arbitrary. To accommodate this change, the power law equation will have real valued powers (not necessarily integer powers).

$$S(f) = \sum_{n \leq 0, n \in R} h_n f^n \tag{F.13}$$

Given the phase noise PSD corner frequencies and specified power (measured at 1Hz of bandwidth at these corner points) in dBc/Hz, the slope can be calculated.

F.1.4 Allan variance

In order to compare a stability of any two lasers is used an Allan variance method. Allans idea is to focus on consecutive frequency measurements - by making a series of adjacent frequency measurements, each obtained by averaging over a period of time τ and separated in time by τ , the difference in frequency between consecutive measurements can be computed. Then plotting the rms frequency difference between adjacent measurements as a function of τ reveals how the oscillators frequency is fluctuating over the various timescales.

The signal from the frequency source can be expressed as

$$E(t) = E_0 \cos\left[2\pi\nu_0 t + \phi(t)\right] \tag{F.14}$$

The instantaneous fractional frequency deviation from the nominal center frequency is given by

$$y(t) = \frac{1}{2\pi\nu_0}\frac{d}{dt}\phi(t) \tag{F.15}$$

The Allan variance for an averaging time is then defined as

$$\sigma_y^2(\tau)^2 \equiv \langle\frac{1}{2}[\bar{y}(t+\tau) - \bar{y}(t)]^2\rangle \tag{F.16}$$

where $\langle\rangle$ indicates an infinite time average and $\bar{y}$ represents the time average of $y(t)$ over a period τ. $\sigma_y(\tau)$ can be estimated from a finite set of N consecutive average values of the center frequency, $\bar{\nu}_i$, each averaged over a period τ .

$$\sigma_\nu^2(\tau) = \frac{1}{\nu}\frac{1}{2(N-1)}\sum_{n=1}^{N-1}(\bar{\Omega}_{n+1} - \bar{\Omega}_n)^2 \tag{F.17}$$

Note, that Allan deviation $\sigma_y(\tau)$ is the square root of Allan variance.

F.1.5 Link between phase noise and Allan variance

Phase noise manisfest as the jitter in a signals zero crossing. The variance of such (random) zero crossing jitter is related to the variance of the phase noise itself.

The averaging over τ is equivalent to filtering with a rectangular window function $h(t) \in [\tau, 0]$. Thus we can write,

$$\sigma_y^2(\tau) = \left\langle \left[\int_{-\infty}^{\infty} y(u)h(t-u)du \right] \right\rangle \tag{F.18}$$

It can be computed easier in Frequency domain as,

$$\sigma_y^2(\tau) = \int_0^{\infty} S_y(f)||H(f)||^2 df \tag{F.19}$$

where,

$$||H(f)||^2 = \left(\frac{sin\pi\tau f}{\pi\tau f} \right)^2 \tag{F.20}$$

In Fig. F.2 is presented link between phase noise, fractional-frequency noise and Allan variance.

Table F.1: Phase noise

noise type	$S_\phi(f)$	$S_y(f)$	$S_\phi \leftrightarrow \S_y$	$\sigma_y^2(\tau)$
white PM	b_0	$h_2 f^2$	$h_2 = \frac{b_0}{\nu_0^2}$	$\frac{3 f_H h_2}{(2\pi)^2}\tau^{-2}$ $2\pi\tau f_H \gg 1$
flicker PM	$b_{-1}f^{-1}$	$h_1 f$	$h_1 = \frac{b_{-1}}{\nu_0^2}$	$[1.038 + 3\ln(2\pi f_H \tau)]\frac{h_1}{(2\pi)^2}\tau^{-2}$
white FM	$b_{-2}f^{-2}$	h_0	$h_0 = \frac{b_{-2}}{\nu_0^2}$	$\frac{1}{2}h_0\tau^{-1}$
flicker FM	$b_{-3}f^{-3}$	$h_{-1}f^{-1}$	$h_{-1} = \frac{b_{-3}}{\nu_0^2}$	$2\ln(2)h_{-1}$
random walk FM	$b_{-4}f^{-4}$	$h_{-2}f^{-2}$	$h_{-2} = \frac{b_{-4}}{\nu_0^2}$	$\frac{(2\pi)^2}{6}h{-2}\tau$
linear frequency drift $\dot{y}$				$\frac{1}{2}(\dot{y})^2\tau^2$
f_H is the high cutoff frequency, needed for the noise power to be finite				

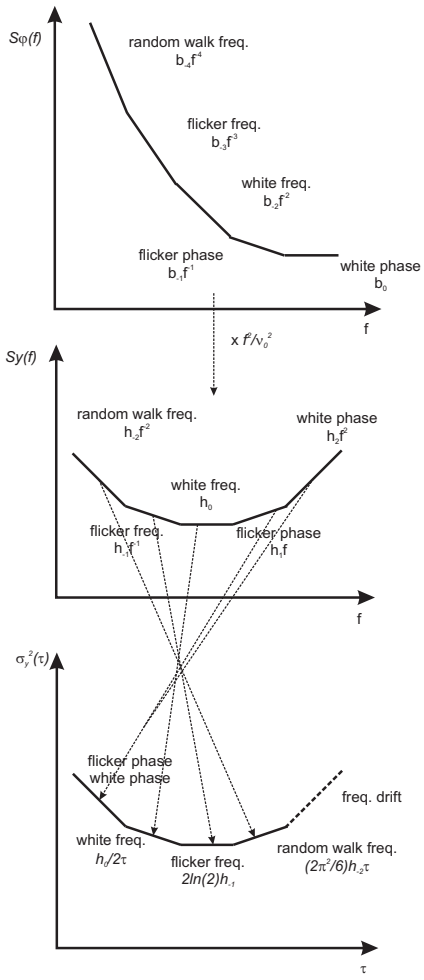

Figure F.2: Phase noise, fractional-frequency noise and Allan variance. Based in figure from Rubiola book [211].

F.2 Passive stability of the laser frequency

In this section we discuss some methods of frequency stabilization. The wavelength λ or the frequency ν of a longitudinal mode in the active resonator is determined by the mirror separation L and the refractive indices n_2 of the active medium with length L and n_1 outside the amplifying region. The resonance condition is

$$qc/\nu = 2n_1(L - L_{actmed}) + 2n_2L, \tag{F.21}$$

where q is number. For simplicity, we shall assume that the active medium fills the whole region between the mirrors. Thus Eq. (F.21) reduces, with $L = L_{actmed}$ and $n_2 = n_1 = n$, to

$$\nu = qc/(2nL) \tag{F.22}$$

Any fluctuation of n or L causes a corresponding change of ν. We obtain from Eq. (F.22)

$$-\frac{\Delta\nu}{\nu} = \frac{\Delta L}{L} + \frac{\Delta n}{n} \tag{F.23}$$

F.2.1 Long-term drift

To illustrate the demands of frequency stabilization, let us assume that we want to keep the frequency $\nu = 375 \times 10^{12}$ Hz of, some solid-state laser constant within 1 kHz. This means a relative stability of $\Delta\nu/\nu \approx 2.6(6) \times 10^{-12}$ and implies that the mirror separation of $L = 0.5$m has to be kept constant within 1.33 pm!

From this example it is clear that the requirements for such stabilization are not trivial. For the next considerations we shall distinguish between long-term drifts of L and n, which are mainly caused by temperature drifts or slow pressure changes, and short-term fluctuations caused, for example, by acoustic vibrations of mirrors, by acoustic pressure waves that modulate the refractive index.

To illustrate the influence of long-term drifts, let us make the following estimate. If α is the thermal expansion coefficient of the material (e.g., quartz or invar rods), which defines the mirror separation d, the relative change $\Delta L/L$ for a possible temperature change ΔT is, under the assumption of linear thermal expansion,

$$\Delta L/L = \alpha\Delta T \tag{F.24}$$

For steel, with $\alpha =\sim 10 \times 10^{-6} K^{-1}$, we obtain from Eq. (F.24) for $\delta T = 0,1$ K a relative distance change of $\Delta L/L =\sim 10^{-6}$, which gives for $\nu = 375 \times 10^{12}$ Hz $\Delta\nu$ a frequency drift of ∼187.5 MHz.

To keep these long-term drifts as small as possible, one has to choose distance holders for the resonator mirrors with a minimum thermal expansion coefficient α. Often massive blocks are used as support for the optical components; these

have a large heat capacity with a time constant of several hours to smoothen temperature fluctuations. However, we shall see that such long-term drifts can be mostly compensated by electronic servo control if the laser frequency is locked to a constant reference frequency standard.

F.2.2 Short-term drift

A more serious problem arises from the short-term fluctuations, since these may have a broad frequency spectrum, depending on their causes, and the frequency response of the electronic stabilization control must be adapted to this spectrum. The main contribution comes from acoustical vibrations of the resonator mirrors. The whole setup of a wavelength-stabilized laser should therefore be vibrationally isolated as much as possible. There are commercial optical tables with pneumatic damping, in their more sophisticated form even electronically controlled, which guarantee a stable setup for frequency-stabilized lasers.

The high-frequency part of the noise spectrum is mainly caused by fast fluctuations of the refractive index in the air region of solid-state lasers.

To develop a quantitative picture of the noise, we will use the frequency noise power spectral density. We can begin by observing that noise causes an individual mode frequency to fluctuate with time, $\delta\nu(T)$. These fluctuations can be characterized by the PSD,

$$S_{\nu n}(f) = \frac{< \delta\tilde{\nu}^2 >}{B} \qquad [\mathrm{Hz}^2/\mathrm{Hz}], \tag{F.25}$$

where the tilde represents a Fourier transform with respect to T and f is the Fourier conjugate variable, B is a unit bandwidth. This frequency noise PSD describes a jitter of the OFC tooth n at a modulation frequency f with a variance of $S_{\nu n}(f)$.

F.3 Active stabilization of the frequency

All the perturbations discussed above cause fluctuations of the optical path length inside the resonator that are typically in the nanometer range. In order to keep the laser frequency stable, these fluctuations can be compensated by corresponding changes of some resonator parameter x. Typically this parameter is a resonator

length L. For such controlled and fast length changes in the nanometer range, piezoceramic elements are mainly used [212, 213]. They consist of a piezoelectric material whose length in an external electric field changes proportionally to the field strength. Typical parameters of such piezoelements are a few nanometers of length change per volt. With stacks of many thin piezodisks, one reaches length changes of 100 nm/V. When a resonator mirror is mounted on such a piezoelement, the resonator length can be controlled within a few microns by the voltage applied to the electrodes of the piezoelement.

The frequency response of this length control is limited by the inertial mass of the moving system consisting of the mirror and the piezoelement, and by the eigenresonances of this system. Using small mirror sizes and carefully selected piezos, one may reach the 100 kHz range [214]. Recently were demonstrated a new design of PZT mount. To using it is possible to have bandwidth up to 180 kHz. The method based on the approach to mitigating the effects of the longitudinal resonances is damping. This is very effectively achieved by drilling out the back of a copper mounting structure and filling it with lead [183].

The frequency stabilization system consists essentially of three elements:

1. The frequency reference standard with which the laser frequency is compared. One may, for example, use the frequency ν_R at the maximum or at the slope of the transmission peak of a Fabry-Perot interferometer that is maintained in a controlled environment (temperature and pressure stabilization). Alternately, the frequency of an atomic or molecular transition may serve as reference. Sometimes another stabilized laser is used as a standard and the laser frequency is locked to this standard frequency.

2. The controlled system, which is in this case the resonator length nL defining the laser frequency δ_L.

3. The electronic control system with the servo loop, which measures the deviation $\delta\nu = \nu_L - \nu_R$ of the laser frequency ν_L from the reference value ν_R and which tries to bring $\delta\nu$ to zero as quickly as possible

The "free-running" linewidth, or short-term stability of the laser, is often not adequate for many applications without active stabilization of the laser frequency. In this section we will describe a powerful and elegant technique, used in some of

the most challenging precision measurements in modern optics, for controlling and stabilizing the frequency of a laser.

F.4 Feedback Loops

A schematic of a simple feedback loop is shown in Fig. F.3 (see for details [215–217]). The first component in the loop is the laser witch frequency is to be stabilized. Part of the output laser radiation is split off and used in the feedback loop. The free-running linewidth and noise spectrum of different lasers, as was shown before in Sect. F.2 can vary greatly depending on the stability and finesse of the resonator design, gain-medium characteristics, and other laser parameters. For example, in many solid-state lasers with relatively high-finesse resonators, the spectral density of frequency noise is often dominated by pump and mechanical fluctuations, which generally fall off as $\sim 1/f$ and can be greatly suppressed by the feedback loop. On the other hand, the dominant frequency/phase noise in many diode laser systems is often of a quantum nature due to larger spontaneous emission rates [218], resulting in significant noise processes extending out to higher Fourier frequencies.

To detect fluctuations in the laser frequency, a highly stable reference is needed for comparison. One common way in which this is achieved is by using a high-finesse Fabry-Perot cavity, constructed in such a way as to provide the necessary stability over the time scale of interest. The mth resonant frequency of a Fabry-Perot cavity, determined by the cavity length L as: $\nu_m = m(c/2L)$, can be extremely sharp when low-loss, high reflecting mirrors are used [219]. Although mechanical cavities may drift on longer time scales, they can provide very high short-term stability ($\sim$ seconds). This stability can be taken advantage of due to a combination of a sharp cavity resonance and a linear response to the incident optical field. Unlike the nonlinear response of atomic transitions that can saturate, the signal from the reference cavity can ideally be increased until the signal-to-noise ratio (SNR) of the detected cavity resonance is sufficient to provide the needed stability for the laser.

To tightly lock the laser frequency to a resonance of the Fabry-Perot cavity, the resonance must be detected quickly and with a high SNR. This is perhaps the most critical part of the feedback loop, as it ultimately determines the performance

of the system. The difference between the laser frequency and cavity resonance is converted into a voltage, with a discriminator coefficient D given in units of [V/Hz]. The discriminator voltage, or error signal, can be obtained by several methods. The simplest and most straightforward approach is to lock to the side of the cavity transmission fringe. The side-fringe locking technique uses the slope on either side of the transmission peak to convert frequency fluctuations of the laser into amplitude fluctuations, which are subsequently detected by a photodiode. Although easy to implement, the technique suffers from several drawbacks. First, amplitude modulation (AM) from the laser directly couples into the error signal; the feedback loop cannot tell the difference between frequency modulation (FM) and AM. Changes in the laser amplitude will therefore be written onto the laser frequency. Secondly, due to the photon-lifetime of the Fabry-Perot cavity [219], fast frequency fluctuations of the laser will not be detected in transmission through the cavity. A final limitation is the narrow locking range. A small deviation from the locking point can cause the laser to unlock if the frequency momentarily shifts across the cavity transmission peak. The last two limitations present a particularly troubling tradeoff; high-finesse cavities are desirable so as to provide a narrow linewidth for laser stabilization, yet will simultaneously limit the bandwidth of the feedback loop and reliability of the lock.

A better method, "Pound-Drever-Hall" (PDH) stabilization, is easy to implement and avoids all the above-mentioned complications [189]. PDH stabilization is closely related to the powerful technique of modulation-spectroscopy used for the sensitive detection of atomic and molecular transitions. Pound first proposed this technique for the stabilization of microwave oscillators by introducing phase modulation at a frequency several times greater than the resonance linewidth [220].To avoid the limitations of AM on the laser beam, PDH stabilization relies on the rapid modulation of a lasers frequency to quickly probe both sides of the cavity resonance. If the resonance information is detected at a sufficiently high modulation frequency, amplitude fluctuations can be reduced to their shot-noise limited level. In addition, PDH stabilization utilizes the light reflected from the Fabry-Perot cavity. This is advantageous since the reflected light will be at a minimum on resonance decoupling AM noise from the error signal. Another important aspect of the PDH technique is that the response will not be limited by the cavity lifetime, allowing for a greater bandwidth in the feedback loop.

Once the error signal (e) is generated, it is sent through the servo "loop filter" to ensure the feedback is applied to the laser with the appropriate phase. Due to the finite time delay in the feedback loop, all Fourier frequencies of the error signal cannot be sent back to the laser with the proper phase. The frequency-dependent voltage gain (G, with units of V/V) must therefore roll off toward zero at some frequency to prevent positive feedback. After the signal is conditioned by the loop filter, the correction voltage is finally applied to the actuator, characterized by a coefficient A in units of Hz/V. The frequency range over which the actuator exhibits a flat frequency response to the applied correction signal usually determines the maximum bandwidth of the servo loop. For instance, a piezo-mounted cavity mirror can be used as an actuator to correct the laser frequency. These often have a resonant frequency on the order of a few kHz. Thus the servo bandwidth needs to remain much less than this in order not to excite the piezo resonance.

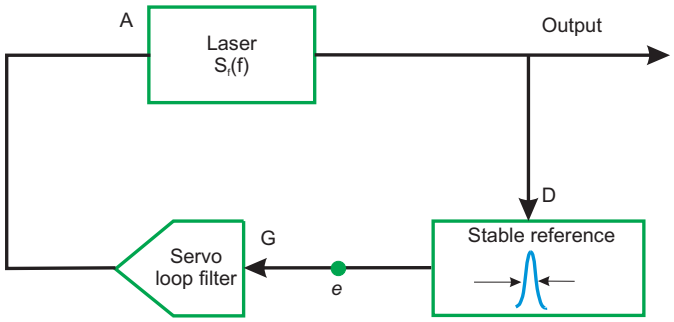

Figure F.3: Simplified schematic of laser feedback loop. S_f is a spectral density of frequency noise; e is an error signal point; D is a discriminator coefficient; G is a loop filter gain; A is an actuator coefficient.

F.5 Feedback Loop: Loop Filter and Actuator

Once a good error signal is obtained, all that remains is to send this signal through the servo loop filter and back to the lasers actuator to "close the loop". As discussed previously, the role of the loop filter is to adjust the error signal such that it is applied to the laser with the appropriate amplitude, phase, and frequency response. To prevent the phase of the error signal from shifting too quickly, result-

ing in positive feedback, it is important to adjust the gain for the overall feedback loop at the unity gain frequency [221].

F.5.1 The PID controller

The other component is the feedback amplifier. It processes the error signal. The gain should be as large as possible and the bandwidth should span as far as possible to control slow and fast frequency excursions. However, there are several limitations set by the requirements for the phase of the feedback gain. A reliable rule for stable operation is that the gain rolls off with high frequencies and the phase shift at the upper unity gain point should be less than π. A more precise definition can be obtained using a Nyquist diagram. As a consequence the delay times have to be kept short and any resonances, mechanical or electronic, have to be avoided. The gain is usually controlled by a PID amplifier, that means a combination of proportional amplifier (middle frequencies), integrator (low frequencies) and differentiator (high frequencies) [222]. All these components contribute to the electronic round-trip phase and have to be carefully optimized.

Unfortunately, most electro-mechanical actuators have resonances in the acoustic range kHz, severely limiting the bandwidth of the amplifier which has to reach unity gain at frequencies well be below the resonance. One option is to split the control into several independent branches. For example, to use a piezo with large range (length changes of several optical wavelengths) at low frequencies to compensate for a drift of the frequencies and to use electro-optic components, such as a phase modulator inside the cavity, which has a smaller range, but no resonance for the control of the high frequency excursions. Extensive research has been carried out into these control systems, for example, for the applications in frequency standards and precision interferometry.

Appendix G

Knife-edge method

G.1 Knife-edge method

Method: Record the total power in the beam as a knife edge is translated through the beam using a calibrated translation stage. The power meter records the integral of the Gaussian beam between $-\infty$ and the position of the knife (see, for example, [223]).

Analysis: Assume a beam propagating in the z-direction with a Gaussian intensity profile:

$$I(x,y) = I_0 e^{-2x^2/w_x^2} e^{-2y^2/w_y^2} \tag{G.1}$$

where w_x and w_y are the $1/e^2$ radii of the beam in the x and y directions respectively. I_0 is the peak intensity.

The total power in the beam is:

$$P_{TOT} = I_0 \int_{-\infty}^{\infty} e^{-2x^2/w_x^2} dx \int_{-\infty}^{\infty} e^{-2y^2/w_y^2} dy = \frac{\pi}{2} I_0 w_x w_y \tag{G.2}$$

Consider the knife edge being translated in the x-direction. The transmitted power is then:

$$
\begin{aligned}
P(X) &= P_{TOT} - I_0 \int_{-\infty}^{X} e^{-2x^2/w_x^2} dx \int_{-\infty}^{\infty} e^{-2y^2/w_y^2} dy \\
&= P_{TOT} - \sqrt{\frac{\pi}{2}} I_0 w_y \int_{-\infty}^{X} e^{-2x^2/w_x^2} dx \\
&= P_{TOT} - \sqrt{\frac{\pi}{2}} I_0 w_y \left[\int_{-\infty}^{0} e^{-2x^2/w_x^2} dx + \int_{0}^{X} e^{-2x^2/w_x^2} dx \right] \\
&= P_{TOT} - \sqrt{\frac{\pi}{2}} I_0 w_y \left[\sqrt{\frac{\pi}{8}} w_x + \int_{0}^{X} e^{-2x^2/w_x^2} dx \right] \\
&= \frac{P_{TOT}}{2} - \sqrt{\frac{\pi}{2}} I_0 w_y \int_{0}^{X} e^{-2x^2/w_x^2} dx
\end{aligned}
\tag{G.3}
$$

Consider now the integral in Eq. (G.3) which we wish to cast in a standard form. Making the substitution $u^2 = 2x^2/w_x^2$, so that $dx = w_x du/\sqrt{2}$ and making the necessary change to the limits of the integral leads to:

$$
P(X) = \frac{P_{TOT}}{2} - \sqrt{\frac{\pi}{2}} I_0 w_y \int_{0}^{\frac{\sqrt{2}X}{w_x}} e^{-u^2} du \tag{G.4}
$$

Using the standard definition of the Error Function listed in the App. G.2 and the expression in Eq. (G.4) for the total power in the beam we arrive at our final result:

$$
P(X) = \frac{P_{TOT}}{2} \left[1 - erf\left(\frac{\sqrt{2}X}{w_x} \right) \right] \tag{G.5}
$$

G.2 The Gaussian Distribution and the Error Function

The Normal or Gaussian distribution function is defined as:

$$
\phi(t) = \frac{1}{\sqrt{2\pi}} e^{-t^2/2} \tag{G.6}
$$

where the pre-factor ensures the correct normalization. Statistical tables give the value of

$$P(t) = \int_{-\infty}^{t} \phi(t)dt \tag{G.7}$$

A perhaps more useful definition includes the width σ and non-zero mean μ of the distribution explicitly:

$$\Phi(t) = \frac{1}{\sigma\sqrt{2\pi}} e^{-(x-\mu)^2/2\sigma^2} \tag{G.8}$$

The full width at half maximum is then related to σ by:

$$FWHM = 2\sqrt{2\ln 2}\sigma \approx 2.35\sigma \tag{G.9}$$

Unfortunately Gaussian beams are defined in yet another way, namely in terms of the $1/e^2$ radius or 'spot size' w:

$$I(r) = \frac{2P}{\pi w^2} e^{-2r^2/w^2} \tag{G.10}$$

where P is the total power in the beam.

The Error Function is defined as follows:

$$erf(x) = \frac{2}{\sqrt{\pi}} \int_0^x e^{-u^2 du} \tag{G.11}$$

and has the properties that:

$$erf(\infty) = 1 \text{ and } erf(-\infty) = -erf(x) \tag{G.12}$$

The Gaussian probability distribution is related to the error function by:

$$P(x) = \frac{1}{2} + \frac{1}{2} erf\left(\frac{x}{\sqrt{2}}\right) \tag{G.13}$$